



FORMATION OF SURFACE DIAMOND-LIKE NANOSTRUCTURES ON GRAPHITE INDUCED BY HIGHLY CHARGED ION IRRADIATION

Thuto Nelson Makgato

A dissertation submitted to the Faculty of Science, University of the Witwatersrand,
Johannesburg, in fulfillment of the requirements for the degree of Masters of Science in
Physics

Johannesburg, 2010

Declaration

I declare that this dissertation is my own work. It is being submitted in fulfillment of the requirements for the degree of Master of Science at the University of the Witwatersrand. It has not been submitted before for any degree or examination at any other university.

Thuto Nelson Makgato

_____ day of _____ 2010

To my family

Let this seed bear the fruit that knowledge brings in the hands of time.

Abstract

The interaction of Antimony Slow Highly Charged Ions (SHCIs) of different charge states with Highly Oriented Pyrolytic Graphite (HOPG) is studied in terms of morphology and electronic modification of single-ion impact induced nanodefects. Results are presented in terms of non-contact Atomic Force Microscopy (NC-AFM) analysis, Raman spectroscopy, Photoluminescence and Scanning Tunneling Spectroscopy (STS). A charge state dependence of radiation damage and nanod defect dimensions is observed using Raman spectroscopy and NC-AFM analysis respectively. Surface treatment of the nanodefects by annealing in a hydrogen atmosphere, induce modification of nanod defect dimensions and the corresponding electronic states as observed from NC-AFM analysis and STS. STS conducted on the treated nanodefects shows significant modification of the electronic energy band gap in Sb^{18+} and Sb^{22+} impact regions. The materials produced in this work by SHCI impact and surface treatment are believed to be diamond-like carbon (DLC) with electronic energy band gaps of approximately 2.05 eV and 2.33 eV corresponding to Sb^{18+} and Sb^{22+} impact regions respectively. DLC nanostructures observed in the present study could provide a host matrix for N-V luminant centers which can be used as single photon sources to fabricate patterned qubits using the Electron Beam Ion Trap (EBIT) for purposes of demonstrating scalable room temperature quantum information devices.

Acknowledgements

I wish to acknowledge and convey my sincere gratitude to the following people for their continued support, guidance, courage and advice without which this dissertation would otherwise not have been possible:

- My supervisor, Prof. Elias Sideras-Haddad
- Dr. Sanjiv Shrivastava
- Our overseas Collaborators: The EBIT Group at LBNL: Dr. Thomas Schenkel, Arunabh Batra, Aruh Persaud
- Rudolf Erasmus
- My family
- My friends
- My Colleagues

I wish to express my gratitude to the Center of Excellence in Strong Materials and the National Research Foundation for financial support.

Table of Contents

Declaration	vi
Acknowledgements	ix
Table of Contents	x
List of Figures	xii
List of Tables	xxiii
1. Introduction	5
1.1 Motivation.....	5
1.2 Dissertation outline	11
2. Theoretical Review	12
2.1 Slow Highly Charged Ions (SHCIs)	12
2.2 Interactions of SHCI with matter	20
2.2.1 Overview.....	20
2.2.2 Coulomb Explosion Model	26
2.2.3 Inelastic Thermal Spike Model (ITS).....	29
3. Diamond: Properties and Synthesis	32
3.1 Carbon Allotropes.....	32
3.1.1 Diamond.....	36
3.1.2 Graphite.....	42
3.2 Diamond Synthesis.....	45
3.2.1 HTHP synthesis of single crystal diamond.	45
3.2.2 CVD diamond synthesis	51
3.2.3 Nanodiamond Synthesis Techniques	54
3.3 The Nitrogen Vacancy Center in diamond.....	65
3.4 Introduction to Quantum Computing	69
4. Experimental Procedures	73
4.1 Electron Beam Ion Trap (EBIT)	73
4.2 SHCI Implantation Details	81
4.3 Monte Carlo Simulations (MC).....	82

4.4	Scanning Probe Microscopies (SPM)	87
4.5	Raman Spectroscopy	101
4.6	Photoluminescence (PL).....	107
4.7	Annealing Apparatus	110
5.	Results and Discussion	112
5.1	Overview.....	112
5.2	AFM Analysis (before annealing).....	112
5.3	AFM Analysis (After annealing).....	121
5.4	Raman Spectroscopy	125
5.5	Photoluminescence (PL).....	138
5.6	Scanning and Tunneling Spectroscopy (STS)	141
6.	Conclusions	149

List of Figures

2.1	Schematic phase space plot of the range of all possible positive ions with nuclear charge Z and electronic charge $ Q < Z$ up to $Z=100$ [30].....	13
2.2	Schematic representation of the relative spatial extent of the wavefunction of a hydrogen-like Nickel ion ($Z=28$) compared with that of a hydrogen atom. The ratio is similar to the size of the planet Neptune compared with size of the Sun [30].....	14
2.3	The total potential energy $W_{\text{pot}}(q)$ of multiply charged Ar^{q+} , Xe^{q+} and Th^{q+} ions versus charge state q [35].....	16
2.4	Diagram showing the ionization sequence for Xenon along an isonuclear sequence. The diagram also shows (smooth line) the ionization potential for Hydrogen along an isoelectronic sequence [30].....	18
2.5	Neutralization energy of xenon and uranium as a function of ion charge. Note, by comparing with figure 2.4, that 40% of the neutralization energy of bare xenon comes from two deepest energy levels. This fraction ranges from 100% to 34% across the periodic table of naturally occurring elements [30].....	19
2.6	Formation of a “hollow atom” as a SHCI approaches the surface of a solid [52].....	23
2.7	Measured sputter yield of LiF for impact Ar^{q+} ions as a function of impact energy [35].....	25

2.8	<p>Snapshot of the time evolution of the Coulomb explosion process for a system consisting of 365 ions. Red and green spheres are used to indicate Si^+ ions and Si atoms respectively. The initial Coulomb repulsive energy stored in the hemispherical region is about 87.3 keV. Between $t = 0$ and 40 fs, the charged region expands significantly. At $t = 80$ fs over 100 ions are ejected from the surface, forming a pronounced hole. By 360 fs the hole is much larger, and about 800 atoms and ions are driven from the surface [60].....</p>	27
2.9	<p>Spatial distributions of pressures (left column) and potential energy (right column) for the system with 365 ions, at several time instants. The times represented in panels (a)-(e) and (a')-(e') are 0, 8, 16, 40 and 80 fs, respectively. All units are in a.u., where 1 a.u. = 2.94×10^{13} Pa or 2.94×10^4 GPa in pressure. The same colour scales are used in (a)-(c) and (a')-(d') to demonstrate the dissipation between 0 and 16 fs. Different colour scales for (d), (e) and (e') are used to focus on the detail of the patterns in the plots [60].....</p>	28
2.10	<p>Mean diameter (top) and height (bottom) of hillock-like nano-structures as a function of the potential energy of Ar^{9+} (open symbol) and Xe^{9+} (full symbol) projectiles. Hillocks are found only above a potential energy threshold of about 14 KeV. The error bars correspond to a standard deviation of the diameter and height distributions; the solid lines are drawn to guide the eye [69].....</p>	31

3.1	Calculated electron density contour of the sp^3 hybrid orbital (left) and the tetrahedral hybridization axes of the four sp^3 orbitals (right). The negative lobes have been omitted for clarity [85].....	34
3.2	Electron cloud representation of the sp^3 hybrid orbital bonding (σ bond) showing covalent bonding [85].....	34
3.3	Planar section of the sp^2 hybrid orbitals of the carbon atom [85].....	35
3.4	The cubic diamond structure, built by a repetition of tetrahedrally bonded blocks. The nearest neighbours define four corners of a cube; cubes are stacked to form a cubic lattice [86, 87].....	37
3.5	The hexagonal diamond (Lonsdaleite) crystal structure, built by repetition of tetrahedrally bonded prisms. Nearest neighbours define triangular prisms which are stacked to form a hexagonal lattice [86].....	37
3.6	Atomic positions in the cubic cell of the diamond structure projected on a cube face; the different colours represent fractions which in turn denote height above the base in units of a cube edge. The points 0 and $\frac{1}{2}$ are on the face of the fcc lattice; those at $\frac{1}{4}$ and $\frac{3}{4}$ are on a similar lattice displaced along the body diagonal by one-fourth of its length. With a fcc space lattice, the basis consists of two identical atoms at $000; \frac{1}{4} \frac{1}{4} \frac{1}{4}$. Note: Blue = 0; Red = $\frac{1}{2}$, Yellow = $\frac{3}{4}$ and Green = $\frac{1}{4}$ [88].....	38
3.7	The two different stacking systems in diamond, i.e. cubic lattice (top) and the hexagonal lattice (bottom) with bilayers in the sequences; .../ABC/ABC/... and .../AB/AB/... respectively [86].....	39
3.8	Three dimensional schematic of the graphite structure [85].....	42

3.9	Schematic of the sp^2 hybridized structure of graphite showing the sigma bonds and the 2p free electrons (above and below the sigma orbitals plane) [85].....	43
3.10	Diagrams showing the arrangement of atoms in two of the most common allotropes of Carbon, namely (a). α -Graphite and (b). β -Graphite [92].....	44
3.11	Pressure-temperature phase diagram of Carbon [94].....	46
3.12	Schematic of diamond growth regions. (a) The diamond growth region using conventional catalysts. (b) The diamond growth region using non-metallic catalysts. Diamond grows in the shaded regions [89].....	49
3.13	NIRIM-type reactor used by Kamo <i>et al.</i> [107].....	52
3.14	SEM images of CVD diamond films deposited at 800°C substrate temperature and 1.5% CH_4 in the reactant gas. A: $\alpha < 1.5$, concentration = 10 ppm B, scale: 13 mm = 3 μm B: $\alpha > 2$, concentration = 60 ppm N, scale: 8 mm = 1 μm [93].....	53
3.15	Schematic illustration of the experimental setup of laser irradiation in liquid [113].....	57
3.16 (a)	Low-resolution TEM bright field image of the cross-section sample with two sites of the spatially periodic structure. (b) Detailed TEM image of one part of the condensed nanocrystals [113].....	58
3.17 (a)	SEM image of the spatially periodic array on amorphous carbon films induced by pulsed-laser irradiation in liquid. (b) Typical SEM image of one treated site. (c) Raman spectrum of the original amorphous carbon	

	films, with the green dotted lines representing the result of a fitted-peak Lorentzian deconvolution. A hatched pane describes the FWHM of the G band. (d) Raman spectrum of the resulting sample, in which the shifts of the G mode and D mode are schematically depicted. The result of a fitted-peak Lorentzian deconvolution and a single skewed BWF line shape is describe by the green dotted lines and a blue symbol line, respectively [113].....	59
3.18	High-resolution lattice image of one of the larger nanocrystals found in the acid residue from the 350 MeV Kr irradiated graphite [119].....	61
3.19	Images (a), (b) and (c) are STM images of the Ar ⁸⁺ impact region. (a) As irradiated (metallic). (b) After electron injection (non-conductive) and (c), after the subsequent hydrogen treatment (non-conductive). Right side curves are <i>I-V</i> characteristics inside and outside of the Ar ⁸⁺ impact region measured by STS [125].....	63
3.20	Diagram showing the nitrogen-vacancy complex in diamond (left) and the corresponding energy level schematics (right) [128].....	65
3.21 (A)	PL data for N-V centers in diamond under 488 nm laser excitation. (B), (C) photon correlation and ESR measurements, respectively, showing the zero field splitting of the ground state of the N-V center [128].....	67
4.1	The drift tubes of EBIT focusing the electron beam [138].....	74
4.2	Diagrams showing the electron beam ion trap at the NIST EBIT, the main region is ~1m in length [139].....	75
4.3	Diagram showing the target chamber at Berkeley EBIT.....	76

4.4	A closer view of the target chamber shown in figure 4.3.....	77
4.5	FIB processed tip. Three holes of different sizes ranging from 1 μm to 100 nm have been drilled on the cantilever. The left insert shows the whole cantilever with the Wheatstone bridge at the bottom. The right insert shows a larger view of the upper 100nm hole [142].....	78
4.6	Cantilever with integrated piezoresistive Wheatstone bridge, bimorph actuator and AFM tip [146].....	80
4.7	Simplified diagram showing the surface patterning system at Berkeley EBIT. Note, the cantilever can be positioned anywhere relative to markers on the sample and revisit any spatial location in a predetermined manner [142].....	80
4.8	Implantation scheme adopted at EBIT (Berkeley) on HOPG (A). One quadrant was left unexposed for reference. The actual HOPG sample is shown in B, the HOPG was kept closed in the holder when not in use to avoid surface accumulation of water vapour from the air.....	81
4.9	Monte Carlo simulations of the ranges of Sb (110 keV) ions in HOPG.....	83
4.10	Monte Carlo Simulations of the lateral distribution of Sb (110 keV) ions in HOPG.....	84
4.11	Monte Carlo simulations of the trajectories of Sb (110 keV) ions in HOPG.....	84
4.12	Transverse view of the Sb (110 keV) ion trajectories using Monte Carlo simulations.....	85

4.13	The Dimension 3100 AFM/MFM apparatus on a vibration isolation table.....	87
4.14	Simplified schematic operation of the Veeco CP II AFM system [151]....	88
4.15	Interatomic force vs. distance curve showing the dependence of the van der Waals force on the sample-tip spacing [152].....	89
4.16	The Veeco CPII AFM Probe cartridge [150].....	91
4.17	Contact and non-contact AFM images of a surface with a water droplet [152].....	93
4.18	The Veeco CP II AFM/STM probe head [150].....	94
4.19	Current-voltage characteristics of an <i>a-C</i> , (top): conventional I-V curve, (middle): differential I-V curve and (bottom): normalized differential current curve [155]. CB and VB refer to the conduction and valence bands respectively.....	100
4.20	Raman scattering of a photon with emission or absorption of a phonon. The process is called Brillouin scattering when an acoustic phonon is involved and polariton scattering when an optical phonon is involved. Similar processes occur with magnons [164].....	102
4.21	Raman spectroscopy/PL setup at the University of the Witwatersrand.....	104
4.22	Diagram showing the light path for the Raman setup shown in figure 4.21.....	105
4.23	Diagram showing the areas on the HOPG sample that were studied using Raman spectroscopy.....	106

4.24	Schematic energy level diagram showing the pathways by which PL transitions occur. Principal radiative (\rightarrow) and nonradiative (\dashrightarrow) transitions causing photoluminescence. S_0, S_1 .. singlet levels; $T_1, T_2, ..$ triplet levels. A represents absorption (10^{-18} - 10^{-15} s). IC: internal conversion ($\sim 10^{-12}$ s). IS: internal crossing ($\sim 10^{-9}$ s) F: fluorescence (10^{-9} - 10^{-8} s). P: phosphorescence (10^{-3} - 10 s) [169].....	109
4.25	Simplified diagram showing the annealing setup at the University of the Witwatersrand. Note: The ceramic tube is connected to a thermocouple to enable temperature control of the system.....	111
5.1	Example of NC-AFM image taken over the Sb^{22+} impact site on HOPG showing line profile directions x and y.....	113
5.2	Line profiles across Sb^{22+} induced nanod defect on HOPG along directions x and y shown in figure 5.1.....	114
5.3	NC-AFM image taken over the Sb^{18+} impact site on HOPG showing line profile directions x and y.....	115
5.4	Line profile taken across a chosen Sb^{18+} induced nanod defect on HOPG along directions shown in figure 5.3.....	116
5.5	Charge state versus defect diameter of induced nanod defects before annealing.....	118
5.6	Charge state versus hillock height of induced nanod defects before annealing.....	119
5.7	NCAFM topography image of a Sb^{18+} impact site on HOPG after annealing.....	121

5.8	3D image of figure 5.7 (top) and line profiles showing the topography of Sb ¹⁸⁺ induced nanodefects (bottom) after annealing. Note the x-y scale is identical to that in figure 5.7.....	122
5.9	Comparison of the (average) defect diameters induced on HOPG before and after annealing as a function of the charge state of the incident Sb ions.....	123
5.10	Comparison of (average) hillock heights induced on HOPG before and after annealing as a function of the charge state of the incident Sb ions....	124
5.11	Raman intensity maps (8 X 8 points) of the unannealed, unirradiated (top) and the unannealed, Sb ²²⁺ irradiated region of the sample (bottom) acquired using 600 lines/mm grating and a 50X objective lens.....	126
5.12	Raman spectroscopy spectra showing unirradiated HOPG (top) and Bi ³⁵⁺ irradiated HOPG (bottom) acquired using the 1800 lines/mm grating and a 50X objective lens.....	127
5.13	Raman intensity map (8 X 8 points) over the unirradiated spot (top) and the Sb ²²⁺ irradiated spot (bottom) after annealing using a 600 lines/mm grating and a 50X objective lens.....	130
5.14	Raman spectra acquired over a random spot in the unirradiated region (top) and in the Sb ²²⁺ irradiated region (bottom) after annealing using the 1800 lines/mm grating and 50X objective lens.....	131
5.15	FWHM of the G peak as a function of the I_D/I_G [16].....	133
5.16	Lorentzian peak fitting of Raman data collected over the Sb ²²⁺ impact site after annealing using the 1800 lines/mm grating and a 50X objective	

	lens. The red line is the fit of the data and the green lines are Lorentzian components of the fit.....	134
5.17	Lorentzian peak fitting results of the Bi ³⁵⁺ irradiated HOPG (unannealed). The red line is the fit of the data and the green lines are Lorentzian components of the fit. The Raman data was acquired using a 1800 lines/mm grating and a 50X objective lens.....	135
5.18	PL spectra of nanodiamonds of different sizes acquired using a 532 nm excitation laser [176]. Note: ZPL refers to the zero phonon line.....	139
5.19	PL intensity spectra taken over the unirradiated site (top) and the Sb ²²⁺ irradiated (bottom) impact site on HOPG using a 50X objective lens, a 600 lines/mm grating and a 514 nm excitation laser.....	140
5.20	STM image showing Sb ²²⁺ induced nanodefects on HOPG and the points along which I-V curves were acquired. The 3D image has the same x-y scale as the 2D image.....	141
5.21	I-V curves acquired over the Sb ¹⁸⁺ (top) and Sb ²²⁺ (bottom) nanodefects on HOPG after annealing showing the inner to the outer regions of the nanodefects.....	142
5.22	Differential current curves for Sb ¹⁸⁺ (top) and Sb ²²⁺ (bottom) induced nanodefects showing the valence (VB) and conduction bands (CB) with respect to the Fermi level, curves from the inner and outer regions on the nanod defect and also the clustered curves labeled A-D.....	144
5.23	Normalized differential curves taken over Sb ¹⁸⁺ (top) and Sb ²²⁺ (bottom) induced nanodefects on HOPG.....	145

5.24	Truncated normalized differential curves taken over Sb ¹⁸⁺ and Sb ²²⁺ nanodefects.....	146
5.25	Plot showing the maximum electronic energy band gap (E_g) Sb ¹⁸⁺ (top) and Sb ²²⁺ (bottom) induced nanodefects (red curve) on HOPG in comparison to graphite (blue curve).....	148

List of Tables

3.1	Some properties of diamond [90, 91].....	41
3.2	Some Properties of Graphite [90, 91].....	44
4.1	Implantation results for all investigated ions using MC simulations.....	86
5.1	Summary of results from observed nanodefects before annealing.....	118
5.2	Summary of results from observed nanodefects after annealing.....	123
5.3	Summary of Raman results obtained from Lorentzian peak fitting before annealing.....	136
5.4	Summary of Raman results obtained from Lorentzian peak fitting after annealing.....	136

Chapter 1

1. Introduction

1.1 Motivation

“The principles of physics, as far as I can see, do not speak against maneuvering things atom by atom”. In his 1959 lecture (published in 1960) titled ‘There is enough room at the bottom’, Nobel laureate Richard Feynman envisioned the possibility of constructing devices using a bottom-up approach as a possible solution to limitations of miniaturization and technology in general. Up to the present day, the concept of nanotechnology is attributed to Richard Feynman [1].

Nevertheless, it is not clear when humans began to take advantage of nanosized materials. However, it is known that in the fourth century A.D. Roman glassmakers were fabricating glasses containing nanosized metals. An artifact from this period called the Lycurgus cup resides in the British Museum in London. The colour of the cup changes from green to a deep red when a light source is placed inside it [2].

Advances in instrumentation coupled with a renewed understanding of science, has brought about a new era in experimental physics; the age of nanotechnology. In general, the primary focus of nanotechnology and nanoscience is on the synthesis, characterization, analysis and application of nanostructured materials. Nanostructures are materials that have at least one of its dimensions confined in the nanometer ($\sim 1-100$ nm) range e.g. quantum dots, nanocrystals, nanowires and nanotubes.

Uniqueness of the structural characteristics, energetics, response, dynamics and physics of nanostructures, constitutes the basis of nanoscience [3]. Appropriate control of the properties and response of nanostructures can lead to new devices and technologies such as biomolecular machines, quantum information systems, and spintronics.

Several methods for synthesizing nanostructures have been proposed and tested, with each method having its strengths and weak points. Some of these methods include; chemical vapour deposition (CVD) methods, laser pyrolysis, sol-gel techniques, colloidal chemistry, ion beam techniques and other exotic methods.

One novel way to produce nanostructures on solid surfaces involves kinetic sputtering with fast ions. However, the interaction of energetic ions (atoms) with surfaces leads to a variety of emission phenomena (emission of electrons, photons, atoms, ions, clusters etc.) and results in pronounced modification of the surface and near-surface regions (change in composition and structure, defect production, removal of atoms etc.) [4].

In kinetic sputtering, the decelerated primary projectiles usually transfer (kinetic) energy and momentum to the target atoms, displacing them from their original position and

eventually causing their emission into vacuum [5]. Therefore fast ions unavoidably cause radiation damage.

As opposed to this, potential sputtering (PS), i.e. desorption induced by potential energy of *slow* highly charged ions (SHCIs), holds great promise as a much more selective nanostructuring tool [6,7]. PS may cause large sputter yields even at such low impact energy where kinetic sputtering and defect creation in deeper layers is not possible [8]. It is only recently that the unique qualities of SHCIs are being appreciated which make these ions an exceptional tool for nanostructuring solid surfaces.

SHCIs are generally characterized by their large potential energy and low kinetic energy. Nanosized defects created by SHCIs ranging between 3 nm to 50 nm have been observed in the form of craters or blisters in several materials such as silicon [9], mica [10], highly oriented pyrolytic graphite (HOPG) [11], SiO₂ and Al₂O₃ [12] using scanning probe microscopy techniques (SPM) particularly the atomic force microscope (AFM) and the scanning and tunneling microscopy (STM).

Morphological/topological alterations induced by SHCIs have been extensively studied by several authors but remains a subject of ongoing research. However, Hamza *et al.* observed photoluminescence from nanostructures in silicon at 20K following intense ultrafast electronic excitation with Xe⁴⁴⁺ ions [13]. This was one of the first observations of electronic modification of SHCI induced nanodefects.

The transformation of electronic states in nanoscale defects following SHCI irradiation is an intriguing subject, particularly the transformation of graphite into diamond. It has been reported that nanodiamond structures have been formed under extremely fast

electron or ion beam irradiation [14]. Nanodiamonds were formed in certain sections of an ion track in a wide range of experimental conditions. Such transformation is due to the strong electronic excitation of carbon atoms along ion tracks. However, this kind of phenomenon is not observed in the low kinetic energy regime [15].

Nevertheless, in recent experiments, modification of electronic states at Ar⁸⁺ impact sites induced on HOPG was achieved by Meguro *et al.* where post-irradiation surface treatment was applied [15, 16]. The surface treatment involved electron injection from an STM tip and He-Cd laser irradiation. This provided sufficient activation for the hybridization of sp² (graphite bonds) into sp³ (diamond bonds).

Carbon related materials such as highly oriented pyrolytic graphite (HOPG), diamond, fullerenes and carbon nanotubes are expected to be key materials in nanoelectronics and other nanoscale technologies. Carbon-based materials exhibit special properties and are generally earth-friendly in nature. These materials are also environmentally compatible since they represent substances with properties between organic and inorganic compounds [16].

When structures are spatially confined within dimensions that are close (\sim 1- 100 nm) to the average atomic diameter such as in nanostructures, quantum effects become more dominant as a result of a phenomenon known as quantum confinement. The possibility of using solid state ion implantation techniques to create qubit arrays of appropriate quantum information nanostructures that are necessary to demonstrate a scalable quantum computer has brought about a renewed interest in the search for the ideal quantum computer. The quantum computer is described in more detail in section 3.4.

One major challenge in the solid state approach to quantum computer development schemes has been finding appropriate single photon sources that have long enough coherence times to execute quantum algorithms. In the solid state approach, coherent control of single quantum systems has been achieved in a number of systems e.g. superconducting Cooper pair boxes [17] and electron spins in quantum dots [18]. Among these, the nitrogen-vacancy (N-V) center in diamond [19] is unique. This is because its spin exhibits a long coherence time that persists up to room temperature [20], whereas most other systems only allow coherent control at cryogenic temperatures.

Coherent manipulation of N-V centers on large ensembles was first achieved many years ago [21, 22]. Recently however, coherent rotations and spin echoes of a single N-V center spin were reported by Jelezko *et al.* [23]. This landmark experiment, demonstrates that the N-V center provides a testbed for quantum manipulation in the solid state at room temperature [24, 25].

On the other hand, single center spectroscopy allows the study of the local environment of the N-V center [26] and has already unveiled anisotropic spin interactions and magnetic dipolar coupling to spins of other defects in diamond [27]. Recent results of these studies include observation of strong coupling between a single N-V center and the spin of a single substitutional nitrogen atom [28, 29] and the measurement of the spin relaxation time of a single nitrogen electron spin [29]. By combining single center spectroscopy with coherent control, the coherent interaction of the N-V center spin with its environment can be probed, which might ultimately lead to coherent quantum circuits [24].

The underlying notion in this work is to utilize the unique properties of slow highly charged ions to synthesize diamond nanostructures as a host matrix for N-V luminant centers which could ultimately be coherently manipulated to achieve practical quantum computation. The behaviour of an N-V center localized in a nanodiamond matrix is an interesting study that can allow one to study properties of decoherence under quantum confinement.

Amongst the already mentioned successes in N-V center studies, this work is also motivated by several successful studies on the charge state dependence of nanodiamond formation and also on the lack of utilization of hydrogen as a catalyst in ion-based nanodiamond synthesis. The variation of the SHCI charge state could probe different aspects of defect formation and nanodiamond synthesis and is hence an interesting experimental technique to explore.

1.2 Dissertation outline

This work is categorized into six chapters. The first chapter aims to motivate and give a historical context of the scientific knowledge relevant to the present research. The second chapter covers the necessary theoretical background that is utilized in studies of carbon based nanotechnologies using highly charged ions. Details of the experimental apparatus utilized in this work are outlined in chapter three. In chapter four, the results of investigations conducted are presented and analyzed. Chapter five and six are geared towards discussion and conclusion of findings from the present study respectively.

Chapter 2

2. Theoretical Review

2.1 Slow Highly Charged Ions (SHCIs)

A SHCI is defined to be any atom that has a large number of electrons ($Q \gg 1$) removed from its naturally occurring atomic structure such that, the total energy released upon neutralization, $E_0 \gg 10$ eV [30]. In this context, slow is defined as velocities $v < v_{\text{Bohr}}$ where the Bohr velocity, v_{Bohr} is a factor of $\sim 1/137$ (the fine structure constant) less than the speed of light. The Bohr velocity, $v_{\text{Bohr}} \approx 2.19 \times 10^6$ ms⁻¹ [31], and represents the orbital velocity of the outer most electrons in neutral atoms. Beyond this benchmark, physical processes such as electron capture by a highly charged ion may be significantly different.

When a number of electrons ($Q=1, 2, 3, \dots$) are sequentially removed from a given atomic specie, a series of ions with varying N electron structures ($N=Z-Q$) having the same nucleus are produced. Such sequences are known as isonuclear sequences, and they represent a phase space that cuts through the (Z, Q) space of all possible SHCIs (figure 2.1) [30].

Positively charged ions created in laboratories are created along isonuclear nuclear sequences. However, SHCIs can also be conceptualized to be created along isoelectronic sequences. These are sequences in which the N electron structure is not varied, but rather the nuclear charge Z is varied in an incremental manner.

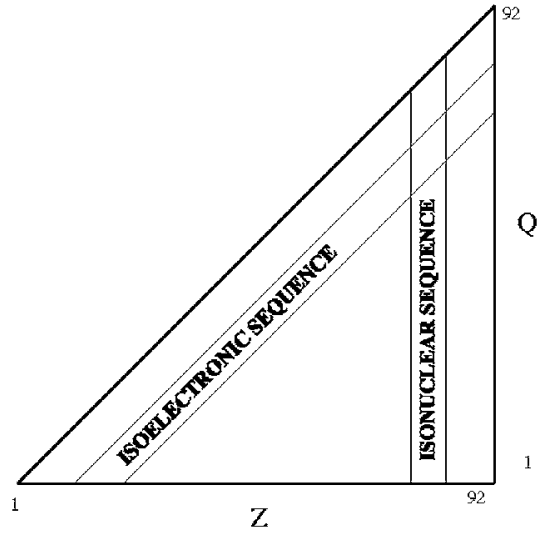


Figure 2.1 Schematic phase space plot of the range of all possible positive ions with nuclear charge Z and electronic charge $|Q| < Z$ up to $Z=100$ [30].

Note: Isoelectronic sequences begin at $Z=N+1$ whereas isonuclear sequences begin at $Q=1$.

The creation of a SHCI results in a compression of the electronic wavefunction of the subject atom, hence the size of a SHCI is in some cases dramatically different from that of its neutral counterpart. A simple scaling law for one-electron ions predicts that the size of the wavefunction varies as the reciprocal of the ion charge as follows;

$$R \sim (1/Z) \sim 1/(Q + 1) \sim 1/Q \quad \text{for } Q \gg 1. \quad (2.1)$$

where the R =Bohr radius [30].

Using equation 2.1, figure 2.2 is drawn to a scale below.

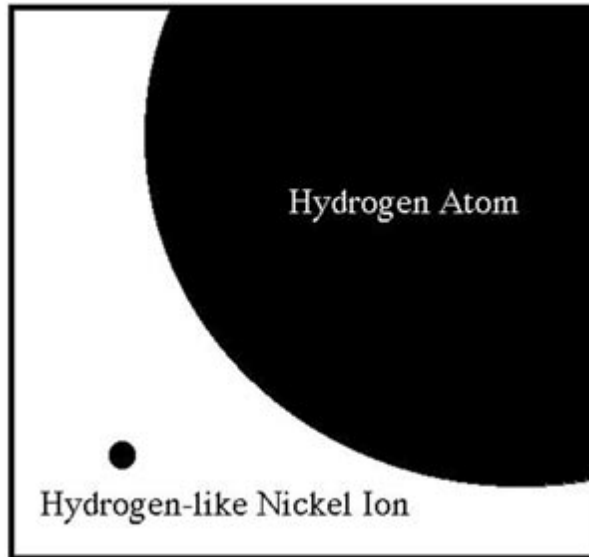


Figure 2.2 Schematic representation of the relative spatial extent of the wavefunction of a hydrogen-like Nickel ion ($Z=28$) compared with that of a hydrogen atom. The ratio is similar to the size of the planet Neptune compared with size of the Sun [30].

The above scaling law for atomic size predicts that the electronic density for a hydrogen-like uranium ion is $\sim 780\,000$ times higher than that of a hydrogen atom. For very highly charged ions (e.g. $Q=92$ with $E_0 \sim 750\,000$ eV) the spatial extent of the wavefunction enters a new regime. In the atomic limit (e.g. for the Hydrogen isoelectronic sequence), the electron orbits the nucleus at a characteristic distance that is large compared to both

the spatial extent of the nucleus and the fundamental length scale at which the electron ceases to behave as point particle with a finite charge (i.e. the Compton wavelength) [30].

As mentioned earlier in this work, SHCIs are considered to have neutralization energies beyond the realm of ordinary experience, such that $E_0 \gg 10$ eV. Therefore, SHCIs are commonly associated with two kinds of energies namely kinetic (which is a factor of Q larger than it would have been if it was singly charged) and potential energy. This is contrary to singly charged ions whose energies are mainly kinetic.

The kinetic energy of SHCIs accelerated through a given electric field is commonly represented by the quantity keV/u, where u is the rest mass of the ion in atomic mass units. However, sometimes the scaling is assumed and the energy is represented merely as keV. The ion velocity is given by the expression:

$$\begin{aligned} \frac{keV}{u} \times 1.07 \times 10^{-6} &= \frac{T(v)}{m_0 c^2} = \frac{\sqrt{p^2 c^2 + m_0^2 c^4} - m_0 c^2}{m_0 c^2} & (2.2) \\ &= \sqrt{\frac{1}{1 - v^2/c^2}} - 1 = \frac{1}{2} \frac{v^2}{c^2} + \frac{3}{8} \frac{v^4}{c^4} + \frac{5}{16} \frac{v^6}{c^6} + \dots \end{aligned}$$

where $T(v)$ is the relativistic expression for the kinetic energy of the ions [30]. There exists a minimum impact velocity v_m that a SHCI can have before impact with the surface. This minimum velocity is a result of acceleration caused by the unscreened surface charge and is commonly referred to as image charge acceleration. The energy gain due to image charge acceleration exceeds 1eV by approximately a factor of $Q^{3/2}$ for

a typical surface [32]. Nevertheless, impact velocities below v_m (down to zero) have been reported on imperfectly conducting surfaces [33, 34].

Highly charged ions are characterized by their large potential energy (relative to conventional singly charged ions). The potential energy corresponds to their production where q electrons (q : ion charge state) have to be removed from an originally neutral atom. This potential energy becomes rather large for higher values of q as shown in figure 2.3 below [35].

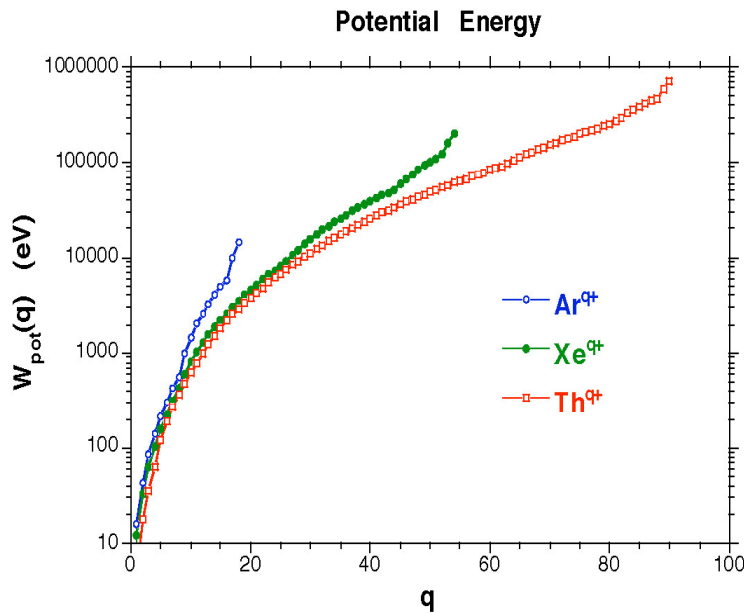


Figure 2.3 The total potential energy $W_{pot}(q)$ of multiply charged Ar^{q+} , Xe^{q+} and Th^{q+} ions versus charge state q [35].

The large potential energy typical for SHCIs also creates relatively high, sometimes very high neutralization energy (e.g. for $Q \gg 1$). Ionization energies of elements across the periodic table vary. Similarly the ionization energies of SHCIs created along an

isonuclear sequence vary. This is primarily because the outermost electrons become more tightly bound to the nucleus as electrons are sequentially removed from the naturally occurring atom.

As electrons are sequentially removed from the SHCI, the ionization potential varies rapidly with respect to the ion charge. This is a direct result of the increasing nuclear charge relative to the inner most electrons in the electronic cloud and the decreasing distance between the inner most electrons and the nucleus. Simple Coulomb scaling potential for one electron atoms predicts the following [30]:

$$U(Z) \sim Z/R \sim Z/(1/Z) = Z^2 \quad (2.3)$$

All species of ions will approach Q^2 enhancement in the high charge limit ($Q \rightarrow Z$) as seen in figure 2.4. The neutralization energy E_0 is given by the sum of all the ionization energies of the charge states at and below that of the ion. Thus the energy E_0 is enhanced by the fact that the individual ionization energies in the sum are themselves enhanced by the ' Q^2 enhancement' described above [30]. Examples of neutralization energy as a function of charge is presented in figure 2.5.

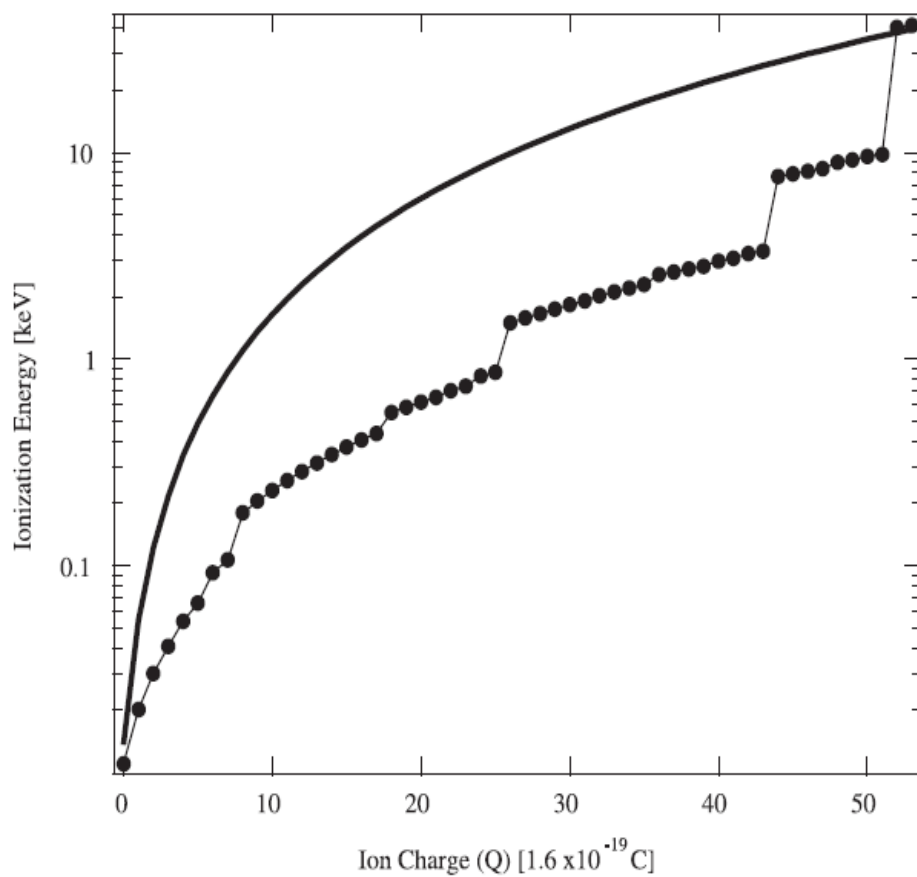


Figure 2.4 Diagram showing the ionization sequence for Xenon along an isonuclear sequence. The diagram also shows (smooth line) the ionization potential for Hydrogen along an isoelectronic sequence [30].

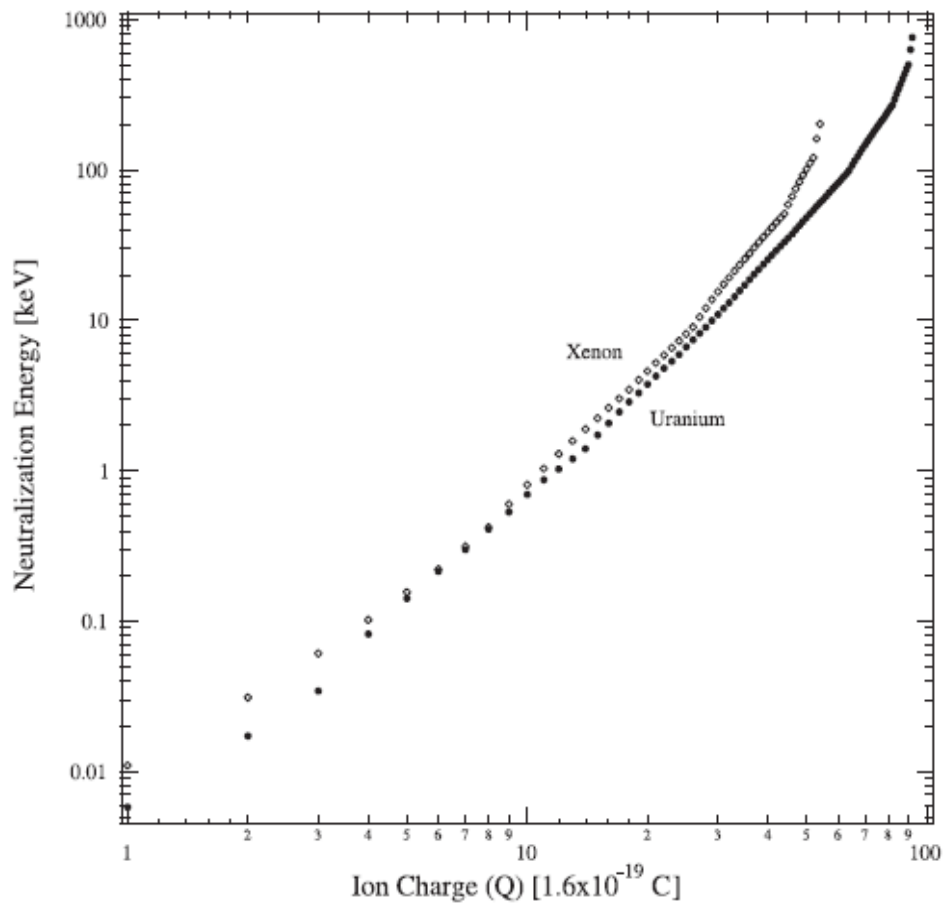


Figure 2.5 Neutralization energy of xenon and uranium as a function of ion charge. Note, by comparing with figure 2.4, that 40% of the neutralization energy of bare xenon comes from two deepest energy levels. This fraction ranges from 100% to 34% across the periodic table of naturally occurring elements [30].

2.2 Interactions of SHCI with matter

2.2.1 Overview

The stopping of ions in matter has been a subject of interest at least since the early 1900s. Great contributors to the theoretical treatment of the stopping of singly charged ions in matter include Bohr [36, 37], Bethe [38, 39], Bloch [40, 41], Firsov [42, 43] and Lindhard [44, 45]. Later improvements to the theory were made by several authors including Sigmund [46] and Ziegler [47]. However, contrary to the stopping of singly charged ions in matter, the interaction of highly charged ions with matter is a relatively recent experimental study and is a subject of ongoing research.

When SHCIs impinge on solid surfaces, modification of the surface and near surface regions occurs on a nanometer scale as a result of two main physical phenomena, namely physical and potential sputtering. The former, occurs by means of direct collisions with atoms of the target material both on the surface and near surface regions. Depending on the kinetic energy of the projected SHCIs, modification of the surface occurs by means of bond breaking between surface and near surface atoms, production of structural defects and the ejection of atoms into vacuum, e.g. conventional ion implanters [5].

Ions projected onto a given target material will first interact with the electronic cloud of the target atoms before interacting with the nuclei of the target atoms. This interaction can be categorized into nuclear stopping and electronic stopping [47]. For singly charged ions (\sim keV), the interaction with matter is mainly nuclear and to a much lesser extent,

electronic [47], however, for swift heavy ions which have a relatively higher velocity ($\sim \text{MeV}/\text{amu}$) the interaction is dominated by electronic stopping [48, 49].

Potential sputtering occurs as a result of the removal of electrons from a given neutral atomic specie. SHCIs by definition have relatively low velocities and hence their kinetic energy is low. As q increases for SHCIs, the resulting potential energy increases in a non-linear manner. The interaction of SHCIs with solid surfaces is thus largely characterized by potential sputtering. The response of a solid surface to deposition of potential energy is a function of many parameters including the both kinetic and potential energy of the projectile ions.

In more detail, as the SHCI approaches the surface, a collective response of the surface electrons is induced. This response is created by the dielectric response of the surface due to the presence of a charged particle, thereby creating an “image charge”. The effect of the image charge on the SHCI is in most cases, a net acceleration towards the surface. As a result of this “image charge acceleration, a lower limit to the projectile velocity is set. Burgdörfer and Meyer [50] predicted an energy gain due to the image charge prior to surface impact given by:

$$\Delta E_{q,im} \approx 1.2q^{3/2}(eV). \quad (2.4)$$

Neutralization of the SHCI occurs before the impact with the surface. This process has been described by the classical-over-the-barrier model (COB). According to the COB model, electrons experience a potential barrier between the surface and the projectile. This barrier is formed by the projectile’s screened Coulomb potential, the projectile’s image potential and the image potential of the electron. As the projectile approaches the

surface, the height of the barrier will decrease and drop below the Fermi level at a critical distance given by

$$R_c(q) = \frac{1}{2W_\phi} \sqrt{8q + 2} \approx \frac{\sqrt{2q}}{W_\phi} \quad (2.5)$$

where W_ϕ is the work function of the material concerned [50]. At this critical distance from the surface, electrons from the surface will be transformed into unoccupied states (quasi-stationary Rydberg states) of the approaching ion which overlap with filled surface valence band states. This continuing resonance capture results in a situation where the outermost orbitals of the SHCI are filled preferentially thereby forming a so called “Hollow atom” [51].

After a critical distance is reached, a number of processes start to compete. The hollow atom will start to shrink as an electron from the projectile is transferred into an empty surface state with a binding energy less than the surface workfunction. The change in charge of the hollow atom due to this rapid auto-ionization will proceed as a result of the continued resonance capture of electrons.

Auger processes can also occur above the surface. One of these processes, Auger neutralization, occurs where an electron from the surface valence band is captured by the ion and another is ejected as an Auger electron. Auger de-excitation of the projectile, on the other hand, is where the excited projectile electron is demoted to a lower shell. This can also occur if another surface electron is captured by the projectile and the initially excited electron is ejected [52].

The resulting above-surface neutralization picture is one of a constantly shrinking electron cloud around the original SHCI as shown below in figure 2.6. Neutralization of a singly charged ion is found to take place at distances of a few angstroms above the surface. For SHCIs on the other hand, neutralization is found to be charge dependent and can start at comparably larger distances.

Once the approaching projectile is in contact with the surface, the outer electrons of the not-yet-relaxed SHCI will be peeled off by surface electron screening. A second, more compact, hollow atom will be formed below the surface. The electrons of the solid will form a compact screening cloud around the SHCI in a timescale related to the plasmon frequency of the solid [52].

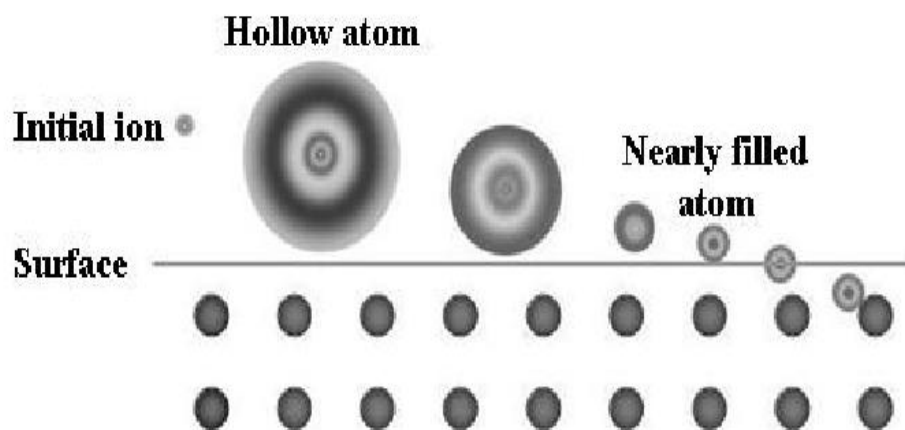


Figure 2.6 Formation of a "hollow atom" as a SHCI approaches the surface of a solid [52].

Below the surface, the hollow atom can de-excite via three processes [53]:

- **Auger neutralization / auto-ionization**

Inner shell vacancies can be filled when excited projectiles eject electrons into vacuum and remaining excited electrons are demoted to lower states.

- **“Side feeding”**

Close collisions with target atoms can fill vacancies via quasi-resonant neutralization (“side feeding”). This may occur if there is sufficient overlap of inner electronic orbitals of the target and core states of the projectile.

- **X-ray emission**

Inner-shell vacancies can decay via X-ray emission and this is the latest step in hollow atom neutralization as it is strongly dependent on the projectile core charge.

Auger processes that take place above and below the surface together will peel off processes that account for the emission of electrons during the interaction. The emitted secondary electrons and X-rays only account for a small fraction of the initial potential energy carried by the SHCI, 1% and 5% respectively. Neutralization of the SHCI takes in a few femtoseconds. The surface atomic motion requires time scales of picoseconds. Thus the major portion of the initial potential energy of the SHCI is initially deposited into the electronic system of the surface [52].

Electronic excitation resulting from SHCI impacts on materials corresponds to the creation of electron-hole pairs (“hot holes”) in the conduction and or valence band of the target, and of inner-shell holes of target atoms. For most metal surfaces, such sudden

perturbation of the electronic structure can be rapidly accommodated. The excitation energy will therefore dissipate within the target material without inducing structural surface modification. This is the main reason that no charge state dependence of sputtering has been observed for Au, Si and GaAs [54, 55].

In materials with reduced electron mobility (e.g. insulator targets), a sudden modification of the near-surface electronic structure cannot be restored immediately and may therefore induce structural modifications (defect formation, desorption, sputtering etc.), giving rise to sputtering induced by the projectile's potential, i.e. potential sputtering. This potential sputtering process is characterized by a strong dependence of the observed sputtering yields on the charge state of the impinging ion, and can take place at ion impact energies well below the kinetic sputtering threshold (figure 2.7) [35].

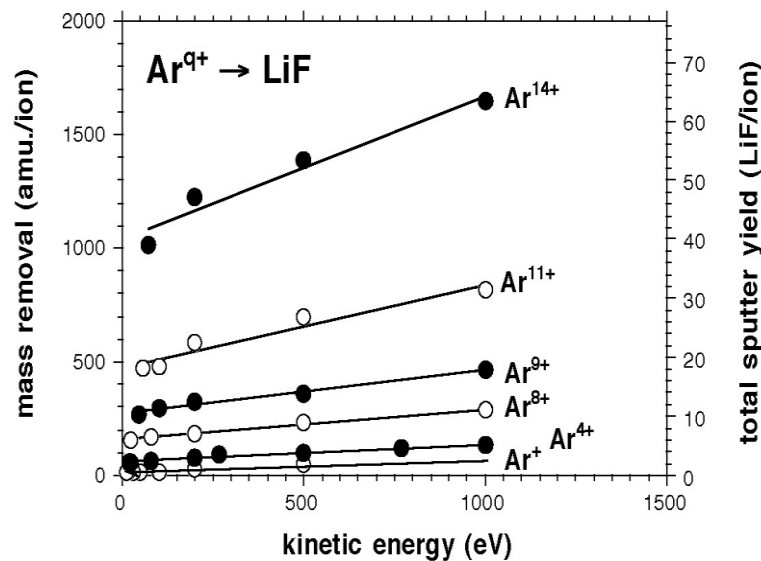


Figure 2.7 Measured sputter yield of LiF for impact Ar^{q+} ions as a function of impact energy [35].

2.2.2 Coulomb Explosion Model

The Coulomb explosion process has been proposed to be the cause of surface damage following SHCI impact [56, 57]. In fact, it is only recently that clear evidence for the existence of surface Coulomb explosions induced by SHCIs has been obtained [58, 59]. Cheng and Gillaspay performed the first full-scale three-dimensional molecular dynamics simulations of the Coulomb explosion model [60]. Although the Coulomb explosion model has been studied by several authors, it remains a subject of ongoing research.

In the Coulomb explosion model, target (surface and near surface) atoms receive kinetic energy in the surface equivalent of an ion explosion spike [61, 62, 63]. A surface domain with high ionization density is formed in the course of electron emission during relation of SHCIs. Several hundred, mostly low energy (<20 eV) electrons are emitted from metals and insulators by SHCI like Xe^{44+} and Au^{69+} [64, 65].

In insulators and poor conductors, charge neutrality cannot be reestablished on the time scale of several picoseconds, i.e. before ionized target atoms are repelled from each other resulting in a Coulomb explosion [31]. The rapid expansion of the target material is thought to send a shock wave into the material. The intersection of the shock wave in the surface can lead to desorption of neutral and charged molecules and clusters [65, 66, 67].

Nevertheless, the main argument against the Coulomb explosion mechanisms question whether hole lifetimes even in insulators are sufficiently long to prevent re-neutralization of the charged domain before the lattice can respond [68]. Figures 2.8 and 2.9 show

some results of the Coulomb explosion computer simulations that were conducted by Cheng and Gillaspay where, a Si (111) surface consisting of 34 560 atoms distributed over 24 layers was subjected to SHCI impact. Details of the simulation are given in ref [60].

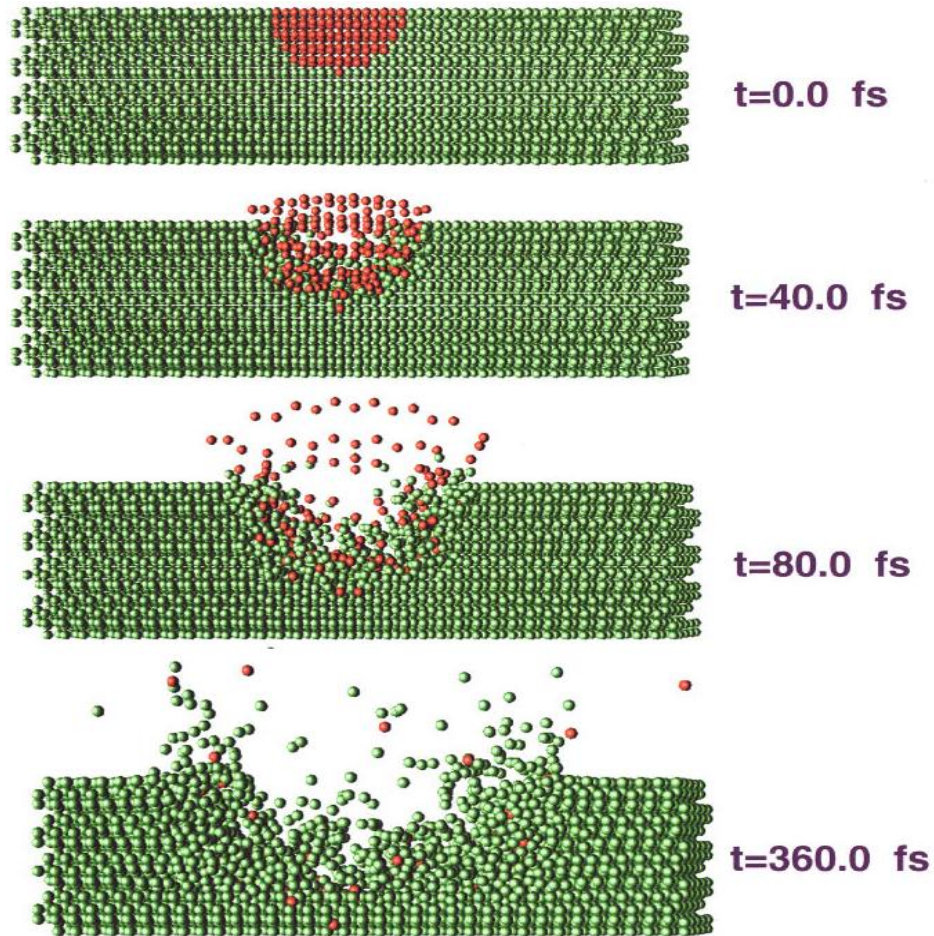


Figure 2.8 Snapshot of the time evolution of the Coulomb explosion process for a system consisting of 365 ions. Red and green spheres are used to indicate Si⁺ ions and Si atoms respectively. The initial Coulomb repulsive energy stored in the hemispherical region is about 87.3 keV. Between $t = 0$ and 40 fs, the charged region expands significantly. At $t = 80$ fs over 100 ions are ejected from the surface, forming a pronounced hole. By 360 fs the hole is much larger, and about 800 atoms and ions are driven from the surface [60].

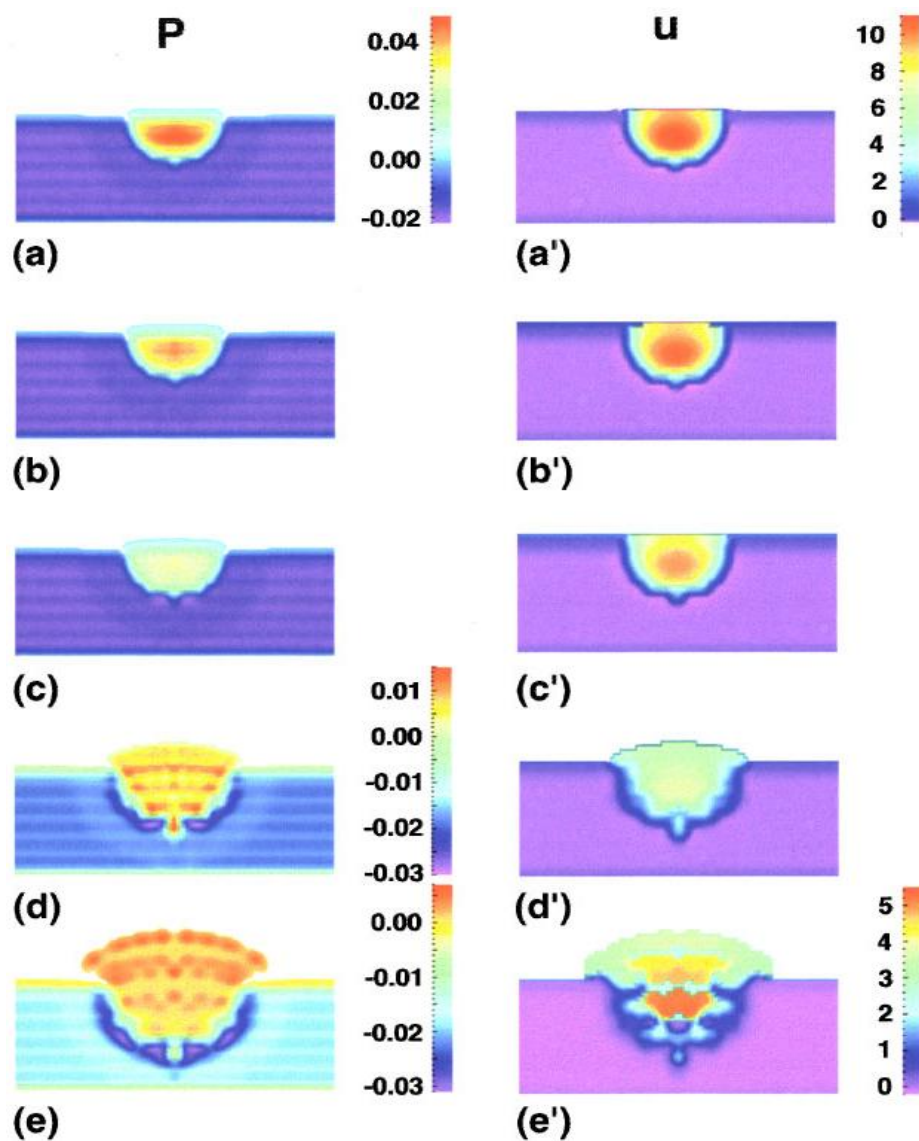


Figure 2.9 Spatial distributions of pressures (left column) and potential energy (right column) for the system with 365 ions, at several time instants. The times represented in panels (a)-(e) and (a')-(e') are 0, 8, 16, 40 and 80 fs, respectively. All units are in a.u., where 1 a.u. = 2.94×10^{13} Pa or 2.94×10^4 GPa in pressure. The same colour scales are used in (a)-(c) and (a')-(d') to demonstrate the dissipation between 0 and 16 fs. Different colour scales for (d), (e) and (e') are used to focus on the detail of the patterns in the plots [60].

2.2.3 Inelastic Thermal Spike Model (iTTS)

The iTTS is a mathematical model initially designed to explain in a quantitative manner, the behaviour of materials when subjected to fast ion impact. Since the 1950s, several theoretical models have been proposed to explain the appearance of latent tracks induced in matter by the slowing down process of incident ions in the electronic stopping power regime [69]. Among these, the ionic spike model for insulators of Fleischer *et al.* [70] and the thermal spike model [71] initially proposed by Seitz and Koehler [72] are the most often used.

In the thermal spike model, the energy lost by the slowing down of a heavy ion is shared between electrons by the electron-electron interaction and is then transferred to the lattice atoms by electron-phonon coupling. The formation of a high temperature cylinder along the incident ion path is assumed, the temperature of which could be higher than the melting and vaporization temperatures of the material [69].

Due to the small volume of the cylinder, the cooling rate may reach $\sim 10^{14} \text{ Ks}^{-1}$ so the molten matter cools down within $\sim 10^{-11} \text{ s}$ and changes back to solid state. In the framework of this model, the latent track is assumed to result from the rapid quenching of the entire cylinder of the molten matter. Chronologically, the ionic spike (10^{-15} - 10^{-13} s) comes into play before the thermal spike (10^{-12} s) [69].

Above a critical value of the energy loss, dE/dx , damage produced in the core of the track leads to a macroscopic volume increase (swelling [73, 74]), track etchability [75] and stress [76]. At the surface of ionic crystals, swift ions induce nanometric hillocks [77, 78]

above a threshold value similar to that for swelling [74]. Although numerous experimental data are available for hillock formation due to swift heavy ion impact, the principle of the mechanism is still not yet fully understood [79].

El-Said *et al.* studied SHCI induced surface defects on CaF₂ single crystals. In their investigation, they found that nanostructures induced by SHCI show close resemblance with those created by fast ions. They observed a strong dependence of the formation on potential energy rather than on stopping power, also that there exists a well-defined threshold of potential energy required for the onset of nano-hillock formation (see figure 2.10) [79].

Mathematical Description

The inelastic thermal spike model is described mathematically by two coupled equations [80, 81, 82] governing the energy diffusion of the electron and lattice subsystem respectively. A time-dependent thermal transient process is expressed in cylindrical geometry:

$$C_e \frac{\partial T_e}{\partial t} = \nabla(K_e \nabla T_e) - g(T_e - T) + B(r, t) \quad (2.6)$$

$$\rho C(T) \frac{\partial T}{\partial t} = \nabla(K(T) \nabla T) + g(T_e - T), \quad (2.7)$$

where T_e , T , C_e , $C(T)$ and K_e , $K(T)$ are the temperature, the specific heat and the thermal conductivity for the electronic and the atomic systems respectively, ρ is the mass

density of states of the lattice, and g the electron-phonon coupling constant. $B(r, t)$ is the energy density per unit time supplied by the incident ions to the electronic system at radius r and time t [69]. Further details regarding the model are discussed the references; [69, 81, 82, 84].

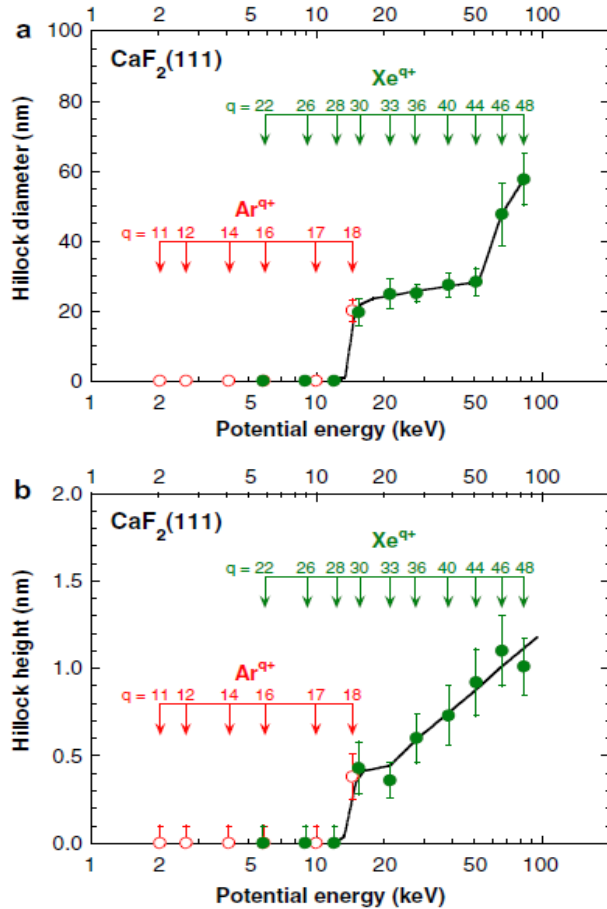


Figure 2.10 Mean diameter (top) and height (bottom) of hillock-like nano-structures as a function of the potential energy of Ar^{9+} (open symbol) and Xe^{9+} (full symbol) projectiles. Hillocks are found only above a potential energy threshold of about 14 KeV. The error bars correspond to a standard deviation of the diameter and height distributions; the solid lines are drawn to guide the eye [69].

Chapter 3

3. Diamond: Properties and Synthesis

3.1 Carbon Allotropes

Allotropes refer to different chemical compounds formed by any atomic species. The different chemical structures are due to different bonding possibilities that exist between atomic species with the surrounding atoms. Carbon is the sixth element on the periodic table, has the electronic configuration: $[\text{He}]2s^22p^2$ and an atomic radius of ~ 0.077 nm [85].

Carbon can form a variety of allotropes including diamond, graphite and carbon nanotubes (multiwalled and single walled). Although carbon exhibits a complex allotropy, allotropes that are frequently found in nature are diamond and graphite, which in turn exhibit different physical properties as a result of the difference in their chemical structures.

Carbon atomic orbitals can hybridize to form so called hybrid orbitals (sp^2 , sp^3 and sp hybrid orbitals). In the sp^3 hybrid orbital, the arrangement of the electrons of the L shell of the carbon atom in the ground state is modified as one of the 2s electrons is promoted to the higher 2p orbital.

These new orbitals are labeled sp^3 since they are formed from one s and three p orbitals. In this hybrid sp^3 state, the carbon atom has four $2sp^3$ orbitals. This then raises the valence state from two to four. A calculated sp^3 electron-density contour is shown in figure 3.1. It is important to note that hybrid orbitals are only formed in the bonding process with other carbon atoms and are not representative of an actual structure of a free carbon atom [85].

The four hybrid sp^3 orbitals (known as tetragonal hybrids) have identical shape but different spatial orientation. Connecting the endpoints of these vectors forms a regular tetrahedron with equal angles to each other of 109.28° (see figure 3.1).

The sp^3 hybrid orbitals form a strong bond when the carbon atom combines with a sp^3 orbital from another carbon atom since the concentration of the bonding electrons between the nuclei minimizes the nuclear repulsion and maximizes the attractive forces between themselves and both nuclei. This type of bond is directional and is called a sigma bond (σ) shown in figure 3.2 [85].

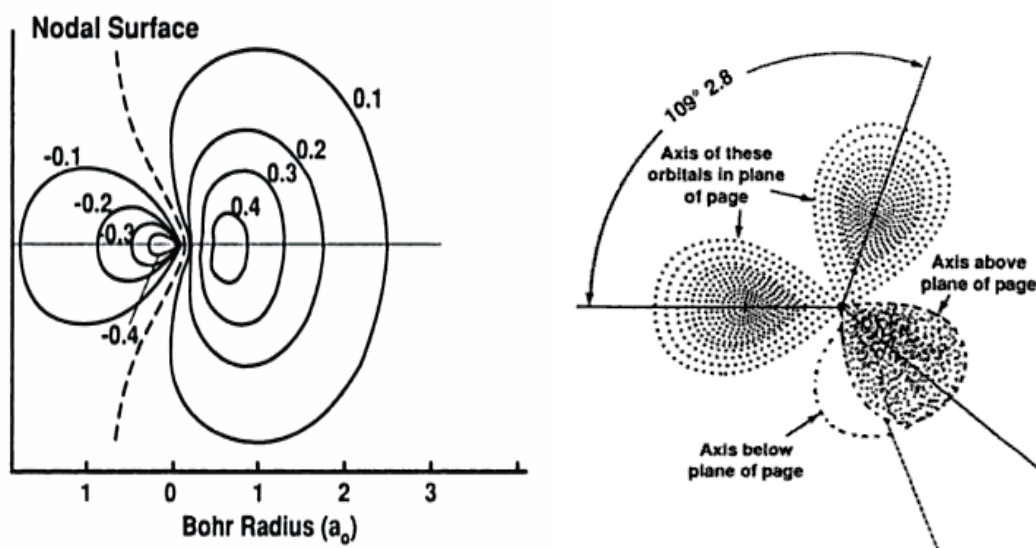


Figure 3.1 Calculated electron density contour of the sp^3 hybrid orbital (left) and the tetrahedral hybridization axes of the four sp^3 orbitals (right). The negative lobes have been omitted for clarity [85].

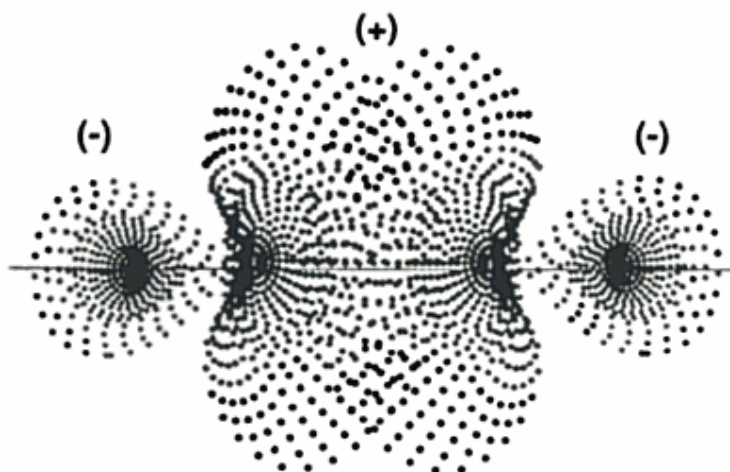


Figure 3.2 Electron cloud representation of the sp^3 hybrid orbital bonding (σ bond) showing covalent bonding [85].

Whereas the sp^3 orbital is the key to diamond and aliphatic compounds, the sp^2 (or trigonal) orbital is the basis of all graphitic structures and aromatic compounds. In a sp^2 orbital, the arrangement of the electrons of the L shell of the carbon atom in the ground state is modified as one of the 2s electrons is promoted and combined with two of the 2p orbitals (hence sp^2). The result such a modification is three sp^2 and an unhybridized free (or delocalized) p orbital. Therefore, the final valence of the system is four.

The calculated electron-density contour of the sp^2 orbital is similar in shape to that of the sp^3 orbital shown in figure 3.1. However, the three identical sp^2 orbitals are in the same plane and their orientation of maximum probability forms a 120° angle from each other (figure 3.3). The fourth orbital (the delocalized non-hybridized p electron), is directed perpendicular to the plane of the three sp^2 orbitals and becomes available to form the subsidiary pi (π) bond with other atoms [85].

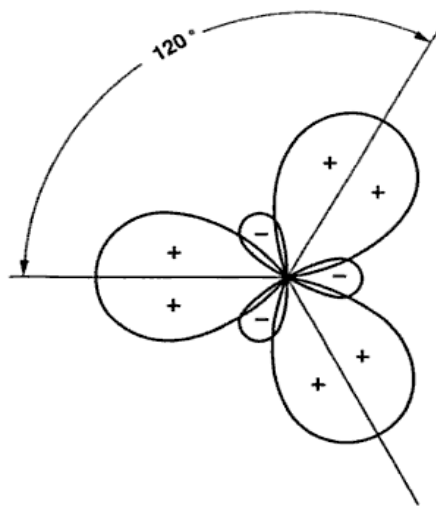


Figure 3.3 Planar section of the sp^2 hybrid orbitals of the carbon atom [85].

The sp^2 like the sp^3 bond, is covalent in nature. It is also a very strong bond, however, the overlap in the sp^2 orbital with other sp^2 orbitals is more pronounced, has a shorter bond length and a higher energy. The sp^2 orbital is directional like the sp^3 orbital. It is also called a sigma (σ) orbital and the bond is called a sigma (σ) bond [85].

3.1.1 Diamond

Diamond is a carbon allotrope in which each carbon is covalently bonded to four other carbon atoms at a distance of $\sim 1.545 \text{ \AA}$ forming a tetrahedral geometry [85]. Nearly all diamonds adopt this structure except a small percentage which show a hexagonal structure related to wurtzite and these are called Lonsdaleite (see figures 3.4 and 3.5).

Diamond bonds result from a hybridization of one s and three p orbitals thereby forming so called sp^3 hybridized orbitals at bonding angles of 109.47° in three dimensions. As a result of this bonding nature, the structure of diamond is denser than that of graphite and has an atomic density of $\sim 1.77 \times 10^{23} \text{ atoms/cm}^3$ i.e. ($\sim 3.57 \text{ g/cm}^3$) [86].

The nearest neighbours in the diamond tetrahedral bond can be imagined as placed at four of the eight corners of a cube as shown in figure 3.4 where the bond directions are $\langle 111 \rangle$. The tetrahedral element may also be visualized with the four nearest neighbours defining a three-dimensional prism with triangular cross-section. These prisms may be stacked to form a hexagonal lattice as shown in figure 3.5.

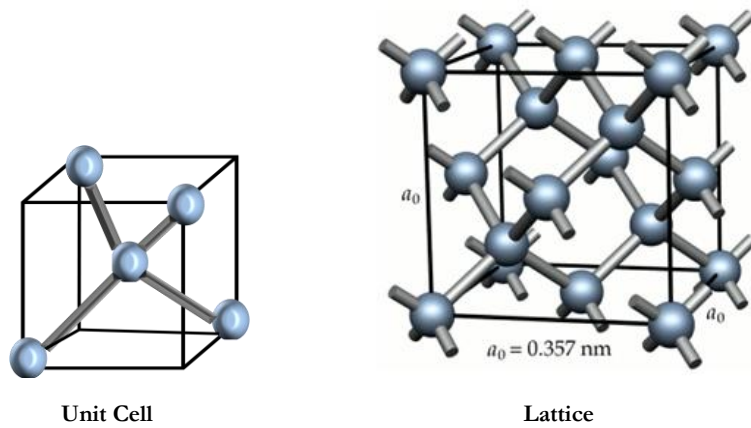


Figure 3.4 The cubic diamond structure, built by a repetition of tetrahedrally bonded blocks. The nearest neighbours define four corners of a cube; cubes are stacked to form a cubic lattice [86, 87].

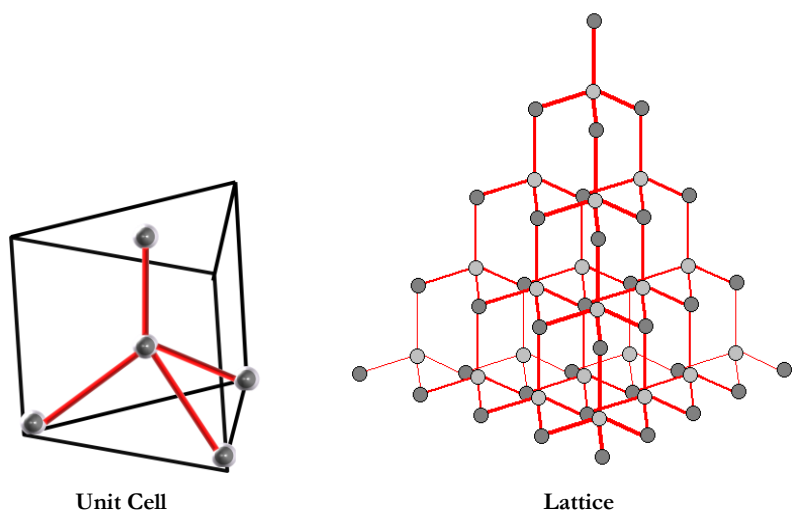


Figure 3.5 The hexagonal diamond (Lonsdaleite) crystal structure, built by repetition of tetrahedrally bonded prisms. Nearest neighbours define triangular prisms which are stacked to form a hexagonal lattice [86].

The space lattice of diamond is fcc (face centered cubic). The primitive basis has two identical atoms at $000; \frac{1}{4} \frac{1}{4} \frac{1}{4}$ associated with each point of the fcc lattice (see figure 3.6). The maximum proportion of the available volume which may be filled by hard spheres is only 0.34, which 46% of the filling factor for a closest packed structure such as fcc or hcp (hexagonal close packing). Carbon, Silicon, Germanium and Tin can all crystallize in the diamond structure, with lattice constants $a = 3.56, 5.43, 5.65$ and 6.46 \AA respectively [88].

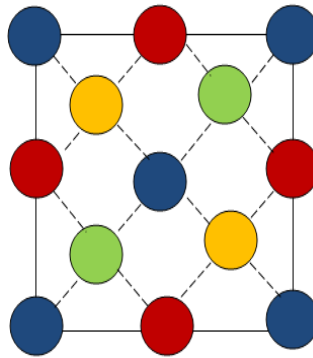


Figure 3.6 Atomic positions in the cubic cell of the diamond structure projected on a cube face; the different colours represent fractions which in turn denote height above the base in units of a cube edge. The points 0 and $\frac{1}{2}$ are on the face of the fcc lattice; those at $\frac{1}{4}$ and $\frac{3}{4}$ are on a similar lattice displaced along the body diagonal by one-fourth of its length. With a fcc space lattice, the basis consists of two identical atoms at $000; \frac{1}{4} \frac{1}{4} \frac{1}{4}$. Note: Blue = 0; Red = $\frac{1}{2}$, Yellow = $\frac{3}{4}$ and Green = $\frac{1}{4}$ [88].

The two different stackings of the basic tetrahedral element are shown in figure 3.7. The diamond-cubic lattice can also be seen to be constructed of a three-dimensional array of

six-membered rings where each ring has the “chair” conformation. The rings make up bilayer sheets of atoms that are parallel to the $\langle 111 \rangle$ planes. These sheets are stacked in the $\dots/ABC/ABC/\dots$ sequence [86].

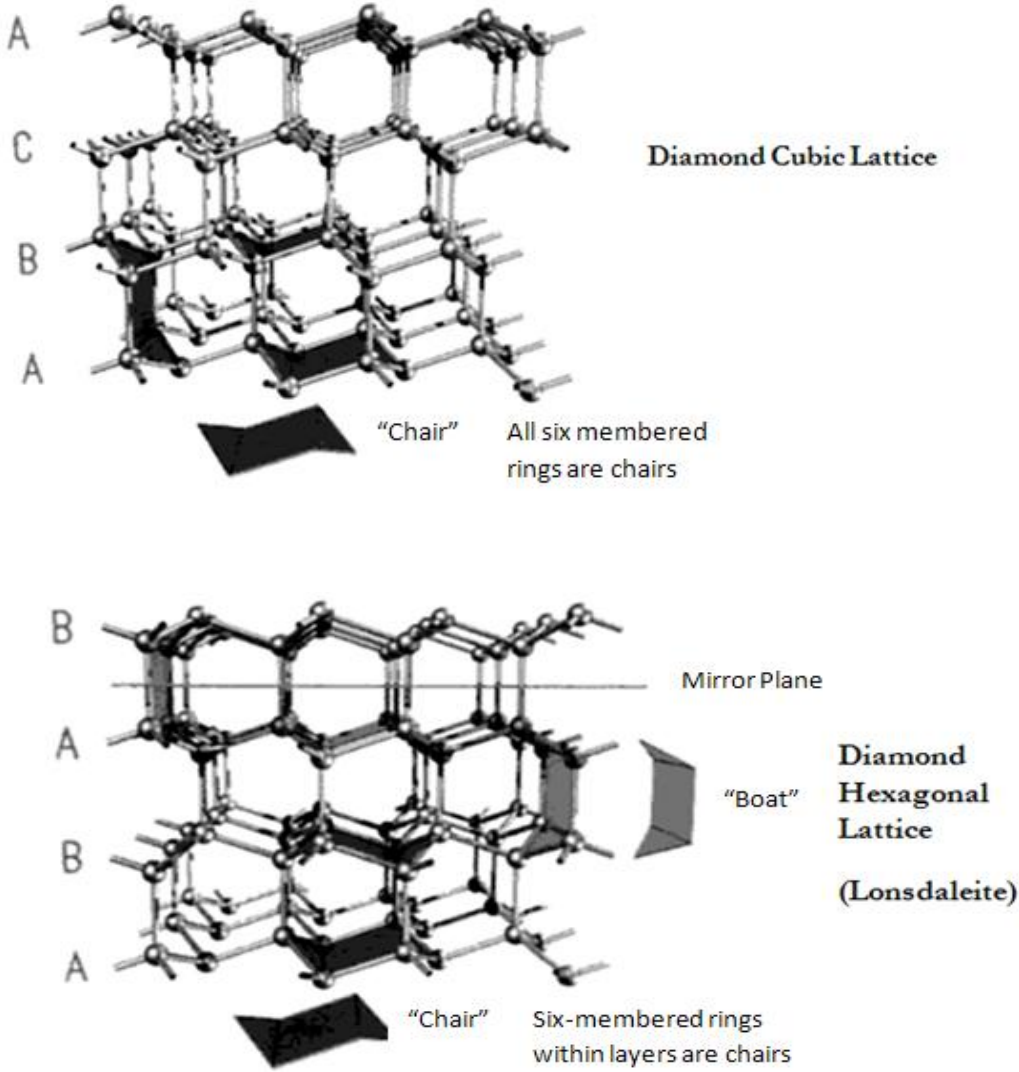


Figure 3.7 The two different stacking systems in diamond, i.e. cubic lattice (top) and the hexagonal lattice (bottom) with bilayers in the sequences; $\dots/ABC/ABC/\dots$ and $\dots/AB/AB/\dots$ respectively [86].

The numerous applications of diamond are a direct result of its extreme properties. Diamond is the hardest known naturally occurring mineral according to Mohr's hardness scale. As a result, it is commonly used in industrial applications as an abrasive. The tetrahedral sp^3 covalent bonds allow diamond to have a very stable structure (metastable) even at room temperature. Diamond is also used in the manufacturing of Infra-Red (IR) Detectors as it is the best known thermal conductor.

Diamond Types

Diamond is classified into several categories depending largely on its purity or impurity levels. Advances in optical absorption techniques suggest that nitrogen is the most common impurity in naturally occurring diamond. Natural diamonds that have a large fraction of nitrogen are classified as type I, whereas those that are largely free of nitrogen impurities are classified as type II. Type I diamonds can be further classified into Ia if the nitrogen exists in an aggregated form or as Ib if the nitrogen exists as single substitutional atoms.

Most natural diamond belongs to the subdivision type Ia and the nitrogen concentration can be as high as 3000 ppm. Less than 0.1% of naturally occurring diamonds are type Ib with typical concentrations of 40 ppm. In both the Ia and Ib type diamonds, nitrogen acts as an electron donor with ionization energies of 4.0 and 1.7 eV respectively, implying that the crystals are electrically insulating at room temperature.

Some, very rare in nature, type II diamonds are highly conductive, exhibiting resistivities as low as 25 Ωm ; these are classified as type IIb. On the other hand, nitrogen-free high resistivity diamond is classified as type IIa. Type IIb diamonds are p-type semiconductors with typical boron concentrations less than 1 ppm and acceptor ionization energy of 0.37 MeV [89]. Table 3.1 below shows some properties of diamond.

Table 3.1 Some properties of diamond [90, 91].

PROPERTY	UNITS	VALUE
Lattice constant (300 K)	[\AA]	3.5668
Elastic Modulus	[GPa]	700-1200
Young's Modulus (111 direction)	[GPa]	1223
Bulk Modulus	[GPa]	442.3
Density	[g/cm ³]	3.515
Melting Point	[K]	3750-3850
Heat Capacity	[Jg ⁻¹ °C ⁻¹]	0.4715
Thermal conductivity:		
• (Type I, 300 K)	[Wm ⁻¹ K ⁻¹]	895
• (Type IIa, 300 K)	[Wm ⁻¹ K ⁻¹]	2300
• (Type IIb, 300 K)	[Wm ⁻¹ K ⁻¹]	1350
Thermal expansion coefficient		
• (300 K)	[x 10 ⁻⁶ /°C]	0.8
• (193 K)	[x 10 ⁻⁶ /°C]	0.4
• (400-1200 K)	[x 10 ⁻⁶ /°C]	1.5
Electronic band-gap (0 K)	[eV]	5.48
Electronic band-gap (300 K)	[eV]	5.50
Electron mobility (300 K) (high-purity single-crystal CVD)	[cm ² V ⁻¹ s ⁻¹]	1800-4500
Hole Mobility (300 K) (high purity single-crystal CVD)	[cm ² V ⁻¹ s ⁻¹]	1200-3800

3.1.2 Graphite

Graphite is the most common allotrope of carbon. It is also the most thermodynamically stable form of carbon particularly α -graphite. Along any plane in the graphite lattice, each sp^2 hybridized carbon atom combines with three other sp^2 hybridized atoms to form covalent σ bonds which in turn make up a series of hexagonal rings, all located in parallel as shown in figure 3.8. The fourth valency (the free delocalized electron) is oriented perpendicular to this plane (figure 3.9).

Unlike the sigma (σ) orbital, it is non-symmetrical and is called by convention a pi (π) orbital. It is available to form a subsidiary pi (π) bond [85]. The planar sheets in graphite are weakly held together by van der Waals forces with an average separation of 3.34 Å between the planes. This separation is large in comparison to the single carbon-carbon bond length of 1.54 Å. In the graphite lattice, the planes follow the pattern: ABABAB in the case of α -graphite and ABCABCABC for β -graphite (figure 3.10).

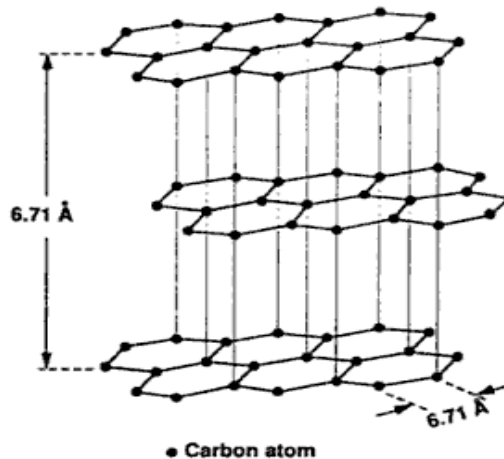


Figure 3.8 Three dimensional schematic of the graphite structure [85].

Since the graphite sheets are weakly bound by van der Waals forces, the sheets can easily slide over neighboring planes. For this reason, graphite is commonly used as a lubricant in industry. The π -electron system is delocalized and hence enables the material to conduct charge parallel to the planes. Therefore graphite behaves as an electrical conductor along the lattice planes.

However, along the direction perpendicular to the planes, no chemical bonding exists. As a result graphite does not conduct electricity along the direction perpendicular to the planes. Table 3.2 shows some properties of graphite which are a direct result of its chemical structure.

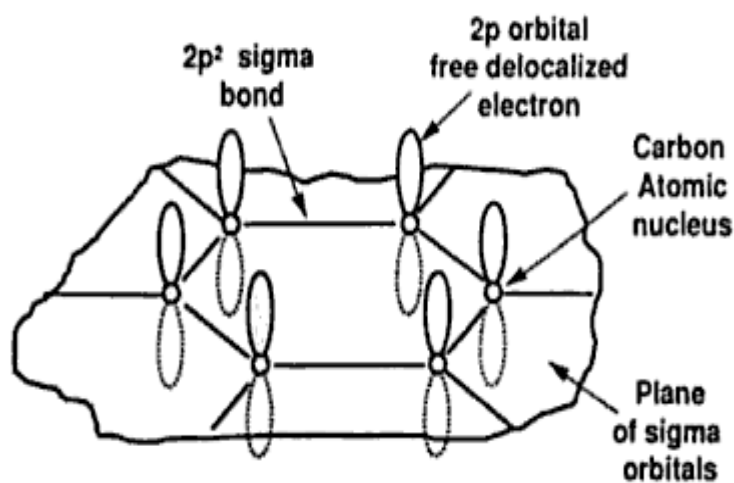
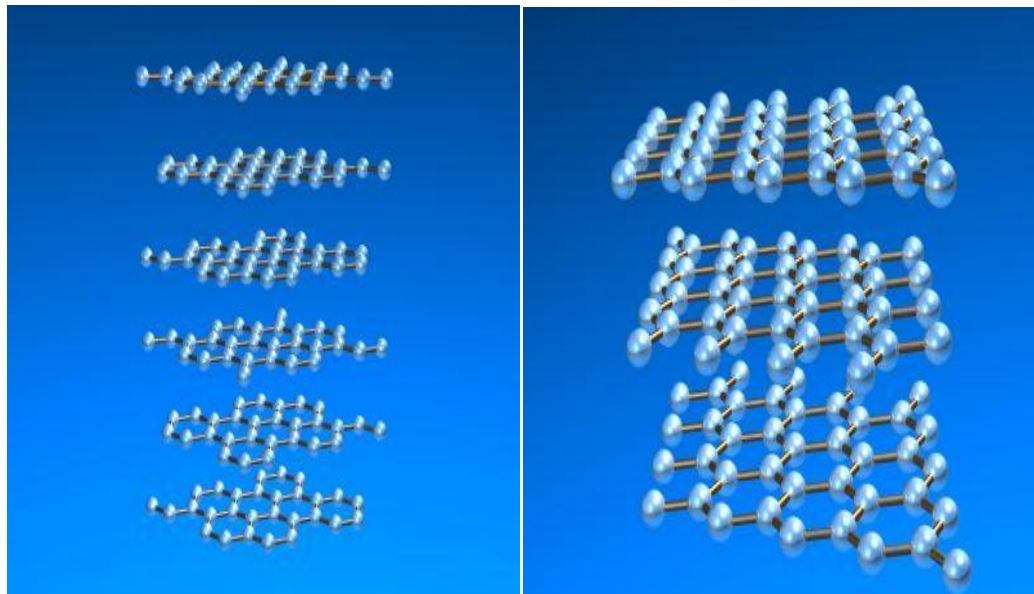


Figure 3.9 Schematic of the sp^2 hybridized structure of graphite showing the sigma bonds and the $2p$ free electrons (above and below the sigma orbitals plane) [85].



(a)

(b).

Figure 3.10 Diagrams showing the arrangement of atoms in two of the most common allotropes of Carbon, namely (a). α -Graphite and (b). β -Graphite [92].

Table 3.2 Some Properties of Graphite [90, 91].

PROPERTY	UNITS	VALUE
Lattice constant	[\AA]	2.462
Bond Length	[\AA]	1.421
Density	[g/cm^3]	2.26
Melting Point	[K]	4200
Band Gap	[eV]	-0.04
Thermal Conductivity	[W/cmK]	300.06
Heat Capacity, C_p	[J/moleK]	8.527
Thermal Expansion Coefficient		
• (in plane)	[$\times 10^{-6}/^{\circ}\text{C}$]	8.8
• (along c axis)	[$\times 10^{-6}/^{\circ}\text{C}$]	27.3

3.2 Diamond Synthesis

Probably the first recorded synthesis of diamond was performed by Scot J B Hannay in 1880. He used a mixture of hydrocarbonates, lithium and oil which was heated up in iron pipes until it blasted [93]. In this section, the synthesis of diamond is discussed. Several methods of producing diamond have been explored to date. However, this section will only focus on the following methods for the synthesis of diamond: high temperature high pressure synthesis techniques (HTHP), chemical vapour deposition (CVD) and nanodiamond synthesis techniques.

3.2.1 HTHP synthesis of single crystal diamond.

High temperature high pressure diamond is synthesized at the conditions where diamond is thermodynamically more stable than graphite. Although this implies that knowledge of the carbon phase diagram is important for diamond synthesis, this is not sufficient for the synthesis in practice. Kinetic considerations are also necessary [89].

The activation energy of direct conversion (solid-solid transformation) from graphite to diamond is very large and very high temperatures are required. Catalysts are employed to decrease the required activation energy for diamond to graphite conversion. Synthetic diamond has three forms namely: single crystal (commonly used in electronic applications), polycrystalline aggregate and powder [93]. Figure 3.11 shows the phase diagram of diamond with several phase boundaries.

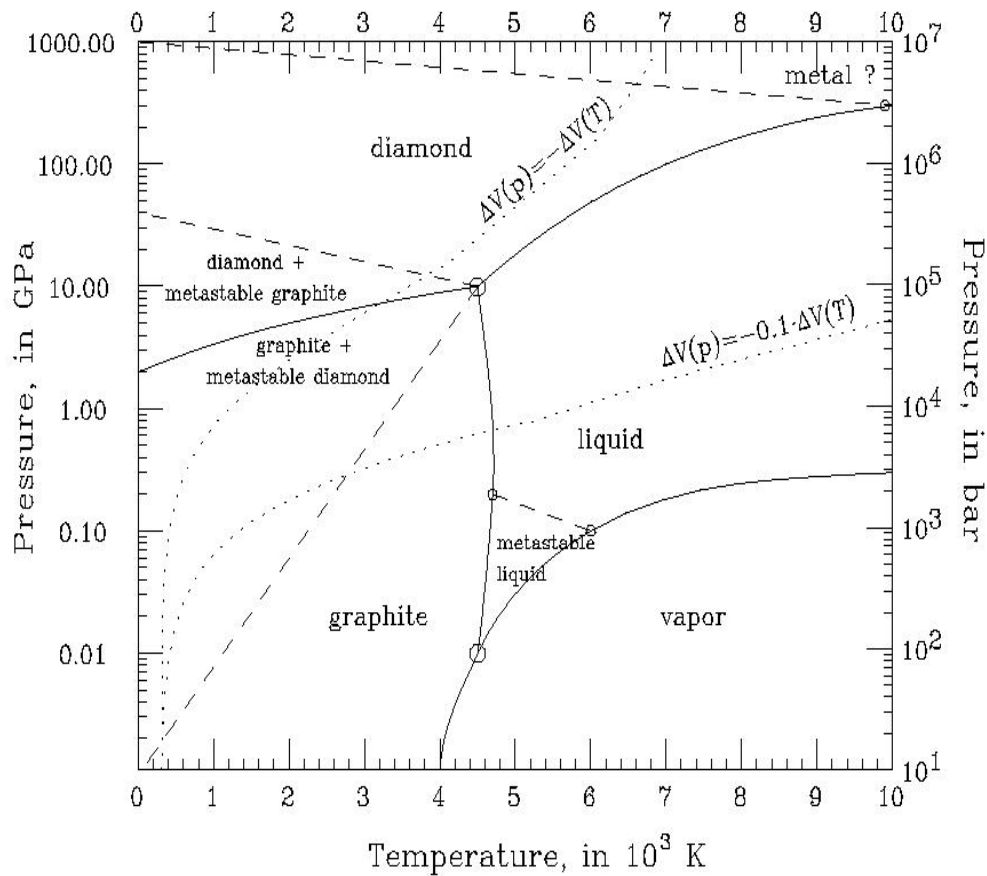


Figure 3.11 Pressure-temperature phase diagram of Carbon [94].

The boundary between graphite and diamond has been extensively studied and is given by [95]:

$$P(\text{GPa}) = 1.94 + 0.0025T(^{\circ}\text{C}) \quad (2.8)$$

The above relationship was determined based on experiments on growth and dissolution of diamond and graphite, accounting for the pressure effect on the EMF of a thermocouple [89].

Direct Conversion

There are two main ways to synthesize diamond without utilizing catalysts namely: static and dynamic compression. In static compression, 8 to 20 GPa of pressure and 1000 to 3000°C temperatures are required [96]. In order to generate such high pressures, a belt apparatus diamond anvil cell and multi-anvil apparatus are used. Electric current or a laser is applied for heating the sample.

Carbon sources that are commonly used for the synthesis are graphite, amorphous carbon, glassy carbon and fullerite C_{60} . Diamonds synthesized using such a method are typically less than 20 μm in size. Hexagonal diamond (Lonsdaleite) has been synthesized as well as cubic diamond [97].

Conversion to diamond has been detected even at room temperature using in-situ X-ray diffraction, but the diamond is not quenchable [98]. For this conversion, C_{60} was used as the carbon source and the diamond was recovered after a high pressure compression up to 20 GPa was applied at room temperature [97].

Dynamic compression techniques have produced diamond at pressure of 7 to 150 GPa. The temperature applied in the synthesis is a function of the initial sample density. Several carbon sources including graphite, C_{60} and Carbon nanotubes have been utilized for this purpose. The duration of loading is in most cases $\sim\mu\text{s}$ and the diamond synthesized has a grain size ~ 100 nm [89].

Well crystalline graphite enhances the formation of hexagonal diamond. This connection is consistent with the martensitic nature for the graphite-hexagonal diamond

transformation. In order to recover diamond irreversibly, it is necessary to heat the compressed sample up to about 1000°C [89].

There are several known materials that assist the conversion of graphite to diamond at lower temperature and pressure conditions (catalysts). Some of these include [96]:

- **Conventional catalysts**

Transition metals of group VIII elements (Fe, Co, Ni, Ru, Pd, Os, Ir, Pt), Mn and Ta. Ni, Co, Fe and alloys in which they are main constituents, are popularly utilized in the production of diamond. More than 10% of carbon dissolves into the molten metals. In this process, these catalysts act as carbon solvents.

- **Mg**

This plays the role of the solvent of carbon essentially at high temperatures where its carbide decomposes.

- **Oxygen containing materials**

Carbonates (CaCO_3 , etc), hydroxides (Ca(OH)_2 , etc.), sulphates (MgSO_4 , etc.), H_2O , kimberlite. Any compounds containing oxygen may be effective as catalysts except thermally stable oxides. Oxygen liberated from the compounds play an essential role for the diamond synthesis. The catalysts are likely to have a correlation with growth of natural diamond.

- **Hydrides**

LiH , CaH_2 . Micrometer sized crystals have been formed using such catalysts.

Figure 3.12 shows a region of diamond growth. This region is bounded by two lines, i.e. the diamond-graphite equilibrium line and a melting line where a liquid phase is formed

in the catalysts-carbon system. This region is applicable for the conventional catalysts [89].

Ni and Co have a eutectic relation with carbon, whereas Fe and Mn form stable carbides. In order to form the liquid phase at low temperatures, alloys of the metals are employed. 5-6 GPa and 1200 to 1500°C are the typical conditions for commercial production using the conventional catalysts [89].

Higher pressure is required to grow diamond at the low temperature range. The minimum temperature for growth is higher than the melting temperature of the catalyst at a given pressure. The minimum pressure and temperature for the growth is lowered by employing a seed crystal, indicating that the nucleation barrier is considerable for the formation of diamond [89].

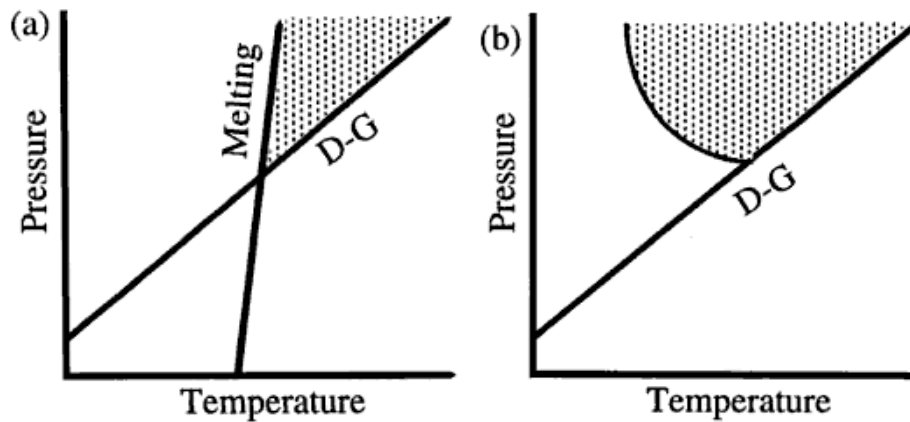


Figure 3.12 Schematic of diamond growth regions. (a) The diamond growth region using conventional catalysts. (b) The diamond growth region using non-metallic catalysts. Diamond grows in the shaded regions [89].

Atomic impurities incorporated into the diamond lattice are limited. Some of these atomic species together with their optical effects in diamond are described below [89]:

- **Boron**

Readily incorporated to produce a blue colour if boron-containing materials such as boron, boron nitride and borides are present in the growth cell. [99].

- **Nitrogen**

Largely responsible for the yellowish colour in diamond. Present in a wide range of concentrations from near zero to 800 ppm [100, 101, 102]. The diamonds grown from typical metal catalysts such as Ni, Co and Fe, contain 50-300 ppm of nitrogen. By adding nitrogen getters, Ti, Zr or Al, to the catalysts, the N concentrations are reduced to undetected levels, i.e. type IIa. Nitrogen is incorporated in single substitutional form, but nitrogen pairs are found in crystals grown at higher temperatures [103].

- **Nickel**

Produces a number of characteristic absorption and luminescence bands. With decreasing nitrogen concentrations, a brownish-yellow colour which is seen in a crystal grown of pure nickel, changes to green then brown. Electron spin resonance (ESR) studies have revealed that substitutional Ni and interstitial Ni⁺ are present in nitrogen rich and poor crystals respectively. Heat treatment produces complexes consisting of Ni, N and vacancies [104, 105, 106].

3.2.2 CVD diamond synthesis

Much progress has been made in the last decade to produce diamond using the chemical vapour deposition (CVD) techniques. Today, CVD diamond plates of more than 10 cm in diameter and more than 1 mm thickness are commercially available whose optical and thermal properties are comparable to the best single crystal diamonds [93].

The most important CVD techniques are hot filament and microwave assisted. However, this section will only focus on microwave assisted CVD for brevity. Single-crystal diamond has several outstanding physical and chemical properties such as the highest thermal conductivity at room temperature, the highest hardness, the highest Young's modulus and an ultrawide-band optical transmission range. Up to now, there exists a great industrial need for synthetic diamond, roughly 80 000 kg of synthetic diamond (HTHP) is used every year worldwide [93].

Microwave CVD

Along with HFCVD, it was microwave-plasma enhanced CVD (MPECVD) which moved diamond deposition from its niche of scientific curiosity into the area of industrially applicable technologies. It was first demonstrated by the group of Kamo *et al.* (1983) at MIRIM in Japan [107].

Generally, in the microwave-plasma diamond deposition reactor, process gases are introduced into a reactor chamber which contains the substrate to be coated. The chamber is an integral part of an electromagnet cavity and consequently its geometry has

a strong influence on the location and the extent of the microwave discharge. It is of great importance to create stable plasma which can be reproducibly controlled [93].

Typically the substrate to be coated with diamond is immersed into the plasma within this cavity. The microwaves couple energy into the electrons which in turn transfer their energy to the gas through collisions [108, 109]. As a result of these collisions, the process gas is heated and chemical reactions in the gas phase lead to the formation of diamond precursors which impinge on the substrate surface. If the surface conditions are carefully adjusted, diamond starts growing on the substrate [93].

The microwave plasmas are excited by 915 MHz (32.8 cm) and 2.45 GHz (12.2 cm). The choice of the very specific frequencies is mainly due to the availability of components that comply with national regulations. MPECVD is a very flexible technique in terms of the variety of gas precursors which can be used for diamond growth.

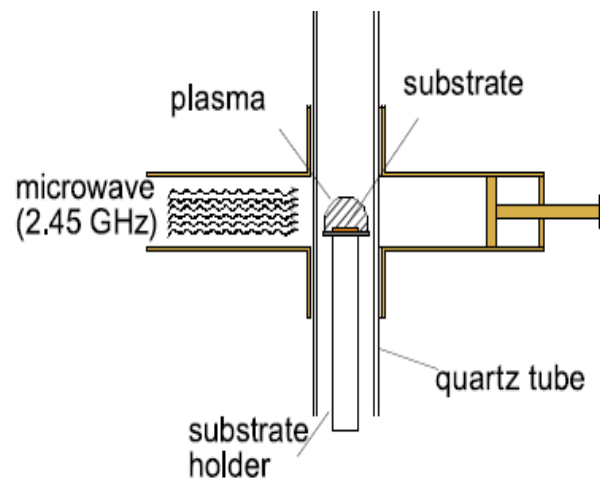


Figure 3.13 NIRIM-type reactor used by Kamo *et al.* [107].

In contrast to the HFCVD, where the admixture of aggressive reactant gases like oxygen or halogens would destroy the filaments, almost every conceivable gas mixture can be used [93]. The textured growth of CVD diamond films is dependent on only one parameter, the growth parameter α , which is defined as

$$\alpha = \sqrt{3} \frac{v_{100}}{v_{111}} \quad (2.9)$$

where v_{100} and v_{111} are the growth velocities on $\{100\}$ and $\{111\}$ directions respectively [93]. The growth parameter determines both the shape of the diamond nucleus and the texture of a polycrystalline diamond film. Experimentally, α is dependent on e.g. the methane concentration in the methane gas, the substrate temperature and gas impurities especially nitrogen and boron [93]. Figure 3.14 below shows diamonds of textures synthesized using the CVD method where concentrations of the input reactants were varied.

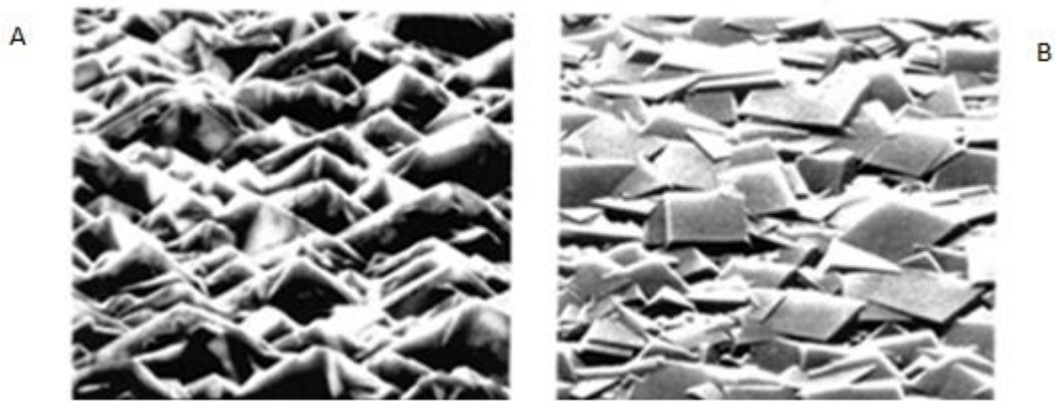


Figure 3.14 SEM images of CVD diamond films deposited at 800°C substrate temperature and 1.5% CH₄ in the reactant gas. A: $\alpha < 1.5$, concentration = 10 ppm B, scale: 13 mm = 3 μ m B: $\alpha > 2$, concentration = 60 ppm N, scale: 8 mm = 1 μ m [93].

3.2.3 Nanodiamond Synthesis Techniques

The first and most commonly used method for the synthesis of nanodiamonds is by explosive detonation of carbon based materials such as graphite and fullerenes. This method has been largely used for mass production of nanodiamond for industrial applications such as abrasives and wear resistant coatings.

Other diamond synthesis methods include (but are not limited to) synthesis by laser methods and synthesis by fast (and slow) ion irradiation. Although many synthesis methods are being explored as proof of principle, these vast techniques are also largely related to different desired applications.

Detonation Nanodiamonds

By comparing the explosive detonation parameters with the carbon phase diagram and performing calculations, it has been shown empirically and then theoretically, that free carbon in detonation products (DPs) of powerful condensed carbon-containing individual explosives with a negative oxygen balance should condense in a diamond or liquid phase [110].

A detailed mechanism explaining all the stages of UDD (ultrafine-dispersed diamonds) synthesis has not yet been proposed. Nevertheless, three stages can be distinguished in the detonation synthesis [110].

The stages are as follows:

- **First stage**

Transformation of the explosive under conditions of high pressure and temperature. Due to the detonation, free carbon must appear in DPs. The pressure and temperature in the detonation wave should provide the thermodynamic conditions necessary for conservation of the produced diamond phase and for preventing the diamond to graphite transition. For a 50/50 trotyl/hexogen (TH) mixture, these conditions take place at 22 GPa and 3200 K.

- **Second stage**

The DPs expand rapidly and diamond particles are cooled to a temperature lower than the graphitization temperature.

- **Third stage**

This stage is characterized by intense heat and mass exchange between the DPs and the medium surrounding the explosive. The main parameters determining the final temperature and the time after which this temperature sets in are the specific heat, the amount of substance and the chemical activity of the medium.

Experiments on UDD synthesis in various media have shown that the diamond yield depends on the gaseous medium in which the explosive detonates; the yield increases in the series vacuum-hydrogen-argon-nitrogen-carbon dioxide. Moreover, the diamond yield increases with the initial pressure of the gas filling the blast chamber.

Synthesis by Laser Ablation

There have been few studies involved in the transformation of graphite and amorphous carbon to nanodiamond [111, 112]. Liu *et al.* [113] conducted an experiment to probe the phase transition of amorphous carbon to nanodiamond by employing a unique laser induced reaction technique, i.e. pulsed laser irradiation in liquid [114].

In their experiment, amorphous carbon was converted into nanodiamond by pulsed-laser irradiation of amorphous carbon films in a confined liquid at room temperature and ambient pressure. Nanocrystalline diamonds (NCDs) with a size of about 4-7 nm were prepared in amorphous carbon films by the amorphous carbon-to-diamond conversion.

Their findings have applications field emission devices (FEDs) since NCDs embedded in amorphous carbon films can greatly improve the field emission performance by enhancing the emission site density (ESD) of the amorphous carbon cold cathode. The experimental approach is shown in figure 3.15 [113].

The amorphous carbon films with a thickness of about 700 nm were deposited on single crystalline silicon substrates using a filtered cathode vacuum arc (FCVA) technique at room temperature. Their apparatus included a Nd: YAG laser (wavelength of 532 nm, pulse width of 10 ns and power density of $5.7 \times 10^8 \text{ W/cm}^2$) and de-ionized water filled to about 3 mm above the amorphous carbon film.

Some results from their investigation are shown figures 3.16 and 3.17.

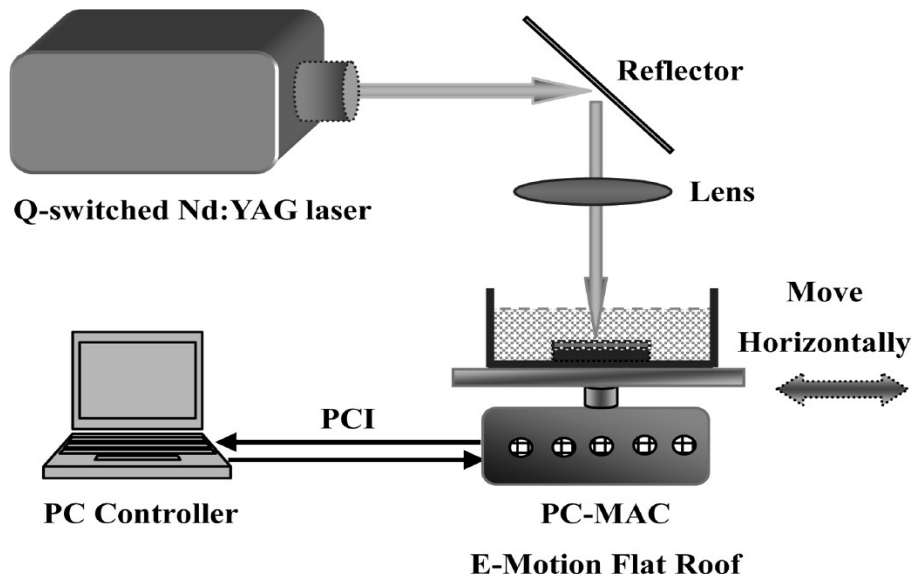


Figure 3.15 Schematic illustration of the experimental setup of laser irradiation in liquid [113].

Generally, laser induced plasma is first created at the liquid-solid interface when a pulsed-laser ablates the amorphous carbon layer. The plasma that contains various components of carbon species will be ejected from the laser-ablated amorphous carbon layer. Due to the laser induced pressure and the strong confinement of water, the laser-induced plasma is driven into a high-temperature, high-density and high-pressure state [113].

Water will dissociate into atomic H and O elements in the plasma plume [115, 116]. The presence of atomic H has been suggested to be of benefit to the nucleation and growth of diamond structured carbon in the liquid environment [117]. Therefore, some phase transitions from the sp^2 to the sp^3 phase of carbon could take place in the plasma plume [113].

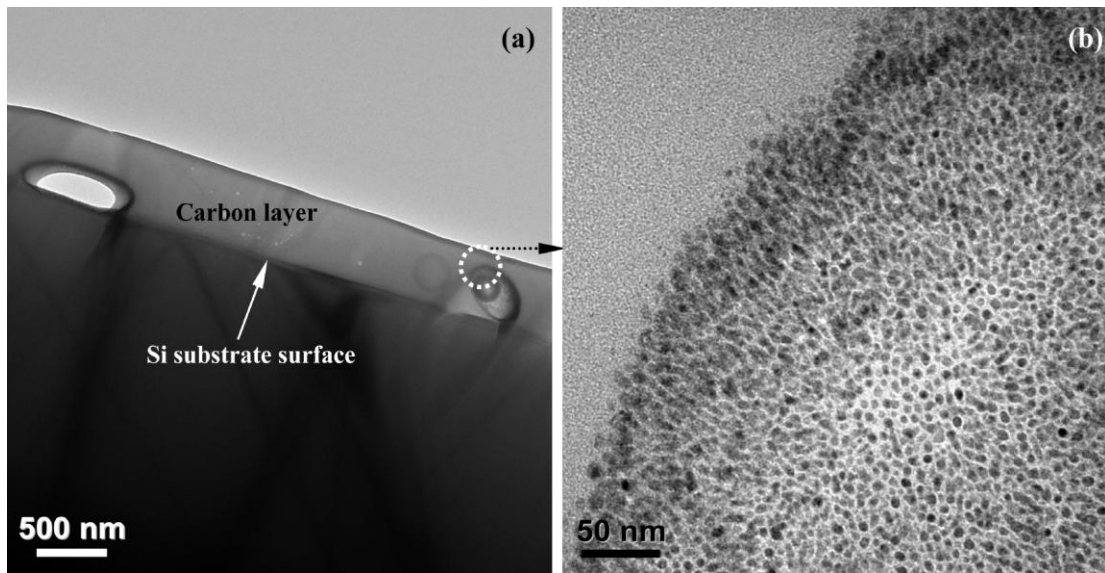


Figure 3.16 (a) Low-resolution TEM bright field image of the cross-section sample with two sites of the spatially periodic structure. (b) Detailed TEM image of one part of the condensed nanocrystals [113].

As a result of the liquid confinement, the quenching time of the plasma plume becomes so short that the metastable sp^3 phase could be frozen in the final products. In this particular study, the quenching time is ~ 20 ns, thus, NCDs immersed in amorphous Carbon can be reserved in the final products. The pulse-laser irradiation of amorphous carbon in liquid therefore creates a stable phase region of diamond nucleation as shown in this particular study [118].

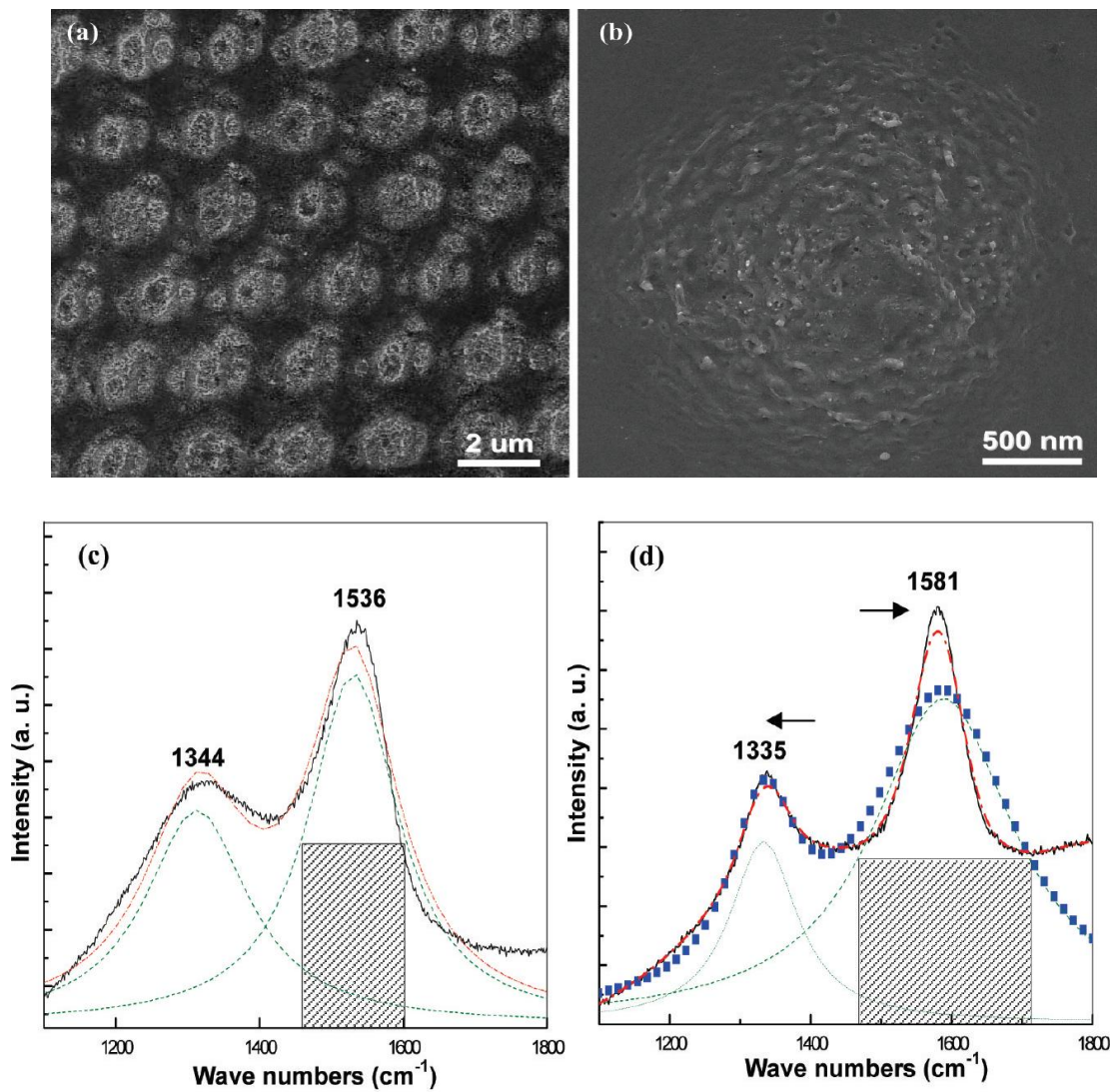


Figure 3.17 (a) SEM image of the spatially periodic array on amorphous carbon films induced by pulsed-laser irradiation in liquid. (b) Typical SEM image of one treated site. (c) Raman spectrum of the original amorphous carbon films, with the green dotted lines representing the result of a fitted-peak Lorentzian deconvolution. A hatched pane describes the FWHM of the G band. (d) Raman spectrum of the resulting sample, in which the shifts of the G mode and D mode are schematically depicted. The result of a fitted-peak Lorentzian deconvolution and a single skewed BWF line shape is describe by the green dotted lines and a blue symbol line, respectively [113].

Synthesis by Ion Irradiation

The transformation of sp^2 to sp^3 hybridization hardly occurs under normal conditions. However, such a transformation has been recently observed in materials irradiated with fast ion beams (high kinetic energy) [119, 120]. Banhart and Ajayan [121] used 1.2 MeV electron irradiation ($>10^{24} e^-cm^{-2} \sim 100$ dpa) to convert the cores of concentric-shell graphitic onions into nanometer-size diamond at irradiation temperatures above 900 K.

Following this experiment, many other successful experiments on nanodiamond synthesis using high kinetic energy beams with different singly charged ions were conducted. An important observation that emerges in studying several different irradiation experiments [121, 120, 122] is that nanodiamonds are formed under a surprisingly wide range of irradiation conditions. This observation led to the notion that nanodiamonds developed almost instantaneously in tracks generated by the high-energy irradiation particle [119].

The fact that nanodiamonds are formed under such a vast range of irradiation conditions may be related to a very small difference in the graphite and diamond free-energies at these temperatures coupled with surface-energy considerations that may make diamond the stable phase at very small particle sizes [123, 124]. Under particle irradiation, it is possible that both the stable (graphite) and metastable (diamond) phases can form simply because the difference in their respective free-energies is small, this has been observed in diamond films grown by chemical vapour deposition [121].

Daulton et al. [119] used an acid dissolution treatment to remove untransformed graphite and to isolate nanodiamonds from the ion-irradiated graphite specimens. The

acid residues were subsequently characterized by high resolution and analytical electron microscopy. Figure 3.18 shows a nanocrystal produced from such an irradiation.

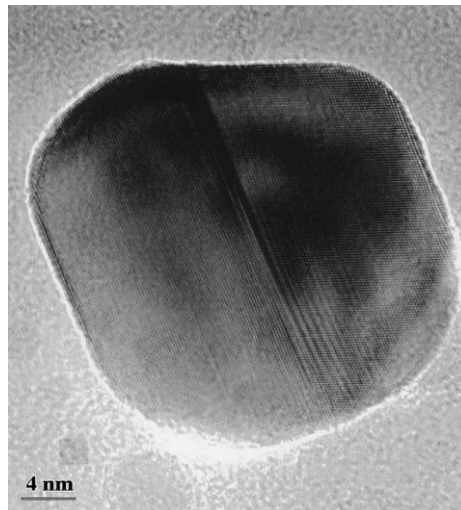


Figure 3.18 High-resolution lattice image of one of the larger nanocrystals found in the acid residue from the 350 MeV Kr irradiated graphite [119].

TRIM calculations of MeV singly charged ion beams in most materials (particularly carbon based materials) show that such high kinetic energy irradiation creates defects up to several microns below the surface. However, in the present study, focus will be on surface and near surface defects.

Contrary to high kinetic energy singly charged ions, slow highly charged ions (SHCIs) creates surface based defects. This is primarily because SHCIs have relatively low velocities (hence low kinetic energy). However, as described earlier, SHCIs are characterized by a large potential energy which is largely responsible for the formation of surface defects.

The high potential energy of SHCIs which induce multiple emission of electrons from the surface before a direct nuclear collision process, provides a strong modification of electronic states of the local surface area via the electronic excitation processes as similar to the fast ion beam irradiation. Meguro *et al* have demonstrated that the single impact of SHCIs converts sp^2 to sp^3 hybridization in HOPG on the nanoscale with subsequent processes such as electron injection and laser irradiation [125].

In their experiment, atomically flat terraces of HOPG were irradiated with slow Ar^{q+} ($q=1-8$) ions with 400 eV of kinetic energy directed onto the HOPG surfaces. After the irradiation, the samples were treated by electron injection and He-Cd laser irradiation in order to complete the transformation from sp^2 to sp^3 . While electron injection had to be carried out on each SHCI impact area one after the other by means of a scanning and tunneling microscope (STM), the He-Cd laser irradiation was able to collectively convert the entire impact region on the HOPG surface. However, no difference in the two post-treatment methods was observed [125].

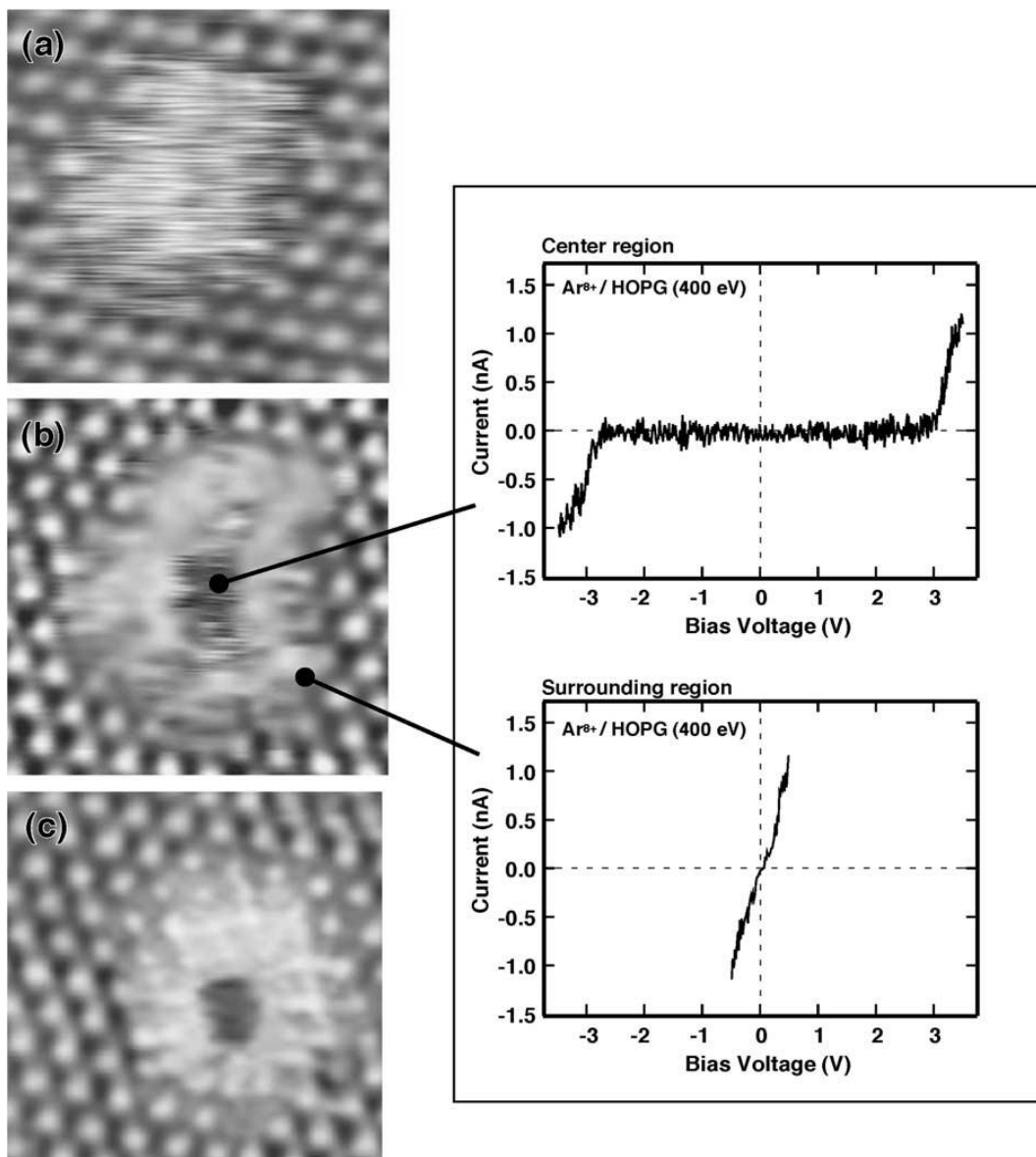


Figure 3.19 Images (a), (b) and (c) are STM images of the Ar^{8+} impact region. (a) As irradiated (metallic). (b) After electron injection (non-conductive) and (c), after the subsequent hydrogen treatment (non-conductive). Right side curves are I - V characteristics inside and outside of the Ar^{8+} impact region measured by STS [125].

Multiple electron emission and the resulting hole accumulation play an important role in the transformation from metallic to non-conductive regions as seen in I-V curves shown in figure 3.19. During the neutralization process via diffusion of electrons, the reconstruction of bonds occurs and the nanoscale sp^3 regions are created because they are the energetically most preferred phase on the nanoscale. Diamond has been reported to be more stable than graphite at the nanoscale (~ 3 nm diameter), even under ambient pressure [126].

Another possibility recently proposed is that the depletion of electron drives a lowering of the potential barrier of the transformation; e.g. when depleting ~ 0.1 electrons/atom, the barrier for the transformation from graphite to diamond is expected to disappear, which is normally 0.29 eV in neutral conditions [127].

Both models are based on the formation of multiple holes which is caused by the large potential energy characteristic of SHCIs. However, in either model, no post process such as electron injection is necessary, while the actual transformation cannot be completed without electron injection or He-Cd laser irradiation [16].

3.3 The Nitrogen Vacancy Center in diamond

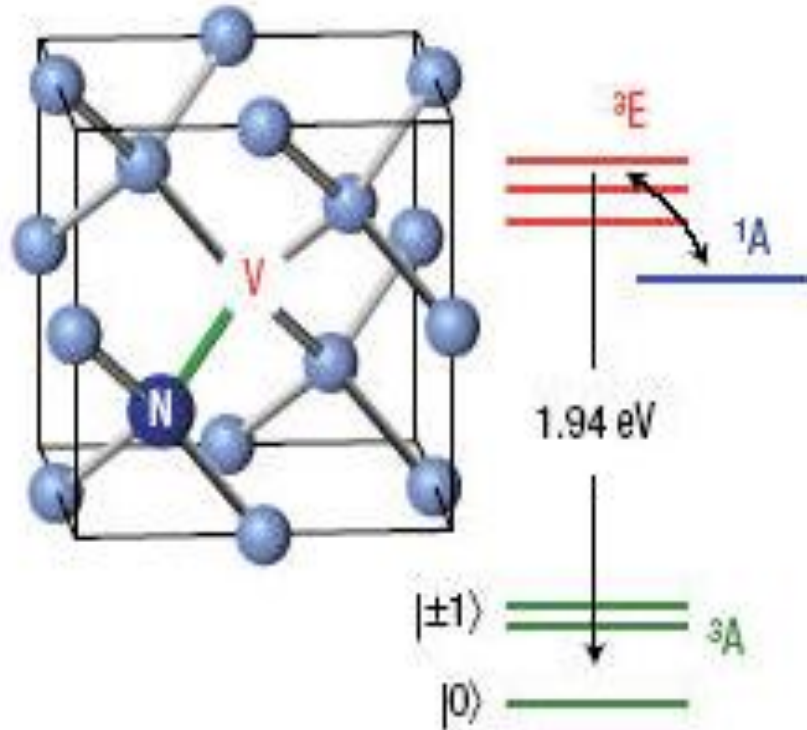


Figure 3.20 Diagram showing the nitrogen-vacancy complex in diamond (left) and the corresponding energy level schematics (right) [128].

Natural (and synthetic) diamond usually contains nitrogen impurities. One such impurity that is commonly encountered in photoluminescence studies of diamond is the N-V luminant centre. The N-V center (in diamond) consists of a substitutional nitrogen atom sitting next to a vacant site in the diamond lattice (see figure 3.20).

The empirical introduction of N-V centers in the diamond matrix can be achieved with high accuracy and precision using specialized equipment such as the EBIT shown in figures 4.1, 4.2 and 4.3. Although this method can pattern N-V centers with high spatial accuracy and precision, subsequent annealing is usually necessary to provide the necessary energy so that vacancies in diamond can be mobile and thereby increase the probability of creating N-V sites.

The ground state of the N-V center is a spin triplet (3A) and shows a zero field splitting between the $|m_S = 0\rangle$ and $|m_S = \pm 1\rangle$ spin sublevels where m_S is the quantum number of the spin sublevel, quantized along the symmetry axis of the N-V center, along the $\langle 111 \rangle$ crystal axis [130]. The N-V state can be detected through photon antibunching measurements and ESR measurements that reveal a zero field splitting around 2.88 GHz corresponding to the ground state splitting (figure 3.21 c) [29].

The N-V⁻¹ shows an allowed optical transition with the zero phonon line (ZPL) at 638 nm which is very stable (see figure 3.21a). The average photon emission rate is substantially small for emissions involving $m_S^{NV} = \pm 1$ levels than for the $m_S^{NV} = 0$ level. This allows readout of the spin state by the photoluminescence intensity, I_{PL} . Thus, tuning radio frequency (RF) waves to precise excitation frequencies can alter the N-V centers between states 0 and 1 passing through transitional states that are quantum superpositions of the 0 and 1 states [29].

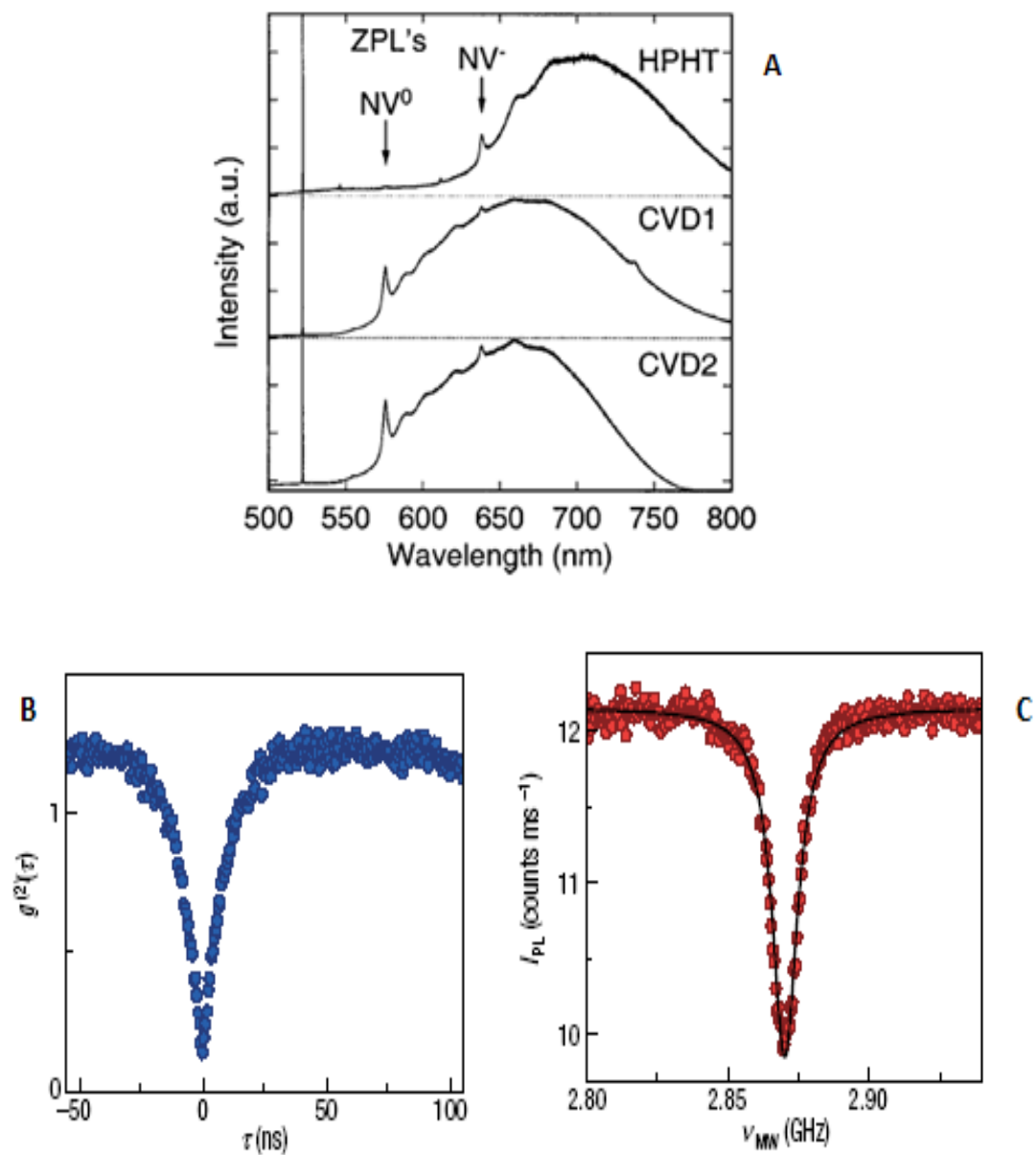


Figure 3.21 (A) PL data for N-V centers in diamond under 488 nm laser excitation. (B), (C) photon correlation and ESR measurements, respectively, showing the zero field splitting of the ground state of the N-V center [128].

Therefore, there exist several experimental “knobs” that can be used to study and manipulate the spin state of the N-V center, these include: magnitude and angle of the applied magnetic field, the power and duration of the optical excitation and the radio frequency (RF) magnetic fields for coherently rotating the electron and nuclear spin [130].

Spin-spin and spin-lattice relaxation times are strongly affected by the coupling of the spin being probed due to its environment. Due to the weak spin-orbit coupling in diamond, the single spin of an N-V center is only weakly coupled to its environment (diamond lattice). Spin coherence times of $\sim\mu\text{m}$ have been measured for the N-V center in a high purity single crystal diamond at room temperature [29].

However, in order to create N-V luminant centers that useful for practical information processing, other impurities that are commonly found in diamond have to be kept at a minimal level to reduce the effect of the environment (quantum noise). These properties of the N-V center meet several requirements for practical quantum computing. Hence, the N-V center in diamond has emerged as a possible solution in the continuing search for advanced materials that are necessary to carry out room temperature quantum computing.

Quantum error correction serves to protect quantum information from errors due to decoherence and other quantum noise. Quantum error correction is essential if one is to achieve fault-tolerant quantum computation that can deal not only with noise on stored quantum information, but also with faulty quantum gates, faulty quantum preparation and faulty measurements.

3.4 Introduction to Quantum Computing

In the early 1980s, the idea of the quantum computer was introduced by Benioff [131] and Feynman [132]. They showed that bits represented by quantum mechanical states can evolve under action of quantum mechanical operators to provide reversible computation. In 1994, an explosion of interest in quantum computation was caused by Shor's discovery of the first quantum algorithm which can provide fast factorization of integers [133]. In 1998, Kane proposed the first silicon solid state quantum computer [134].

A quantum computer is intended not for accelerating digital computation using quantum effects, but to utilize new quantum algorithms which were not possible in a digital computer. In a quantum computer, information is loaded as a "string" of quantum bits – "qubits". A qubit is a quantum object, e.g. an atom (an ion) which can occupy different quantum states [135].

The main advantage of quantum computing is not only the density of qubits but rather that quantum physics allows one to operate with a superposition of states. For one atom, one can produce an infinite number of superpositional states using two basic quantum states, which correspond to "0" and "1" [135].

Utilization of superpositional states allows one to work with quantum states which simultaneously represent many different numbers. This phenomenon is known as "quantum parallelism". Major limitations with classical computers are associated with their inability to solve intractable problems, these are problems which do not have an

efficient algorithm [135], e.g. it can thousands of years for powerful digital computer to factories a 200 digit number.

The first two-qubit quantum logic gate was demonstrated experimentally by Monroe *et al.* in 1995 [136]. They used the Cirac-Zoller scheme for a single B^+ ion in an ion trap. The interaction with the environment quickly destroys superpositional states. This phenomenon of losing quantum coherence is termed “decoherence”. Therefore quantum computing must be done in time scale less than the time of decoherence. The characteristic time scale of decoherence depends not only on temperature but also on the system under consideration.

In quantum information theory, the 0 and 1 states used in classical computers are replaced by orthonormal basis vectors $|0\rangle$ and $|1\rangle$ of a qubit in the form $|\psi\rangle = \alpha|0\rangle + \beta|1\rangle$, where $|\alpha|^2 + |\beta|^2 = 1$. It is estimated that a quantum computer superior to a digital computer today requires at least $10^2 \sim 10^3$ qubits [137].

Successful implementation of a “practical” quantum computer has some basic requirements. These are requirements are summarized by the DiVincenzo criteria [137] and are listed below:

- **A scalable physical system with well characterized qubits.**

A quantum register made of many qubits is required for information storage. The simplest way is to use a two level quantum system, e.g. an electron, a spin $1/2$ nucleus and two polarization states of a single photon may be a qubit. The

system should be scalable up a large number of qubits. The condition of two states may be relaxed to three states (qutrit) or more generally, d states (qudit).

- **Long decoherence times, much longer than the gate operation time.**

Decoherence means many aspects of quantum state degradation due to interaction of the system with the environment and sets the time available for quantum information. Roughly speaking, this is the time required for a pure state

$$\rho_0 = (\alpha|0\rangle + \beta|1\rangle)(\alpha^*\langle 0| + \beta^*\langle 1|) \quad (2.10)$$

to “decay” into a mixed state of the form

$$\rho = |\alpha|^2|0\rangle\langle 0| + |\beta|^2|1\rangle\langle 1|. \quad (2.11)$$

In fact, decoherence time itself is not very important, what matters is the ratio “decoherence time/gate operation time”. For a typical gate operation time \sim ps, the system may execute 10^6 gate operations before the quantum state decays.

- **Initial state preparation**

It should be possible to set qubits to the zero state before each new calculation.

- **Gate Implementation**

The states of the individual qubits need to be manipulated with reasonable accuracy and interactions between the qubits need to be induced in a controlled manner to enable quantum gate implementation. The gate implementation time must shorter than the time for decoherence.

- **Readout**

It must be possible to read out the final states of the qubits once the computation is completed.

The prospect of using the N-V center for achieving room temperature quantum computing has constituted the major motivation for the present investigation. The ability to possibly synthesize nanodiamonds in a controlled manner in the form of qubit arrays by using single ion implantation techniques at the Electron Beam Ion Trap (EBIT) facility (described in the next section), could allow one the unique opportunity to produce nanoarrays of N-V centers localized in nanodiamond matrices which can ultimately be scaled up to produce a functional solid state quantum computer.

Chapter 4

4. Experimental Procedures

4.1 Electron Beam Ion Trap (EBIT)

An electron beam ion trap (EBIT) is a device that can make and trap very highly charged ions by means of a high current density electron beam. The ions can either be studied in the trap itself or be extracted from the trap for external experiments.

The EBIT was first developed at the Lawrence Livermore National Laboratory by Mort Levine and Ross Marrs. A high energy modification to the original EBIT has also been developed and is called super-EBIT. Super-EBIT is capable of producing bare uranium, U^{92+} , which had never been accomplished before without the use of high-energy particle accelerators [138].

The advantage to EBIT creating such high energy ions is that the ions are practically at rest, something that cannot be accomplished by accelerators which accelerate the ions to very high energies. EBIT consists of a high current density electron beam which can be up to 5000 A/cm^2 , which is passed through a series of three drift tubes (see figure 4.1).

The drift tubes are basically a set of three cylindrical copper tubes. The beam is guided, accelerated and focused by magnetic fields and high voltage electrodes. The electron beam energy in the trap is determined by the positive voltage bias applied to the central drift tube. The electron beam is magnetically compressed from a diameter of 1 mm to less than 100 μm by a high magnetic field from a pair of superconducting Helmholtz coils [138].

Ions are trapped radially by the space charge of the electron beam itself and axially by voltages applied to the drift tubes (see figure 4.1). The magnetic field also helps with the confinement.

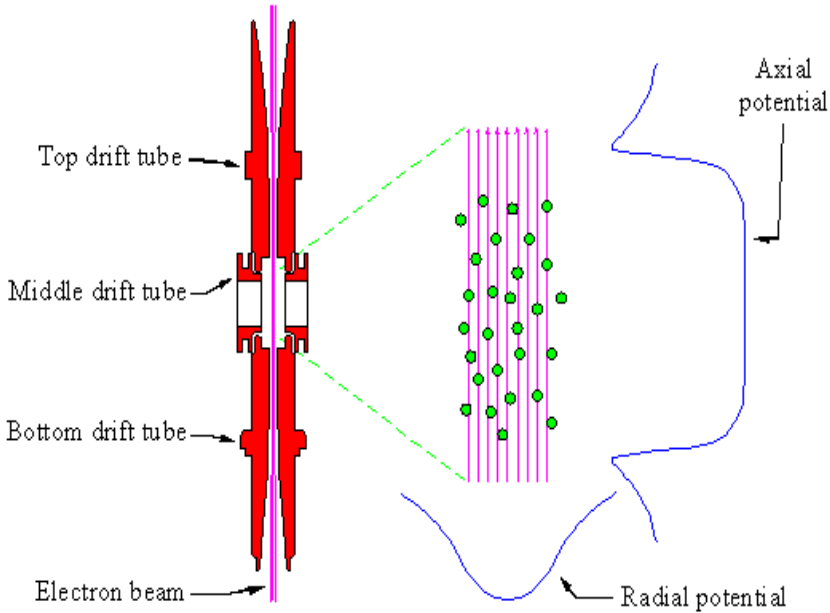


Figure 4.1 The drift tubes of EBIT focusing the electron beam [138].

The electrons will collide with the ions in the beam and will therefore strip off the ion's electrons until the energy required to remove the next electron is higher than the beam energy. The original EBIT can have a beam energy of 30 keV which can create a uranium atom with only 10 of the usual 92 electrons.

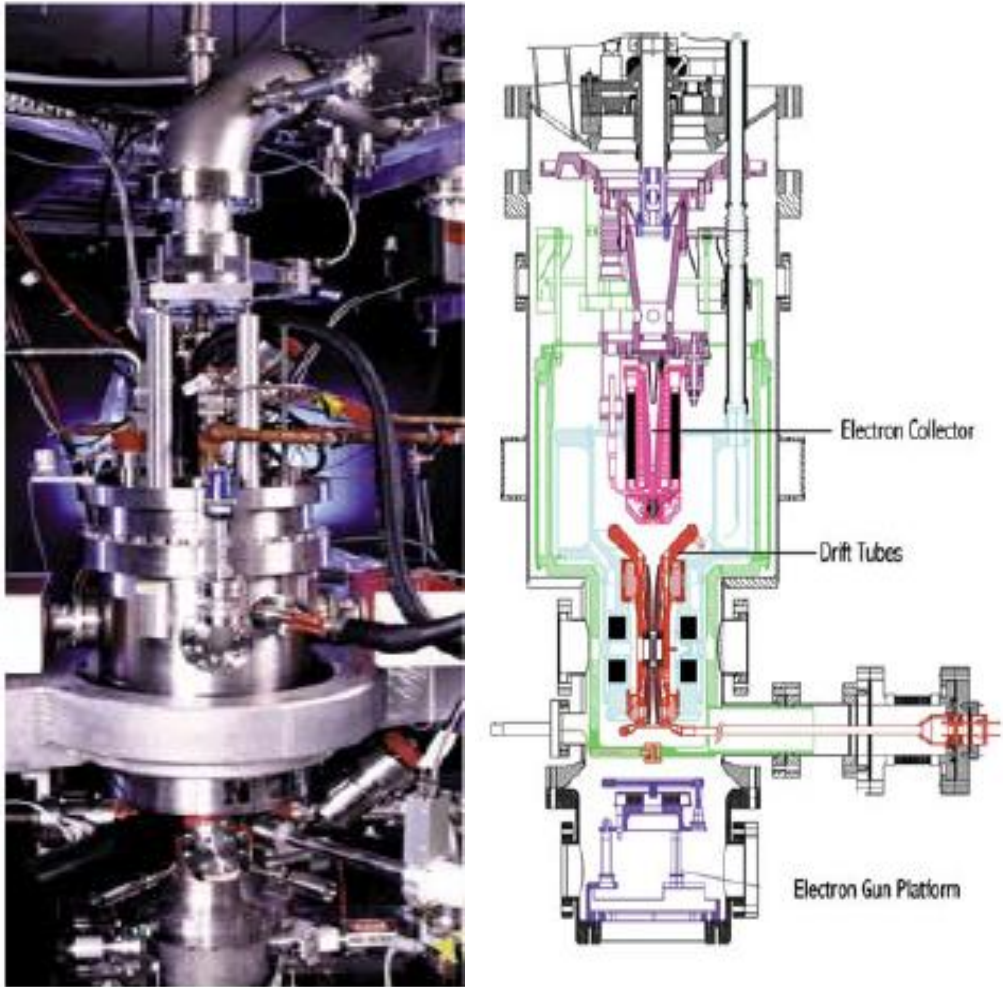


Figure 4.2 Diagrams showing the electron beam ion trap at the NIST EBIT, the main region is ~1m in length [139].

The electron beam is the primary component of the EBIT and performs three functions: it creates the highly charged ions by removing electrons via electron impact ionization; it traps the ions by providing a potential in the radial direction and it excites transitions in the ions where radiation is released which allows them to be studied spectroscopically.

Figure 4.3 shows the target chamber where samples are mounted. It is in this part of the setup where the projectile SHCIs can be biased to a given kinetic energy. This kinetic energy is a function of the charge state of the SHCIs. This is because the kinetic energy impinging on the surface of the target is given by

$$E_{kin} = q \times E_{Bias} \quad (4.1)$$

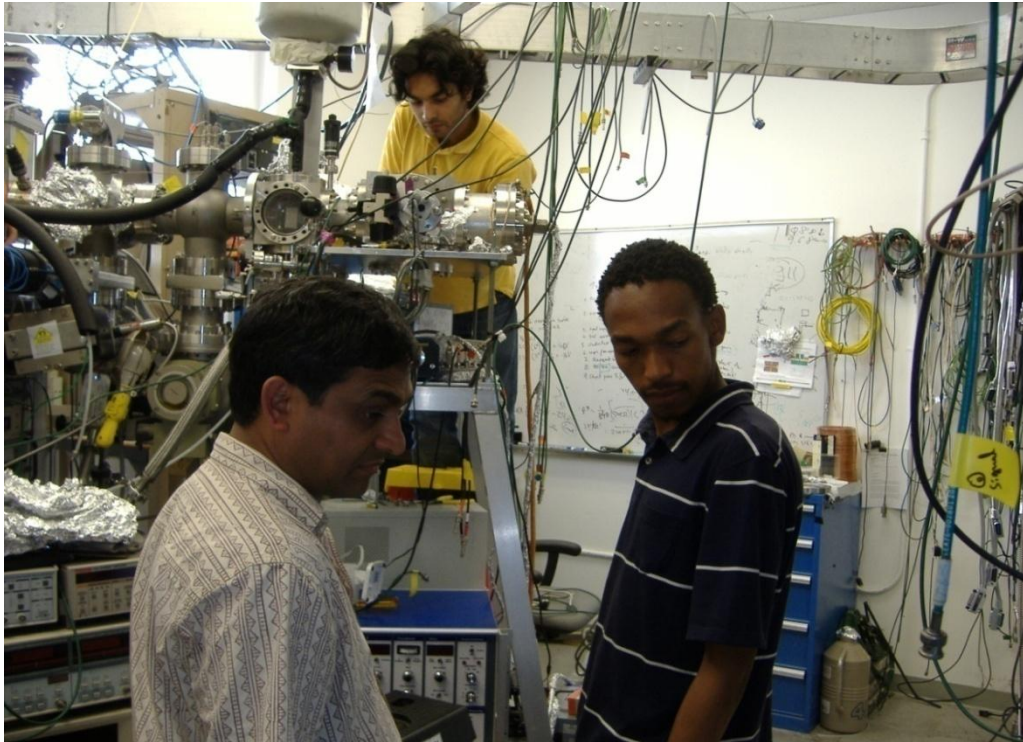


Figure 4.3 Diagram showing the target chamber at Berkeley EBIT.

A closer view of the target chamber at Berkeley EBIT is shown below in figure 4.4.

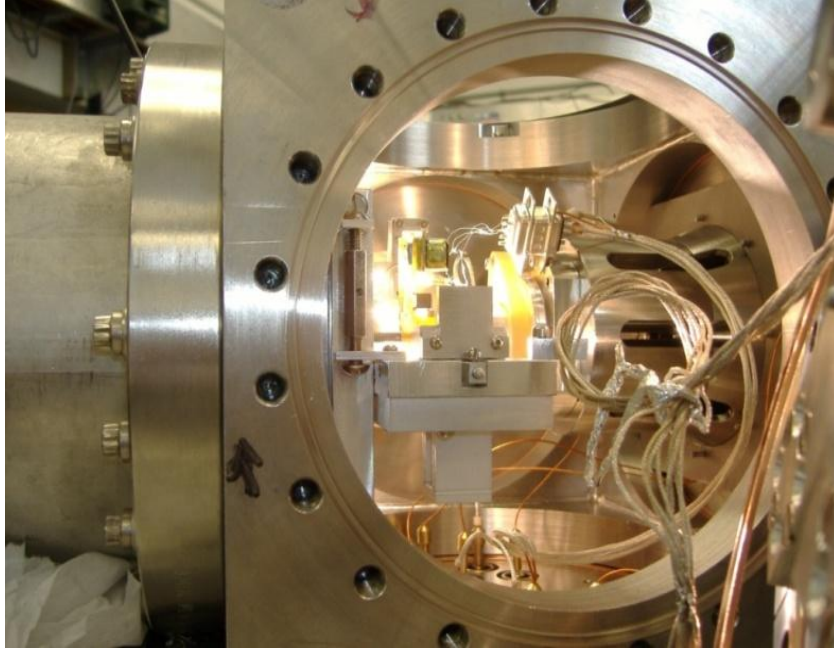


Figure 4.4 A closer view of the target chamber shown in figure 4.3.

There is a wide range of applications for local modification [140] of surfaces with scanning probes e.g. deposition of metal lines through nanostencils [141] and also the precise alignment of single ions on a large array to achieve a quantum computer with several qubits. The target chamber shown above in figure 4.4 has been recently combined with a scanning probe (atomic force microscope, AFM) alignment system to achieve such diverse functionality [142].

In this setup, the alignment is achieved by incorporating a scanning probe into the beamline which is used for ion implantation. The tip of the scanning probe also

functions as a beam spot defining aperture by including a small hole through which the ions will be implanted into the target material. Holes in scanning probe cantilevers as small as 5nm have been achieved by focused ion beam (FIB) drilling followed by local ion beam assisted thin film deposition of Pt or SiO₂ to reduce the hole radius to the desired radius (figure 4.5) [142, 143].

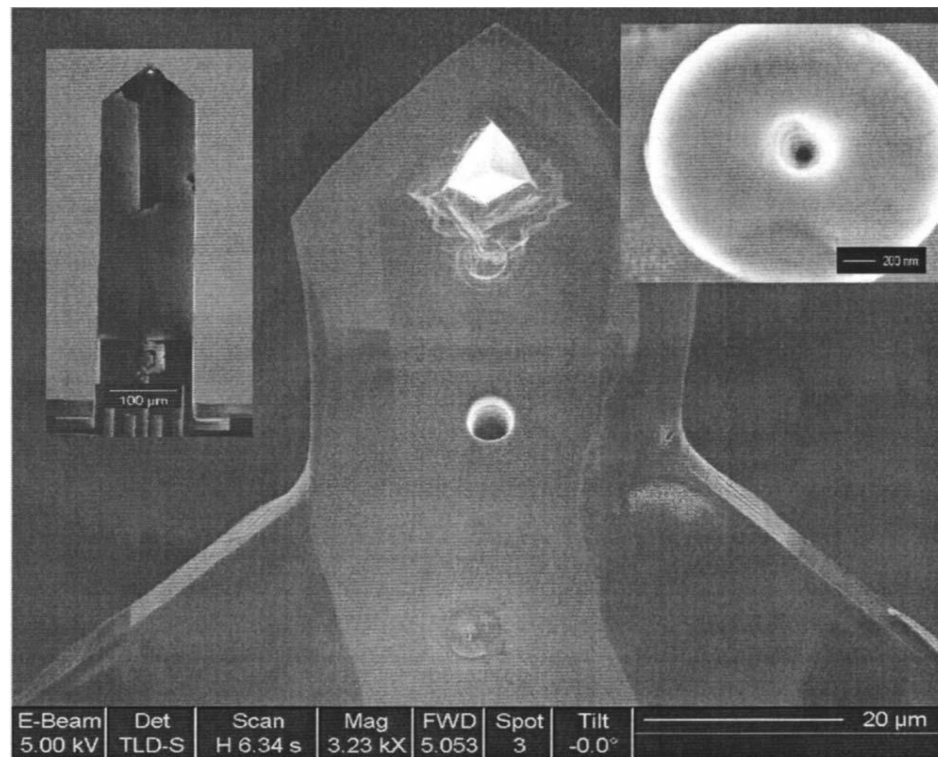


Figure 4.5 FIB processed tip. Three holes of different sizes ranging from 1 μm to 100 nm have been drilled on the cantilever. The left insert shows the whole cantilever with the Wheatstone bridge at the bottom. The right insert shows a larger view of the upper 100nm hole [142].

During scans, the AFM cantilever is held in a fixed position and the stage is moved to acquire the scan image (see figure 4.7). For coarse motion and alignment, the cantilever itself is mounted on a flexure stage and can be positioned freely over the region of interest. The flexure stage is also used to achieve the coarse approach of the tip to the surface [142].

A piezoresistive readout scheme is used to sense the deflection of the cantilevers when imaging the target surface. The cantilevers have a Wheatstone bridge built in [144, 145] and a vacuum preamplifier (X10) integrated close to the cantilever. A second amplification stage (X10 – X5000) outside the vacuum is used in combination with a low pass filter before the signal is fed into the control hardware for the feedback loop [see figure 4.6].

The technique of scanning probe microscope (SPM) tips using a nanoaperture has the advantage of being able to collimate nearly all ion species, this collimation can even take place at a kinetic energy of 1 keV or below. Assembling of nanoclusters or molecules is thus a possibility [146].

By incorporating a single ion detection system into the apparatus, the number of implanted ions can be controlled exactly. At the Berkeley EBIT, this functionality is achievable by detection of secondary electrons from the surface or electron/hole pairs created in the target material. The use of SHCIs leads to several orders of magnitude higher signal and therefore makes the detection of every single ion easier [147, 148].

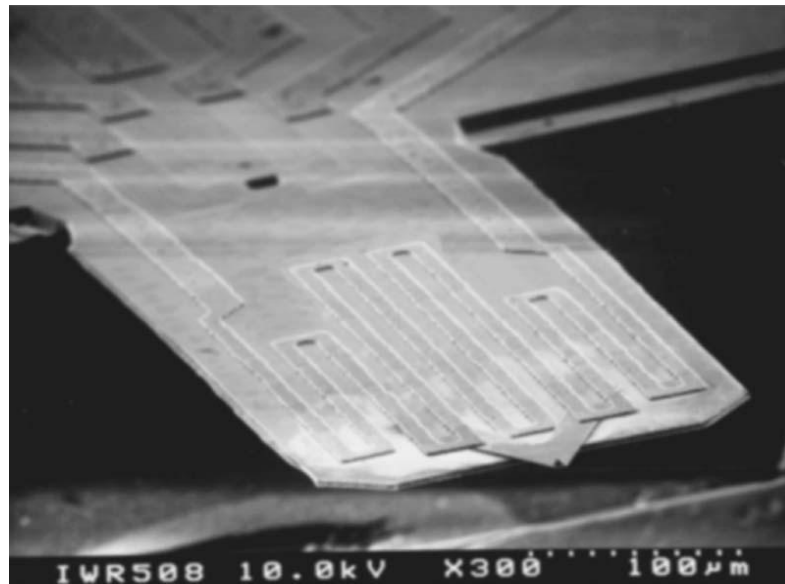


Figure 4.6 Cantilever with integrated piezoresistive Wheatstone bridge, bimorph actuator and AFM tip [146].

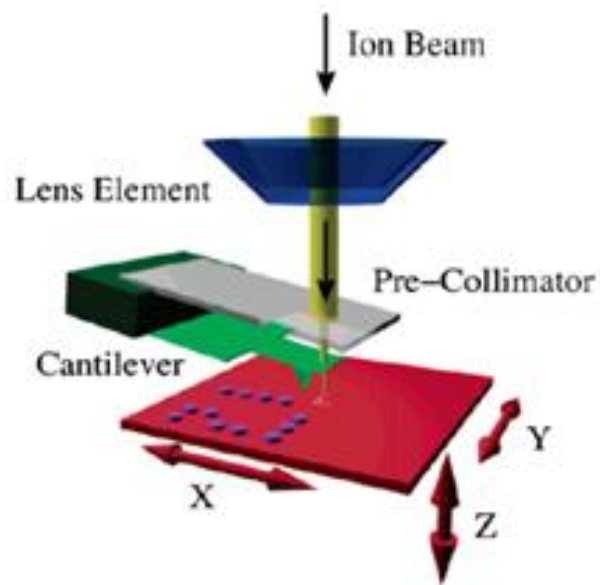


Figure 4.7 Simplified diagram showing the surface patterning system at Berkeley EBIT. Note, the cantilever can be positioned anywhere relative to markers on the sample and revisit any spatial location in a predetermined manner [142].

4.2 SHCI Implantation Details

Slow Highly charged Antimony ions were extracted from the EBIT and reached the target chamber after momentum analysis in a 90° bending magnet. The vacuum pressure inside the target chamber was 10^{-7} - 10^{-8} torr. The ion kinetic energies (see equation 4.1) were set by the EBIT extraction potential of 5 keV and these are: 40 keV, 90 keV and 110 keV for Sb^{8+} , Sb^{18+} and Sb^{22+} respectively.

The HOPG sample that is used in this work was cleaved with an adhesive tape to expose atomically flat terraces necessary for subsequent AFM/STM analysis. The sample was then implanted with Sb at different spatial coordinates with varying charge states: Sb^{8+} , Sb^{18+} and Sb^{22+} as shown below in figure 4.8. The irradiation dose was approximately 100 ions/ μm^2 , and was kept constant at for all implants. The ions impinged on the HOPG surface under normal incidence. The ion currents were 33 pA, 54 pA and 2.8 pA with corresponding exposure times of 90 s, 60 s and 20 min. respectively.

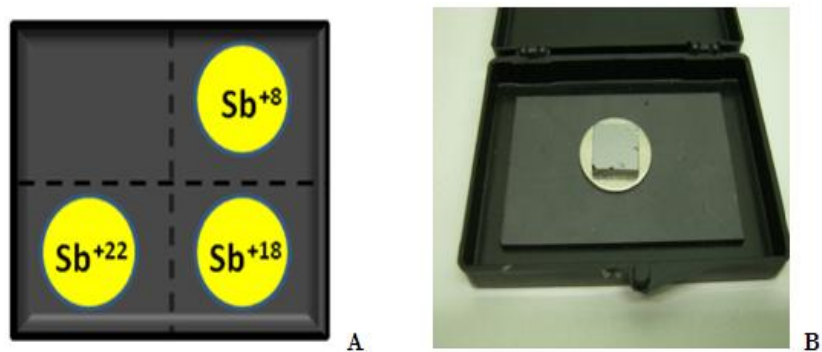


Figure 4.8 Implantation scheme adopted at EBIT (Berkeley) on HOPG (A). One quadrant was left unexposed for reference. The actual HOPG sample is shown in B, the HOPG was kept closed in the holder when not in use to avoid surface accumulation of water vapour from the air.

4.3 Monte Carlo Simulations (MC)

SHCIs projected onto surfaces are associated with a given kinetic energy. This kinetic energy is characterized by the lower limit of the SHCIs set by the Coulomb force and also the extraction potential (see equation 4.1). The neutralisation of SHCIs is a function of its kinetic energy loss and potential energy loss. The stopping of singly charged ions in matter has been extensively studied by several authors [40, 43, 46, 47].

Monte Carlo simulations which follow the ion into the target, making detailed calculations of the energy transferred to every target atom collision have been designed. The SRIM/TRIM software package [149] is an example of such a design. SRIM/TRIM is commonly used in implantation studies to predict the range of singly charged ions in matter.

Using TRIM, one can compute both the final 3D distribution of the ions and also all kinetic phenomena associated with the ion's energy loss: target damage, sputtering, ionisation, and phonon production [149]. A more comprehensive estimation of the range of SHCIs in matter would have to consider the large potential energy commonly associated with SHCIs. As discussed in chapter 2, several authors have designed models that predict the interaction and range of SHCIs in matter; however, this is still a subject of ongoing investigation.

The MC results for the implantation scheme used in this work are shown below where the calculated ranges are purely due to kinetic effects. Plots are shown for an example of the implantation of the highest charge state of Antimony ($q = 22+$) with a

corresponding kinetic energy of 110 keV. Similar calculations for other charge states have been computed and the output parameters are shown in table 4.1.

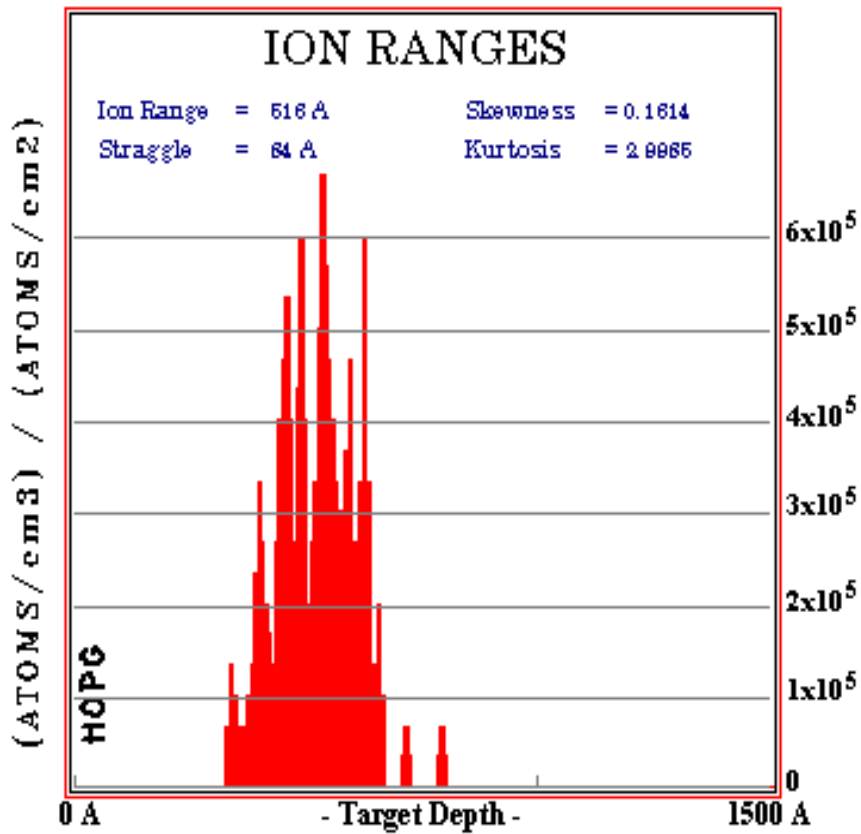


Figure 4.9 Monte Carlo simulations of the ranges of Sb (110 keV) ions in HOPG.

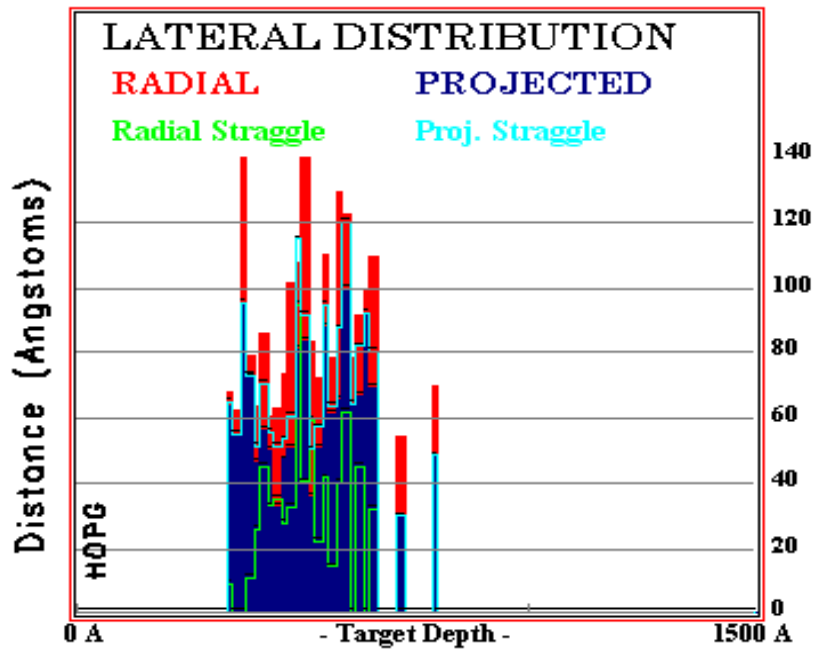


Figure 4.10 Monte Carlo Simulations of the lateral distribution of Sb (110 keV) ions in HOPG.

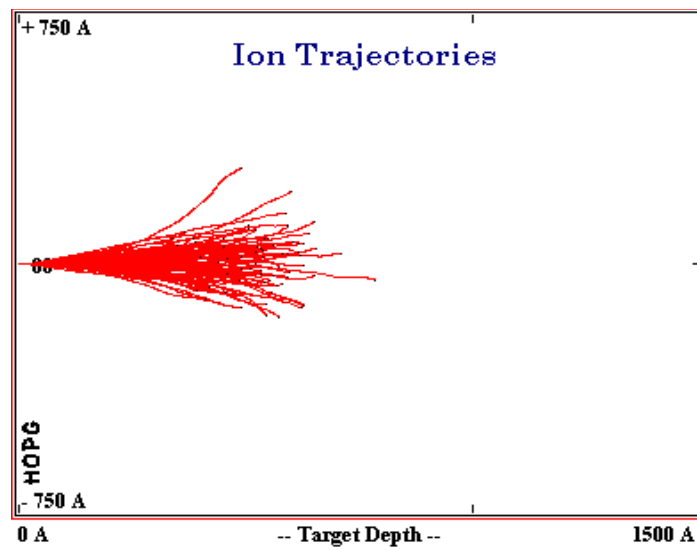


Figure 4.11 Monte Carlo simulations of the trajectories of Sb (110 keV) ions in HOPG.

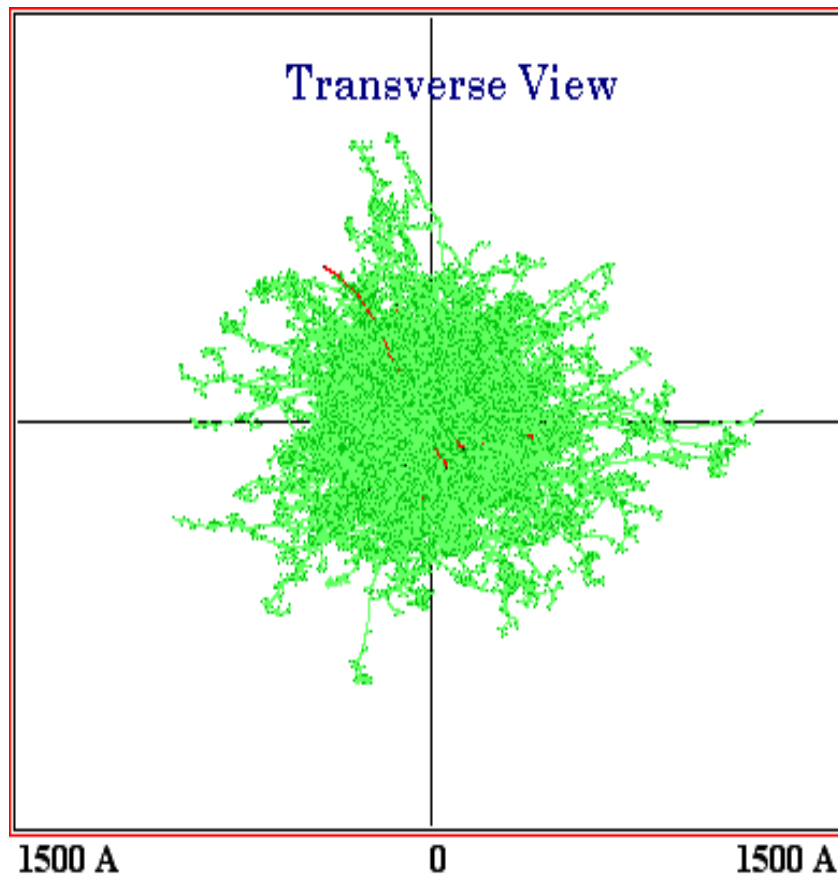


Figure 4.12 Transverse view of the Sb (110 keV) ion trajectories using Monte Carlo simulations.

Figures 4.9 to 4.12 are examples of results of the implantation of Sb (110 keV) ions into HOPG using Monte Carlo simulations. Table 4.1 below shows the results for all charges studied including Bismuth ($q = 35$). The extraction voltage for all ion species is 5 kV.

The parameters shown in table 4.1 namely the straggle, vacancies per ion and the range offer important information regarding the implantation. In this simulation, the vacancies created during the interaction are due to radiation damage resulting from kinetic effects.

This damage occurs by means of dislocations of atoms from initial positions in the ideal lattice structure.

The data for the vacancies created is presented in vacancies per ion therefore; the total vacancies created due to kinetic effects from each implantation are a factor of 100 larger than the displayed values. The straggle of the ions in matter represents a characterization of the 3D spreading of an ion beam in matter. Whereas an approximately linear variation of range and the damage is observed as a function of charge, no obvious correlation can be assumed for the straggle of ions with respect to charge state as seen in table 4.1.

Table 4.1 Implantation results for all investigated ion species using MC simulations.

Parameter	Bi ^{+q}	Sb ^{+q}	Sb ^{+q}	Sb ^{+q}
Charge state (q)	35	22	18	8
Kinetic energy (keV)	175	110	90	40
Range (Å)	559	516	460	274
Vacancies/ion	1411	1021	870	447
Straggle (Å)	70	84	89	47

4.4 Scanning Probe Microscopies (SPM)

Scanning probe microscopies (SPM) refer to fine scale (nm- μm range) imaging and surface characterisation techniques which operate primarily by scanning a sharp tip ($\sim 3\text{-}50$ nm radius of curvature) over a solid or liquid phase surface. Some SPM techniques include: Atomic Force microscopy (AFM), Magnetic Force Microscopy (MFM), Scanning and Tunnelling Microscopy (STM) and Scanning and Tunnelling Spectroscopy (STS), however, this work will focus on AFM and STM/STS techniques which have been utilized in the characterization of our HOPG sample.

4.4.1 The Atomic Force Microscope (AFM)



Figure 4.13 The Dimension 3100 AFM/MFM apparatus on a vibration isolation table.

The atomic force microscope (AFM) probes the surface of the sample with a sharp tip. The tip, a couple of microns long and normally less than 100 Å in diameter, is located at the free end of a cantilever that is 100 to 200 μm long. The tip is either scanned over the sample or the sample is scanned over the tip. Forces between the tip and the sample surface cause the cantilever to bend or deflect, a detector then measures the cantilever deflection, this measured deflection then allows a computer to generate a map of a surface topography [150]. A schematic diagram of the general operation of AFM is shown below in figure 4.14.

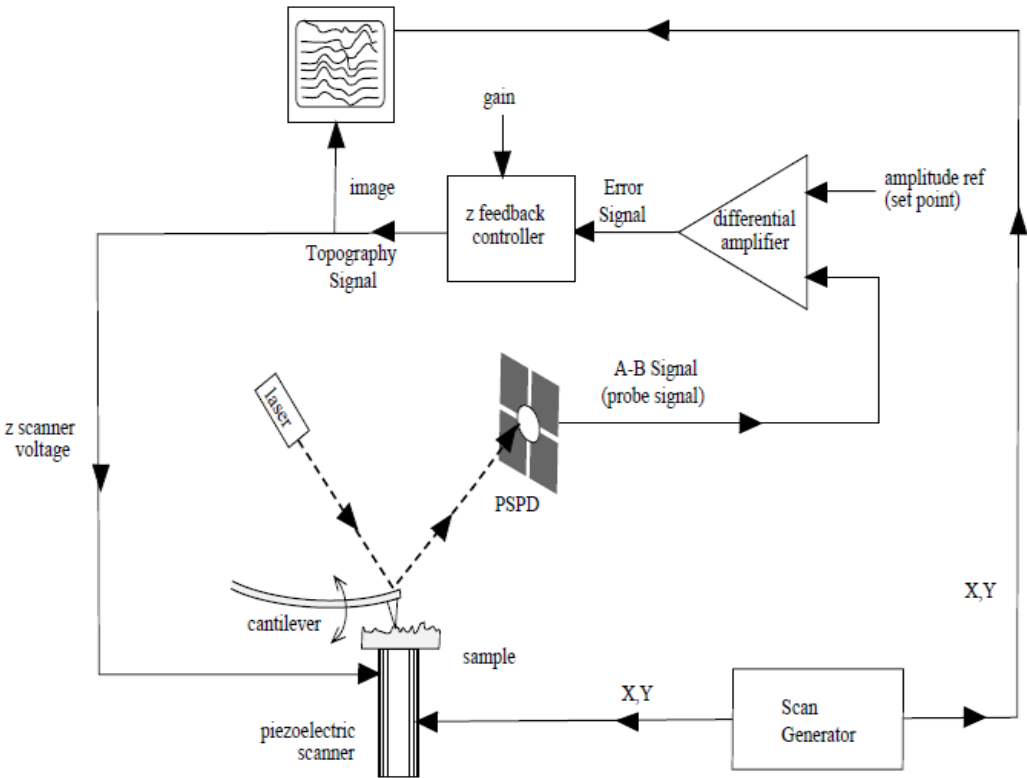


Figure 4.14 Simplified schematic operation of the Veeco CP II AFM system [151].

AFM cantilevers are designed in such a way that they can respond to forces from the surface. The most common force associated with typical sample-tip separations is the van der Waals force. The dependence of the van der Waals force on the sample-tip spacing is shown in figure 4.15. In the contact regime, the cantilever is held less than a few angstroms from the sample surface and the inter-atomic force between the cantilever and the sample is repulsive [152].

In the non-contact region, the cantilever is held on the order of tens to hundreds of angstroms from the sample surface, and the inter-atomic force between the cantilever and the sample is attractive (mainly as a result of the long-range van der Waals interactions). Both contact and non-contact imaging techniques can be used in surface analysis studies [152].

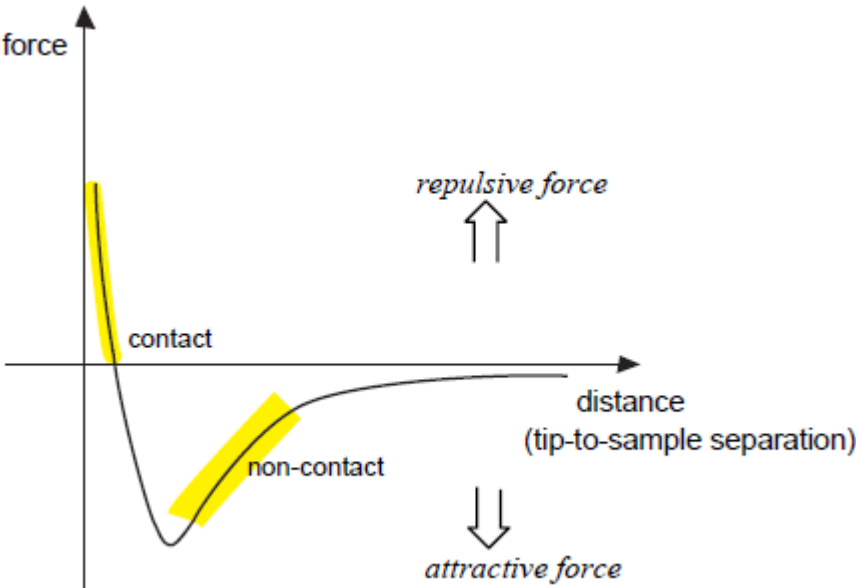


Figure 4.15 Interatomic force vs. distance curve showing the dependence of the van der Waals force on the sample-tip spacing [152].

Contact AFM

In contact-AFM mode or repulsive mode, the tip makes soft physical contact with the sample. The tip is connected to the cantilever with a very low spring constant. This spring constant is lower than the effective spring constant holding the atoms of the sample together. The scanner traces the tip gently over the surface of the sample or the sample under the tip. The contact force causes the cantilever to bend to accommodate the topography of the sample [152].

As the sample-tip distance decreases (see figure 4.15), the atoms in the sample and tip begin to weakly attract one another. This attraction increases with a decrease in separation distance until the atoms are so close together that their electron clouds repel each other electrostatically. The electrostatic repulsion will continue to weaken the attractive force as the separation distance decreases. The force goes to zero when the distance between the atoms reaches several angstroms. When the total van der Waals force becomes positive and hence repulsive the atoms are in contact [152].

In the contact region of the curve the van der Waals force is very steep and the repulsive force balances any other force that attempts to push the atoms closer together. Thus in the AFM when the cantilever (see figure 4.16) pushes the tip against the sample, the repulsive force ensures that the cantilever bends rather than forcing the tip atoms closer to the sample atoms. If a very stiff cantilever is used to exert large forces on the sample, the inter-atomic separation between the tip and the sample atoms is unlikely to decrease; instead the sample surface is likely to be deformed [152].

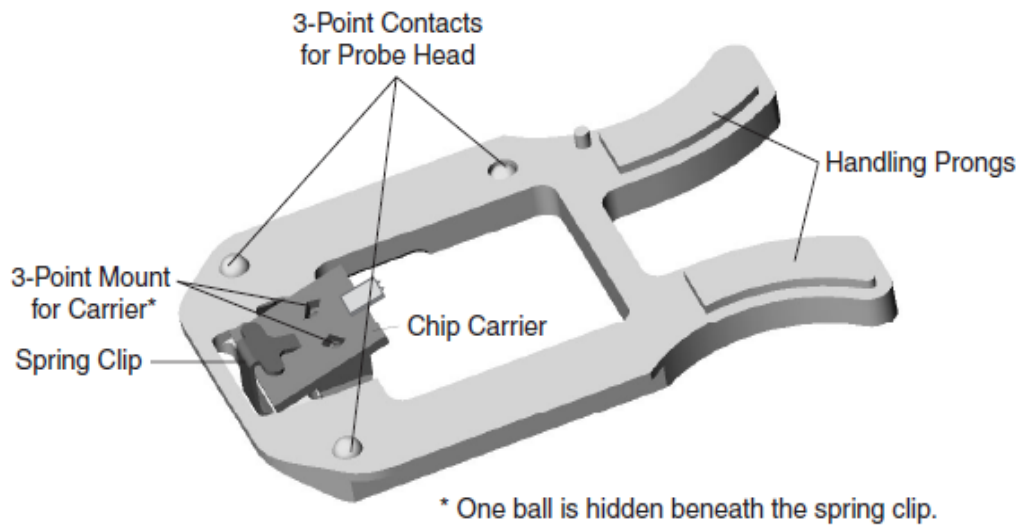


Figure 4.16 The Veeco CPIX AFM Probe cartridge [150].

The AFM can generate the topographic data set by operating in two different modes, constant height or constant-force mode. In constant height mode the spatial variation of the cantilever deflection can be used directly to generate the topographic data set because the height of the scanner is fixed as it scans. In constant force mode the deflection of the cantilever can be used as input to a feedback circuit that moves the scanner up and down in z , responding to the topography by keeping the cantilever deflection constant.

The image is generated from the scanner's motion, and the total force applied to the sample is constant. In constant force mode the speed of scanning is limited by the response time of the feedback circuit, but the total force exerted on the sample by the tip is well controlled.

Non Contact AFM (NC-AFM)

Non-contact AFM is one of several vibrating cantilever techniques in which a cantilever is vibrated near the surface of a sample. The spacing between the tip and the sample in non-contact use is of the order of tens to hundreds of angstroms. Non-contact AFM is desirable because it provides a means for measuring sample topography with very little or no contact between the tip and sample, thus soft (e.g. HOPG) and elastic samples can be studied [152].

A further advantage is that samples like silicon wafers are not contaminated by the tip. A disadvantage of non-contact AFM is that it is more difficult to measure the force since it is so low, also because the force is so low the cantilever has to be stiffer. Figure 4.17 shows the difference between two images taken with contact and with non-contact AFM.

The non-contact AFM picks up a water droplet on the surface of the sample and registers it as a part of the topography. The contact AFM however does not pick the drop up as being part of the topography since the tip moves easier through the drop as it traces across the surface of the sample. This is one of the disadvantages of non-contact operation [152].

If however the sample was very soft then the contact operation would drag the tip through different features of the topography and a distorted image of the surface would be obtained. It is thus important to consider the type of sample when choosing the mode of operation.

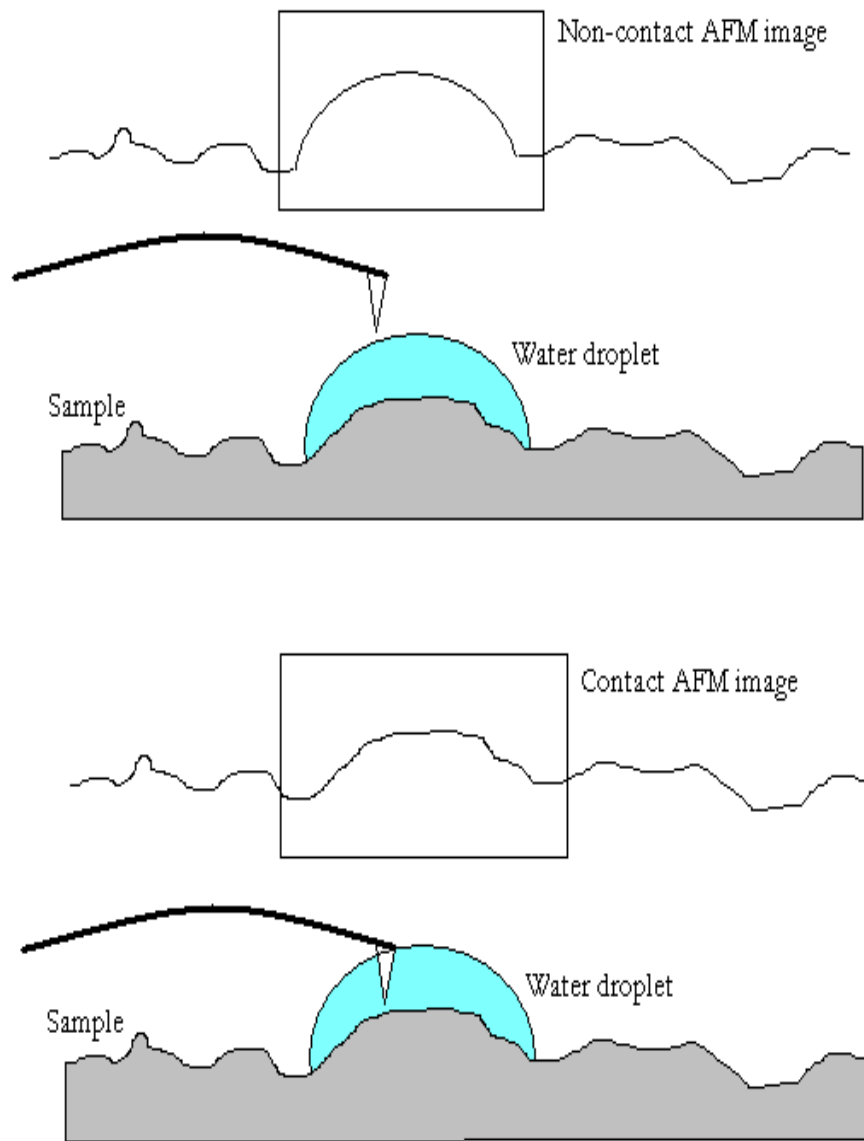


Figure 4.17 Contact and non-contact AFM images of a surface with a water droplet [152].

4.4.2 The Scanning and Tunnelling Microscope (STM)

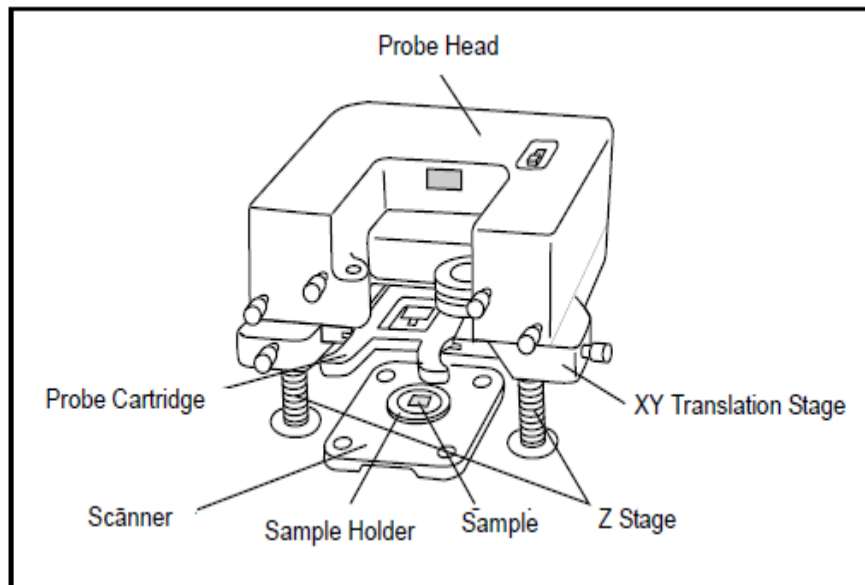


Figure 4.18 The Veeco CP II AFM/STM probe head [150].

The apparatus for STM experiments is generally similar to setups used in AFM experiments. The main difference is the origin of the primary signal being measured. In AFM studies, the van der Waals forces constitute a large fraction of the measured signal whereas, in the STM experiments, the tunnelling electrons make up most of the measured signal.

The STM was invented by G. Binnig, H. Rohrer and collaborators in the early 1980s [153]. The technique relies on tunnelling current between the probe and the sample to sense topography of the sample. The STM probe is an atomically sharp metal tip and is positioned a few atomic diameters above a conducting sample which is electrically biased relative to the tip [153].

At a distance less than 1nm, a tunnelling current flows from sample to tip. In operation, the bias voltages typically range from 10 to 1000 mV while the tunnelling currents vary from 0.2 to 10 nA. The tunnelling current changes exponentially with sample-tip separation. When the two surfaces (tip and sample) are sufficiently close that their wavefunctions overlap, the resulting current is given by

$$I = C \rho_t \rho_s e^{t \cdot \sqrt{k}} \quad (4.2)$$

where ρ_t and ρ_s are densities of the tip and sample respectively, C is a constant and $k = \frac{\sqrt{2m(V-E)}}{\hbar}$ [154].

The exponential relationship between tip separation and tunnelling current makes the tunnelling current an excellent parameter for sensing sample-tip separation (high vertical resolution). A reproduction of the sample surface is produced by scanning the

tip over the sample surface and sensing the tunnelling current. The first STM operated in ultrahigh vacuum on cryogenically cooled samples today; many variations of the STM exist.

STM is generally used under the following conditions [154]:

- For samples with deeply relieved features or where feature verticality is $\sim 90^\circ$.
- Polished samples where different layers having similar topography but different electrical conductivities are to be imaged
- Under conditions where contact with the sample surface is prohibited.

The STM head utilized in this work uses a piezoelectric tube approximately 1.3 cm in diameter to control the 3D motion of the tip. The electrode configuration produces X and Y motions which are perpendicular, minimizes horizontal and vertical coupling and provides good sensitivity. The feedback loop (see figure 4.14) drives the Z motion which controls vertical motion of the Piezo tube.

The Piezo tube, like all mechanical systems, has a resonance frequency which can cause the system to oscillate. The motion of the tip due to external vibrations is proportional to

$$\frac{(f_v)^2}{(f_o)^2} \tag{4.3}$$

where f_v is the vibrational frequency and f_o is the resonant frequency [153]. The Piezo tube has vertical and horizontal resonant frequencies, ~ 60 KHz and 40 KHz respectively for a standard STM head.

When a voltage, V , is applied to a sample (with the tip at ground), only states lying between E_f and $E_f + eV$ participate in tunnelling. The sign and magnitude of the applied voltage determines which states contribute to the resulting topographic images. Many STM experiments are conducted at bias voltages between 1 and 3 V. For interpretation of such high bias results, it is useful to consider the predictions of the simple ‘planar’ tunnelling model using the Wentzel-Kramers Brillouin (WKB) approximation. The WKB theory predicts that the tunnelling current is given by [154]:

$$I = \int_0^{eV} \rho_s(r, E) \rho_t(r, -eV + E) T(E, eV, r) dE \quad (4.4)$$

where $\rho_s(r, E)$ and $\rho_t(r, E)$ are the density of states of the sample and tip respectively at location r and the energy E , is measured with respect to their individual Fermi levels. From equation 4.4, we see that for a negative sample bias, $eV < 0$ and for a positive sample bias, $eV > 0$.

The tunnelling transmission probability $T(E, eV, r)$ for electrons with energy E and applied bias voltage V is given by:

$$T(E, eV) = \exp\left(-\frac{2z\sqrt{2m}}{\hbar} \sqrt{\frac{\phi_s + \phi_t}{2} + \frac{eV}{2} - E}\right) \quad (4.5)$$

where z is the sample-tip spacing and ϕ are the work functions [154]. Therefore, tunnelling is always largest for electrons at the Fermi level for which ever electrode is negatively biased.

Scanning and Tunnelling Spectroscopy (STS)

The AFM/STM apparatus shown in figure 4.18 allows one to conduct tunnelling spectroscopy measurements. The uniqueness of STS when applied to amorphous diamond-like carbon and related materials is related to the fact that STS makes it possible to study the local electronic structure of such materials in regions smaller than the characteristic size of the sp^2 and sp^3 hybridized clusters [155].

Depending on the conditions of measurements, the tunnelling current may be proportional to either the density of electron states at the sample surface or the corresponding convolution with the density of states (DOS) in the STM tip [155]. At lower bias voltages (when the applied voltage is lower than the sample & tip work function), structure in dI/dV vs V_{Bias} is associated with the surface (DOS) [154].

Structure in the surface DOS can arise from critical points in the surface-projected bulk band structure or from true surface states which are generally associated with surface reconstructions. In practice, the tip DOS and the voltage-dependent tunneling probability are almost always unknown hence, extracting quantitative information is often challenging.

In the study of metals and semiconductors, the energy range usually extends several eV on either side of the Fermi energy E_F . Since $T(eV, V)$ is generally a slowly varying function, valuable semi-quantitative electronic structure information can be obtained from I-V measurements [154].

Feenstra *et al.* [156] argued that normalization of dI/dV by (I/V) reduces the data to a form like

$$\left(\frac{dI}{dV}\right) / \left(\frac{I}{V}\right) = \frac{d(\log I)}{d(\log V)} = \frac{\rho_s(eV)\rho_t(0) + A(V)}{B(V)} \quad (4.6)$$

The background term $A(V)$ contains the influence of the electric field in the energy gap whereas, $B(V)$ normalizes the transmission probability over the DOS. Assuming that $A(V)$ and $B(V)$ vary slowly with voltage, structure in $(dI/dV)/(I/V)$ reflects the surface density of states, $\rho_s(eV)$. One major advantage of this normalization procedure, is that it tends to reduce the distance dependence of the tunneling probability [156].

Estimation of the electronic energy band is possible from differential current curves; dI/dV vs. V_{Bias} in STS measurements. Ivanov-Omskiĭ *et al.* [155] estimated the electronic energy band gap for amorphous carbon (*a-C*) films using STS measurements (see figure 4.19).

Nevertheless, there are some drawbacks inherent with the STS method. One of these drawbacks is that, with the feedback loop open, the STM tip is found in the state of unstable equilibrium [157]. Transient processes in the STM circuits at the instant the feedback loop is opened, electrostatic interaction between the tip and the substrate and other interferences may result in uncontrolled changes in the distance between the tip and the sample [155]. However, advances in software allow one to make corrections in the data hence minimizing the possibility of incurring artifacts [158].

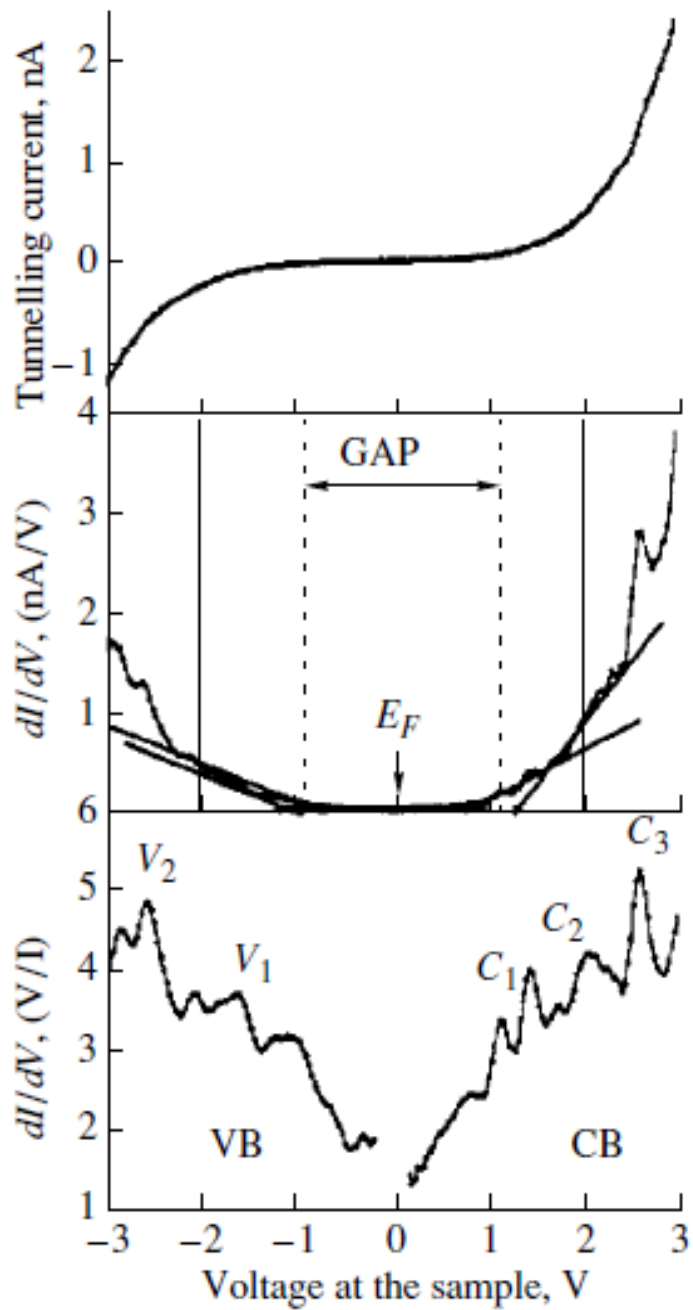


Figure 4.19 Current-voltage characteristics of *a*-C, (top): conventional I-V curve, (middle): differential I-V curve and (bottom): normalized differential current curve [155]. CB and VB refer to the conduction and valence bands respectively.

4.5 Raman Spectroscopy

Raman scattering refers to the inelastic scattering of phonons by fundamental excitations in molecules or solids. Raman spectroscopy is a standard non-destructive technique for the characterization of carbon-based materials. The Raman spectra of vibrational excitations in the various forms of carbon exhibit large differences [159,160,161,162]. The mechanical and optical properties depend on the sp^3 content as well as on the number and size of clusters with short-range and medium range ordered sp^2 -coordinated carbon atoms [163].

Raman scattering on DLC coatings is a sensitive probe of sp^2 and sp^3 bonding of the carbon atoms and of the nanocrystalline clusters. Due to the lattice disorder, the wave vector selection rules are relaxed and phonons from the whole Brillouin zone contribute to the Raman spectra. The observed broad bands reflect the phonon density of states. In the case of exciting the spectra with visible light, resonance effects are essential for the selection of the phonons which contribute to the Raman scattering process [163].

By excitation with phonons of visible light, the Raman spectrum is dominated by scattering of sp^2 bonded graphitic carbon due to resonance enhancement of the Raman scattering cross section. Two broad bands appear at about 1550 cm^{-1} (“G-peak”) and at about 1360 cm^{-1} (“D-peak”). Although the visible Raman spectrum depends fundamentally on the ordering of the sp^2 bonded carbon and only indirectly on the sp^3 content, it can be used in a restricted range of conditions to derive information about the sp^2/sp^3 ratio [163].

In the Raman effect, a photon is scattered inelastically by a crystal, with creation or annihilation of a photon or magnon (see figure 4.20). The process is identical to the inelastic scattering of x-rays. The selection rules for the first-order Raman Effect are:

$$\omega = \omega' \pm \Omega; \quad \mathbf{k} = \mathbf{k}' \pm \mathbf{K}, \quad (4.7)$$

where ω , \mathbf{k} refer to the incident photon; ω' , \mathbf{k}' refer to the scattered photon and Ω , \mathbf{K} refer to the photon created or destroyed in the scattering event. In the second-order Raman Effect, two photons are involved in the inelastic scattering of the photon. The Raman Effect is made possible by the strain-dependence of the electronic polarisability [164].

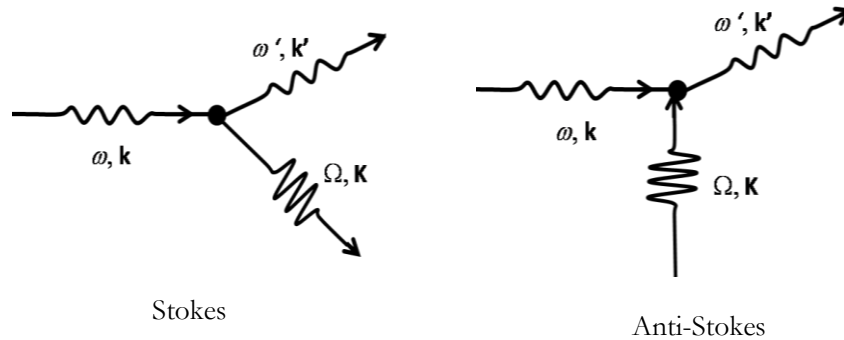


Figure 4.20 Raman scattering of a photon with emission or absorption of a phonon. The process is called Brillouin scattering when an acoustic phonon is involved and polariton scattering when an optical phonon is involved. Similar processes occur with magnons [164].

The polarization of the dipoles excited in solids when a laser beam (amplitude; E_0 frequency ν_{las}) interacts with phonons of frequency ν_{vib} depends on the polarisability tensor $\bar{\alpha}$:

$$\vec{P} = \bar{\alpha} \times \vec{E}_0 \cos(2\pi\nu_{las}t) \quad (4.8)$$

where $\bar{\alpha}$ terms can be individually described as functions of the normal vibrational coordinates Q using a Taylor approximation [165]:

$$\alpha_{ij} = \alpha_{ij}^0 + \left(\frac{\partial \alpha_{ij}}{\partial Q} \right)_{Q=Q_0} \times Q \quad (i, j = x, y \text{ or } z) \quad (4.9)$$

$$P_i = \sum_j \alpha_{ij} \times E_j \quad (4.10)$$

$$= \sum_j \left[\alpha_{ij}^0 E_{0j} \cos(2\pi\nu_{las}t) + \frac{E_{0j} Q_0}{2} \left(\frac{\partial \alpha_{ij}}{\partial Q} \right)_{Q=Q_0} \times [\cos(2\pi(\nu_{las} - \nu_{vib})t) + \cos(2\pi(\nu_{las} + \nu_{vib})t) + \dots] \right]$$

With the scattered electric field being proportional to \vec{P} , equation 4.10 predicts both quasi-elastic ($\nu \sim \nu_{vib}$) and inelastic ($\nu = \nu_{las} \pm \nu_{vib}$) light scattering. The former is known as Rayleigh scattering and the latter, which occurs only if vibrations change polarisability ($\partial \alpha_{ij} / \partial Q \neq 0$) is known as Raman scattering [165].

The classical theory of radiation from an oscillating dipole demonstrates that the Raman peaks have a Lorentzian shape [165]:

$$I(\vec{\nu}) = I_0 \times \int \frac{d^3\vec{k}}{[\vec{\nu} - \vec{\nu}(\vec{k})]^2 + \frac{\Gamma_0^2}{2}} \quad (4.11)$$

where $\vec{\nu}(\vec{k})$ represents the dispersion branch to which the mode belongs to and Γ_0 represents the half-width for the ordered reference structure and the integral is taken over the Brillouin zone. The scattering of one phonon ($\vec{k} \sim \vec{0}$) by n phonons (wave vectors, \vec{k}_i) is governed by the momentum conservation rule [165]:

$$\sum_{i=1}^n \vec{k}_i = \vec{k}_{scattered} - \vec{k}_{incident} \approx \vec{0} \quad (4.12)$$

The Raman spectroscopy setup that has been used to characterise our HOPG sample at the University of the Witwatersrand is shown below in figures 4.21 and 4.22.



Figure 4.21 Raman spectroscopy/PL setup at the University of the Witwatersrand.

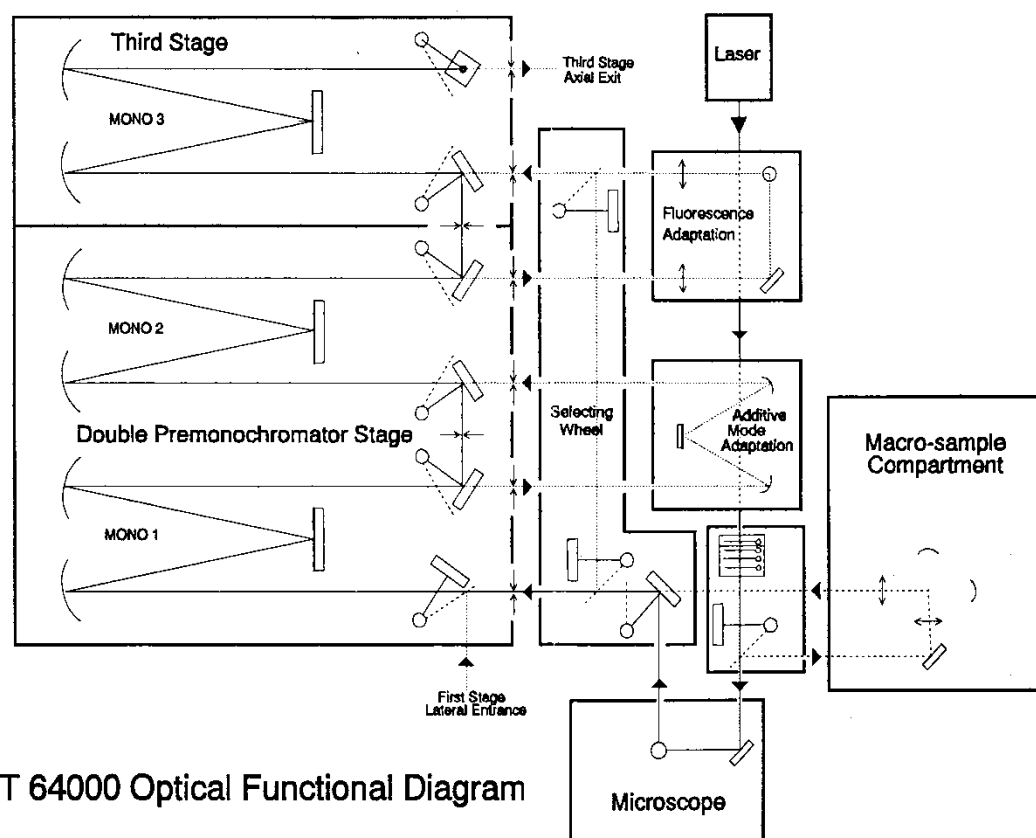


Figure 4.22 Diagram showing the light path for the Raman setup shown in figure 4.21.

Raman spectra acquired in this work are acquired using a Jobin-Yvon T64000 Raman spectrometer operated in single spectrograph mode, with either a 600 lines/mm grating (longer range, lower spatial resolution) or a 1800 lines/mm grating (higher spatial resolution, smaller range), depending on the spectral range of interest. Backscattered light was collected via an Olympus BX40 microscope attachment, using either an Ultra long working distance 50X objective or a 100X objective. The backscattered light was dispersed via the mentioned gratings onto a liquid nitrogen cooled CCD detector and

data collected via Labspec.4.18 software. Two dimensional mapping was done via a motorised X-Y Marzhauser stage controlled via the Labspec software. The 514 nm line of an argon laser was used as the excitation source in all cases. It is important to note the following details:

- Excitation wavelength: $\lambda = 514 \text{ nm}$; Beam spot diameter: $\approx 1 \mu\text{m}$.
- Numerical Aperture, $\text{NA} \approx 0.5$.
- Lateral resolution: $R = 0.61 \times \lambda/\text{NA} = 0.63 \mu\text{m}$. The best possible resolution is $R = 0.314 \mu\text{m}$ (The Abbe' criterion states that the wave nature of light prevents the distinction of points closer than $\lambda/2$, [166]).

With these conditions it should be unlikely to detect structures less than 100 nm in diameter in our Raman setup. Figure 4.23 shows the spatial points that were investigated using Raman spectroscopy. Raman maps were conducted on the sites indicated below.

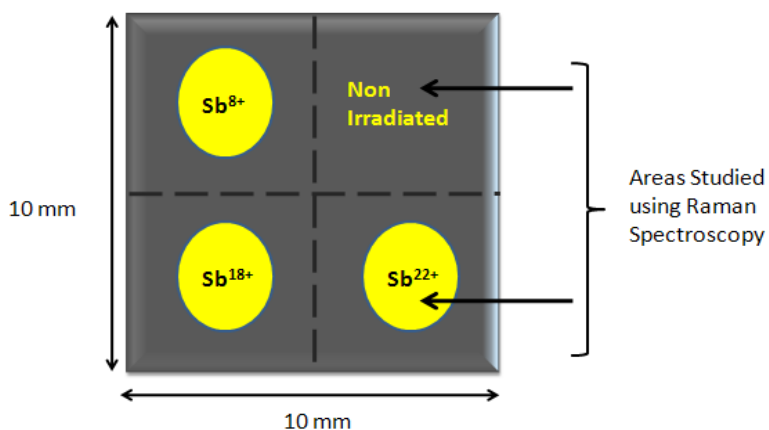


Figure 4.23 Diagram showing the areas on the HOPG sample that were studied using Raman spectroscopy.

4.6 Photoluminescence (PL)

PL refers to the spontaneous emission of light (visible electromagnetic radiation) from a material following optical excitation. The excitation energy and intensity are chosen to probe different regions and excitation concentrations in the sample. Although PL techniques are commonly used to characterize different material parameters, the technique provides electrical rather than mechanical characterization [167].

The first truly scientific investigation of photoluminescence was carried out by Sir George Gabriel Stokes in 1852 (“On the Change of Refrangibility of Light”) [168]. PL is a luminescence caused by ultraviolet, visible or infrared radiation. A special form of PL is the anti-Stokes luminescence where an emission at wavelengths shorter than the shortest wavelength of the excited radiation occurs [169].

In particular, luminescence stimulated by non-ionizing optical radiation is called photoluminescence and includes fluorescence as well as phosphorescence depending on whether the radiative transition is a spin-allowed transition between two states with equal multiplicity (singlet-singlet and sometimes, triplet-triplet) or a spin forbidden transition between two states with different multiplicities (triplet-singlet) [169].

Features observed in the characteristic spectrum can be used to identify surface, interface impurity levels and to gauge disorder and interface roughness. PL is a contactless, non destructive characterization technique and has proven to be an important tool in surface characterization however; the fundamental limitation of PL analysis is its dependence on radiative events [167].

Figure 4.24 shows the principal pathways by which transitions occur (Birks, 1970) [170]. In most cases, molecules are raised from the ground state (S_0) to an excited state (S_n) by absorption. The favoured path for de-excitation is one which minimizes the lifetime of the excited state. Almost all molecules drop quickly to the lowest levels (S_1 or T_1) by non-radiative processes, so that the most commonly observed radiative transitions are $S_1 \rightarrow S_0$ fluorescence and $T_1 \rightarrow S_0$ phosphorescence [169].

In general, fluorescence lifetimes (0.1-10 ns) are much shorter than phosphorescence lifetimes (1 ms to 10 s). Fluorescence has thus also been defined as photoluminescence which occurs promptly after excitation while phosphorescence is discernibly delayed [169].

PL measurements were conducted on the unirradiated and the Sb^{22+} impact sites on HOPG. The apparatus is very similar that to used for the Raman spectroscopy measurements. However, two different objective lenses were used, namely the 50X and 100X objectives. The main reason for using the 2 objective lenses is that the 100X objective has higher light collection efficiency. Therefore, small peaks might appear stronger than usual whereas, the 50X has a higher resolution and can thus resolve a large range of PL peaks.

The setup utilizes a 514 nm excitation laser as in the Raman setup; however, diamond was a relatively large band gap and usually requires ultraviolet excitation.

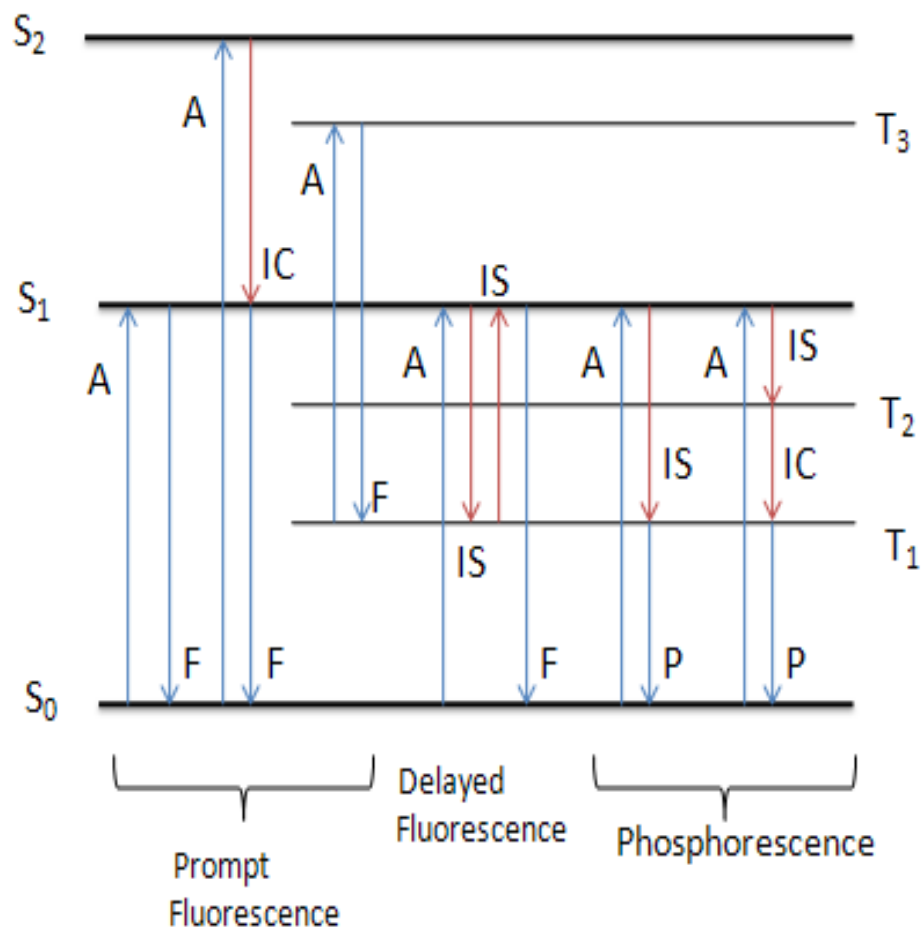


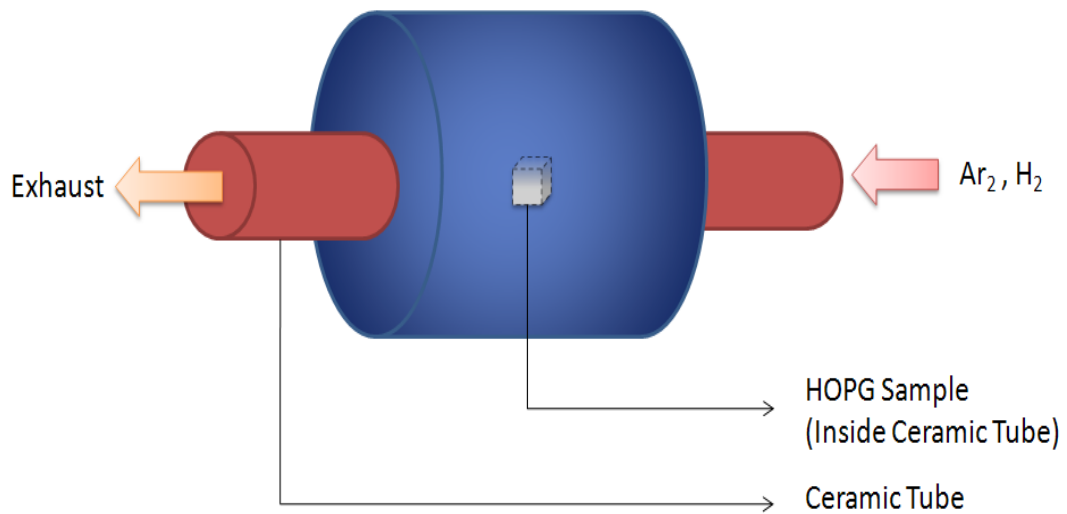
Figure 4.24 Schematic energy level diagram showing the pathways by which PL transitions occur. Principal radiative (\rightarrow) and nonradiative (\rightarrow) transitions causing photoluminescence. $S_0, S_1 \dots$ singlet levels; T_1, T_2, \dots triplet levels. A represents absorption (10^{-18} - 10^{-15} s). IC: internal conversion ($\sim 10^{-12}$ s). IS: internal crossing ($\sim 10^{-9}$ s) F: fluorescence (10^{-9} - 10^{-8} s). P: phosphorescence (10^{-3} - 10 s) [169].

4.7 Annealing Apparatus

Meguro *et al.* injected electrons from an STM tip (alternatively localised He-Cd laser irradiation can be used) onto SHCI induced surface defects to catalyse the conversion of sp^2 to sp^3 bonding in graphite [16]. In this work, the catalysis of sp^2 to sp^3 bonds is achieved by annealing the sample at $\sim 650^\circ\text{C}$ in a hydrogen atmosphere for 40 minutes. This transformation is possible because hydrogen radicals etch away any graphite reconstructions on the surface facilitating only diamond growth [90].

The annealing stage of this project has been carried out at the University of the Witwatersrand. The setup utilised is fairly simple and is shown in figure 4.25 below. In conventional annealing systems, impurities are sometimes present from previous annealing experiments. To reduce the probability of introducing impurities into the induced defects, we first raised the temperature of the system to $\sim 800^\circ\text{C}$ then flushed the ceramic tube with Argon gas for 10 minutes.

After 10 minutes we then lowered the temperature to $\sim 650^\circ\text{C}$, inserted the sample into the ceramic tube, flushed Argon for about 10 minutes and then introduced Hydrogen gas into the ceramic tube. One of the important safety precautions to take into account is to make sure that hydrogen gas is released from the ceramic tube in a reasonably short time. This is because hydrogen explodes when compressed under high temperatures. The release of hydrogen (and argon) is achieved by creating an exhaust at the end of the ceramic tube (see figure 4.25).



Annealing Temperature: 650°C

Annealing Time: 40 minutes

Figure 4.25 Simplified diagram showing the annealing setup at the University of the Witwatersrand. Note: The ceramic tube is connected to a thermocouple to enable temperature control of the system.

Chapter 5

5. Results and Discussion

5.1 Overview

In this section, findings from experimental investigations will be presented and analysed. These include AFM (before and after annealing), Raman Spectroscopy, Photoluminescence (PL), STM imaging and STS analysis. Ion implantation experiments using Sb with varying charge states were conducted at the Electron Beam Ion Trap (EBIT) facility at Lawrence Berkeley National Laboratory in U.S.A, while Raman spectroscopy, PL, AFM, STM and STS experiments were conducted at the University of the Witwatersrand in South Africa.

5.2 AFM Analysis (before annealing)

The HOPG surface can undergo mechanical deformation with minimal applied stress. This is a direct consequence of its bonding nature described in chapter 3. For this reason and to preserve the impact induced defects, non-contact AFM was used to analyze the

nature of the defects before annealing. It is also important to note that all AFM analysis was conducted at room temperature and ambient pressure.

In order to assess the nanostructuring of the HOPG surface and to characterize the sample before surface treatment, the SHCI implanted regions were analyzed using the AFM apparatus described in section 4.4.1. Results from NC-AFM analysis are shown below.

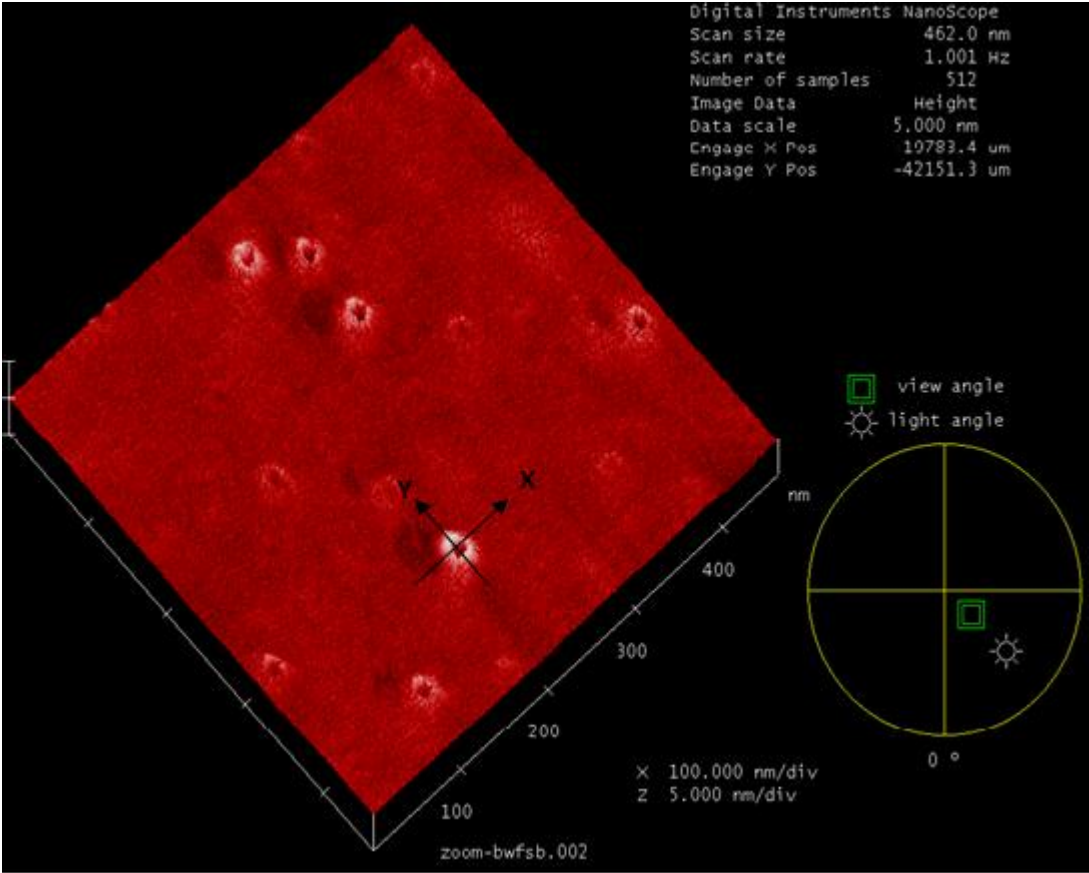


Figure 5.1 Example of NC-AFM image taken over the Sb^{22+} impact site on HOPG showing line profile directions x and y.

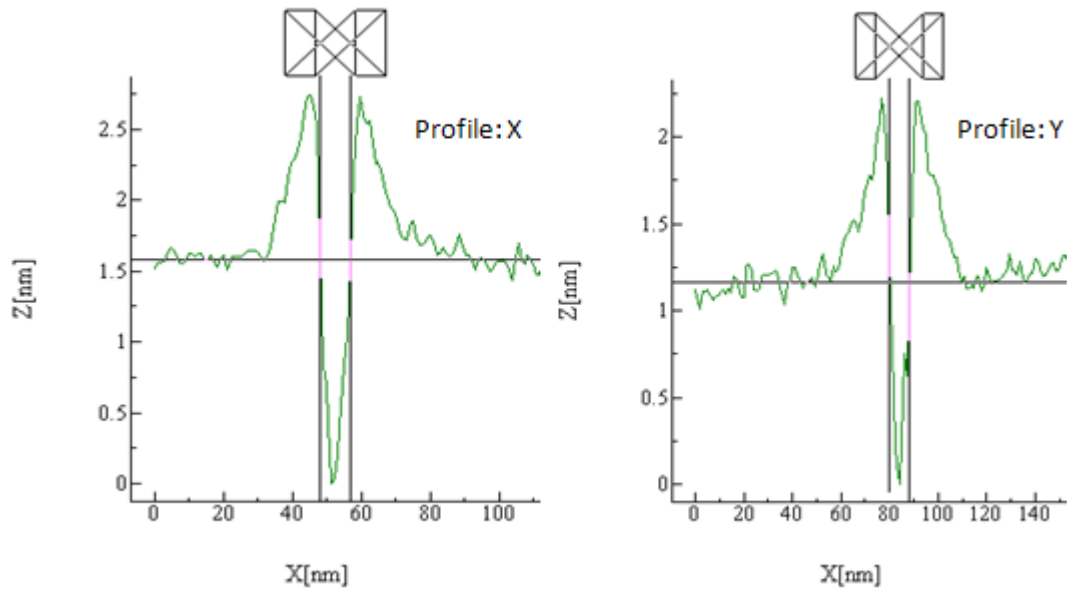


Figure 5.2 Line profiles across Sb^{22+} induced nanod defect on HOPG along directions x and y shown in figure 5.1.

Figure 5.1 and 5.3 shows examples of NC-AFM images of SHCI impact induced nanod defects on HOPG before annealing. The AFM images were analyzed with respect to number densities, height and width distributions of the nanod defects. A summary of results acquired using NC-AFM on the nanod defects before annealing is shown in table 5.1. It is important to note that due to the finite radius of curvature of the AFM tip, there exists a systematic error in the diameters measured but not in the measured hillock heights [79].

In figure 5.1, the imaged region was irradiated with Sb^{22+} according to figure 4.23. There are ~ 10 visible defects in the imaged region. The given scan size is 462 X 462 nm,

therefore we expect to find ~ 21 impact induced defects assuming that the efficiency of defect formation is 100% and the beam distribution is Gaussian.

The actual ion distribution in the beam is Gaussian; however, the efficiency of defect formation is not 100%. Also, there is great difficulty in determining the ion fluence in such cases of extremely low current. Therefore given all these uncertainties, the observed number of defects is within reasonable expectations.

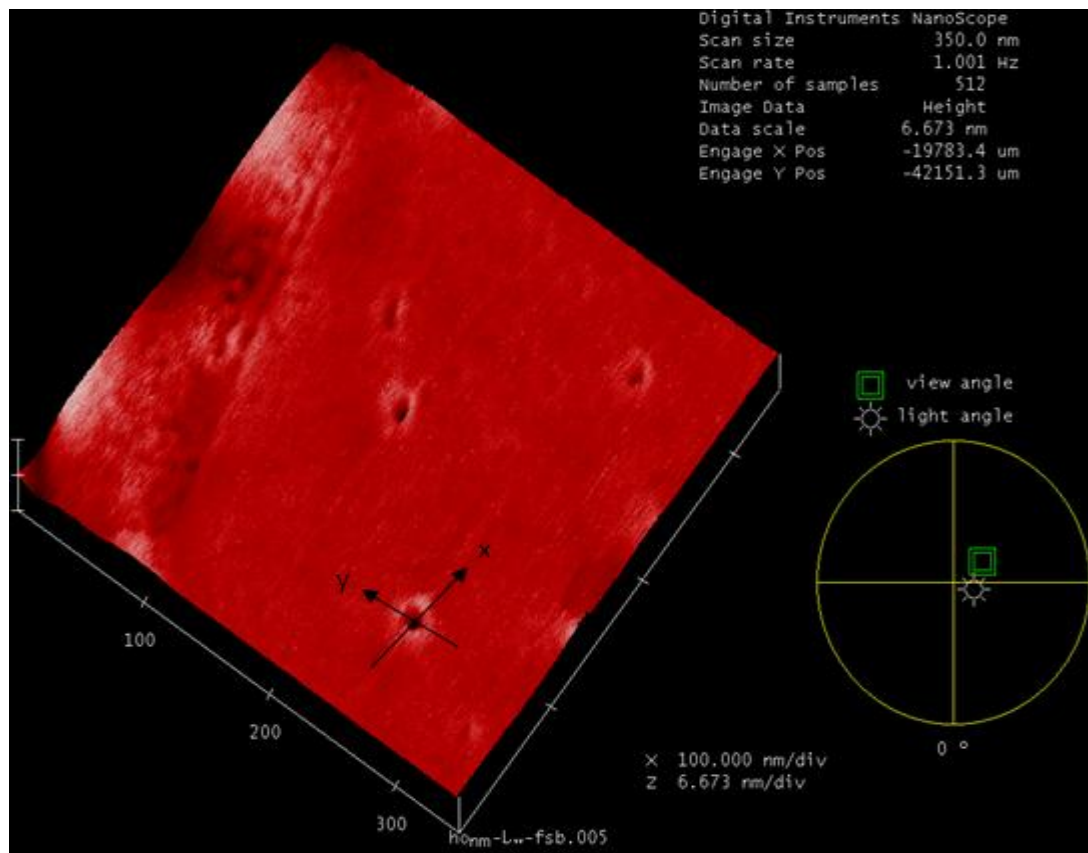


Figure 5.3 NC-AFM image taken over the Sb^{18+} impact site on HOPG showing line profile directions x and y.

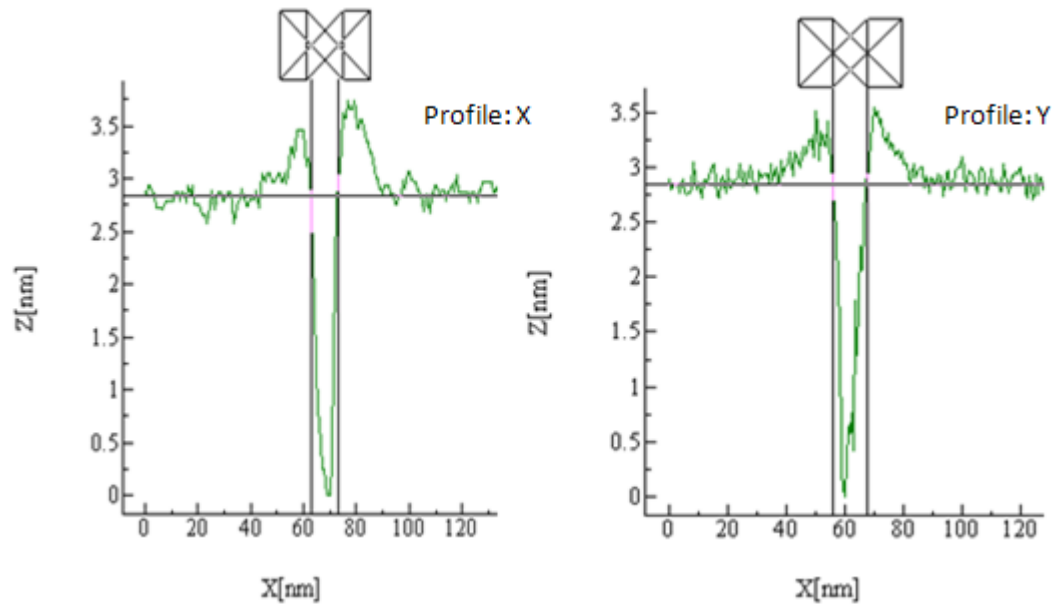


Figure 5.4 Line profile taken across a chosen Sb^{18+} induced nanodefect on HOPG along directions shown in figure 5.3.

All the observed SHCI induced nanodefects appear to have a crater at the center of a protrusion or hillock-like feature. Figures 5.1 and 5.3 show examples of such defects whereas, figures 5.2 and 5.4 show line profiles taken across the induced nanodefects along directions x and y defined in figures 5.1 and 5.3 respectively. The diameter and the height of the hillock-like features are quantified using statistical averages and the results are shown in table 5.1 and figures 5.5 and 5.6.

In figure 5.3, the Sb^{18+} induced nanodefects are presented. The scan size of the imaged region is 350 X 350 nm. Therefore, assuming an implantation dose of ~ 100 ions/ μm^2 where the ions in the beam follow a Gaussian distribution and the nanodefect formation efficiency is 100%, we expect to find ~ 12 impact induced defects. However, this not the

case because the efficiency of nanod defect formation is not 100% even though the ion distribution in the beam is Gaussian. Figure 5.4 shows line profiles taken across Sb^{18+} induced nanod defects along the directions x and y as shown in figure 5.3. Both the x and y line profiles have similar features to the Sb^{22+} induced nanod defects that is both have a crater in the middle of hillock-like feature, however, the diameter and hillock size appear to be slightly smaller than in the Sb^{22+} case.

Table 5.1 and figures 5.5 and 5.6 show summarized NC-AFM results of observed nanod defects before annealing. The average diameter (and height) of Bi^{35+} impact induced nanod defects has been included in the data for comparison. The errors shown are calculated by means of a standard deviation σ and a standard error in the mean, *StErr* (since the data is normally distributed) given by:

$$\sigma = \sqrt{\frac{1}{N} \sum_{i=1}^N (x_i - \bar{x})^2} \quad (5.1)$$

$$\text{StErr} = \frac{\sigma}{\sqrt{N}} \quad (5.2)$$

where N is the number of elements in the given sample space.

Table 5.1 shows a direct proportionality between the hillock height and the nanod defect diameter with respect to the charge state (hence kinetic energy and potential energy) of the incident ion. The direct proportionality of the nanod defect diameter with respect to charge state has been previously observed by several authors [182, 79, 35]. Figure 5.5 and 5.6 illustrate results shown table 5.1.

Table 5.1 Summary of results from observed nanodefects before annealing.

Property	Units	Sb ⁸⁺	Sb ¹⁸⁺	Sb ²²⁺	Bi ³⁵⁺
Defect diameter	nm	7.94±0.950	10.48±0.613	11.90±0.890	14.7±0.590
Hillock height	Å	1.90±0.382	7.72±0.418	8.60±0.392	9.72±0.916
Kinetic energy	keV	40	90	110	175

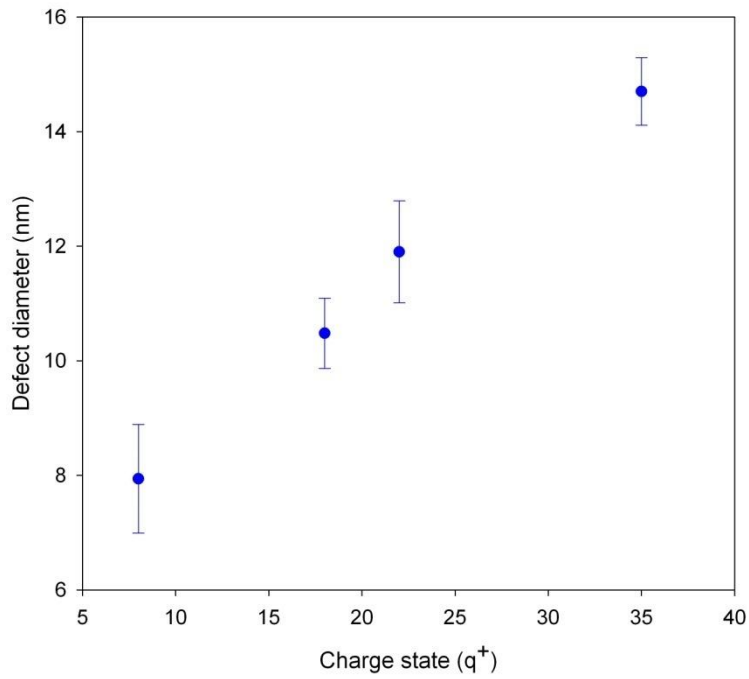


Figure 5.5 Charge state versus defect diameter of induced nanodefects before annealing.

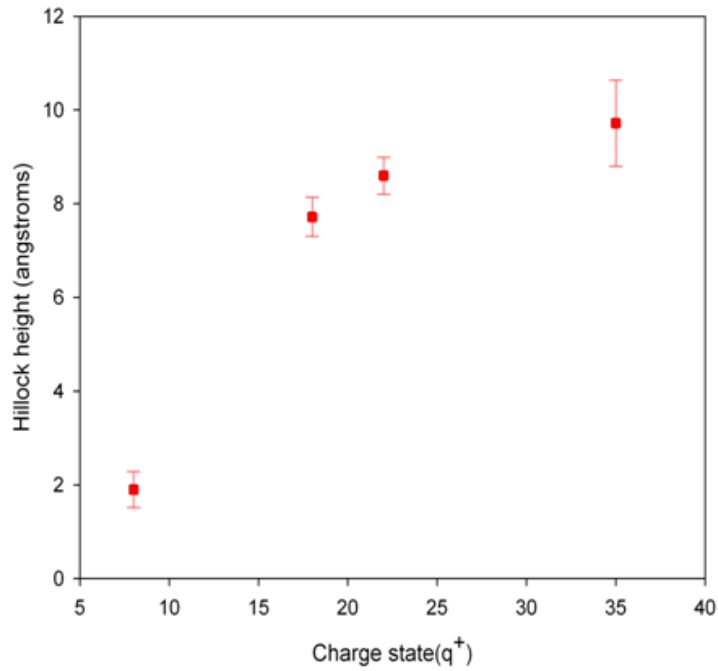


Figure 5.6 Charge state versus hillock height of induced nanodefects before annealing.

The above findings show that for all investigated charged states in this work, SHCI induced nanoscale defects have been formed. The nanodefects (before annealing) have diameters which vary between 7-15 nm while the hillock heights vary between 1 and 10 Å. Therefore, the diameter to height ratio varies between 15 and 70. The formation of nanodefects by SHCI irradiation is found to be directly proportional to the charge state of the incident SHCIs.

El-Said *et al.* found that for every target material, there exists a minimum potential energy (hence charge state) that any incident ion must have in order to form surface nanodefects [79]. However, as seen in figures 5.5 and 5.6, the potential energy threshold for SHCI induced nanod defect formation in HOPG occurs at lower incident charge states

than those utilized in this work. The interaction of the incident SHCI with the target surface, involves a series of complex processes which occur on different time and energy scales (see chapter 2). When a SHCI approaches the surface, neutralization starts by electron transfer from the target into highly excited states of the projectile. Deexcitation of the projectile proceeds via Auger-type processes producing primarily low energy electrons [79].

An increasing amount of potential energy (e.g. for highly charged heavy ions) is dissipated by X-ray emission. The critical distance R_c from the surface for electron transfer to the SHCI can be estimated as:

$$R_c \approx \frac{\sqrt{2q\varepsilon(8i + \varepsilon - 1)}}{(\varepsilon + 1)W} \quad (5.3)$$

where i is the amount of charge left behind (for the first electron capture $i=1$), W and ε are the work function and the dielectric constant of the material, respectively [79]. Therefore, for Sb^{8+} and Sb^{22+} impinging on HOPG, the critical distance for electron transfer is approximately 1.2 nm and 2.0 nm respectively.

The upper limit for the interaction time between the Sb SHCIs and the HOPG surface is therefore set by the critical distances 1.2 nm and 2.0 nm corresponding to Sb^{8+} and Sb^{22+} respectively. The interaction time for charge states studied in this work is \sim fs. Within this time scale multiple electron emission together with other surface processes described in chapter 2 of this work ultimately result in a localized deformation of surface and near surface regions which can be imaged using techniques such as AFM as in figures 5.1 and 5.3.

5.3 AFM Analysis (After annealing)

After annealing the HOPG sample at $\sim 650^\circ$ in a hydrogen atmosphere for ~ 40 minutes, NC-AFM images of the surface were acquired at room temperature and ambient pressure using the apparatus described in section 4.4. Results from the NC-AFM analysis after annealing are shown below. Only Sb^{18+} induced nanodefects are shown below for brevity, however, statistical results from all impact sites are shown in table 5.2 and plotted in figure 5.9 and 5.10.

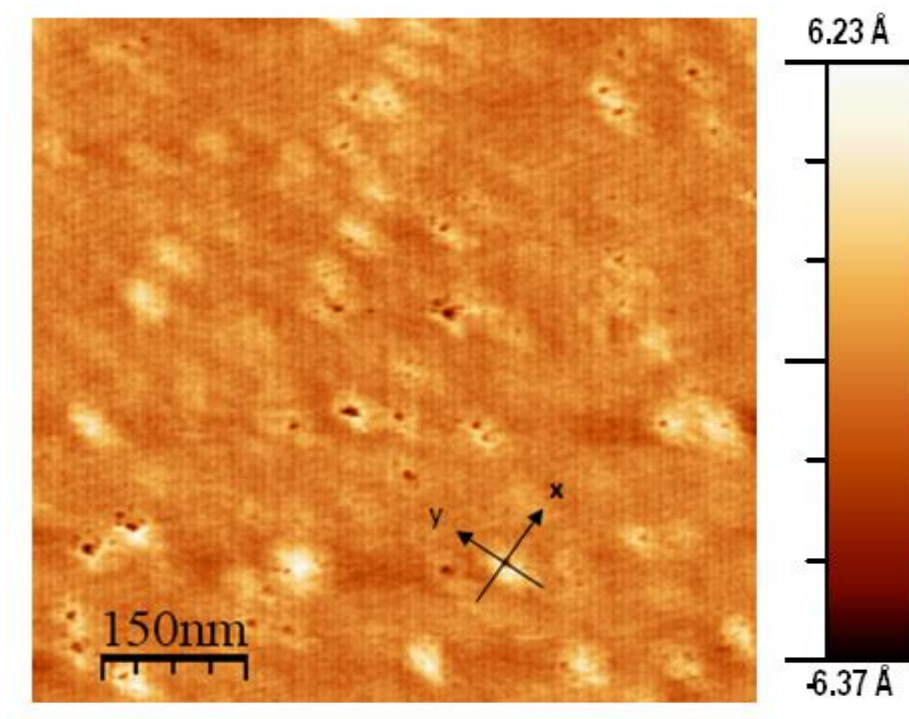


Figure 5.7 NCAFM topography image of a Sb^{18+} impact site on HOPG after annealing.

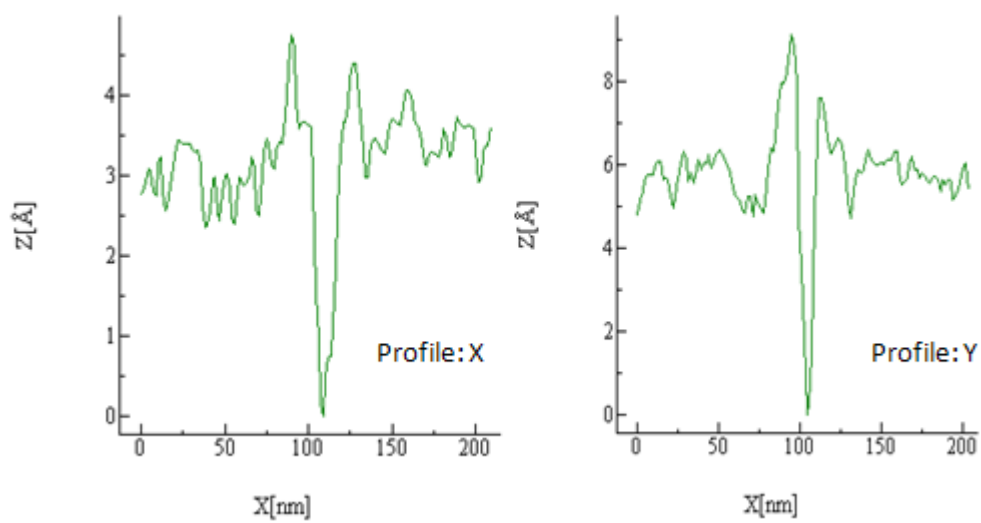
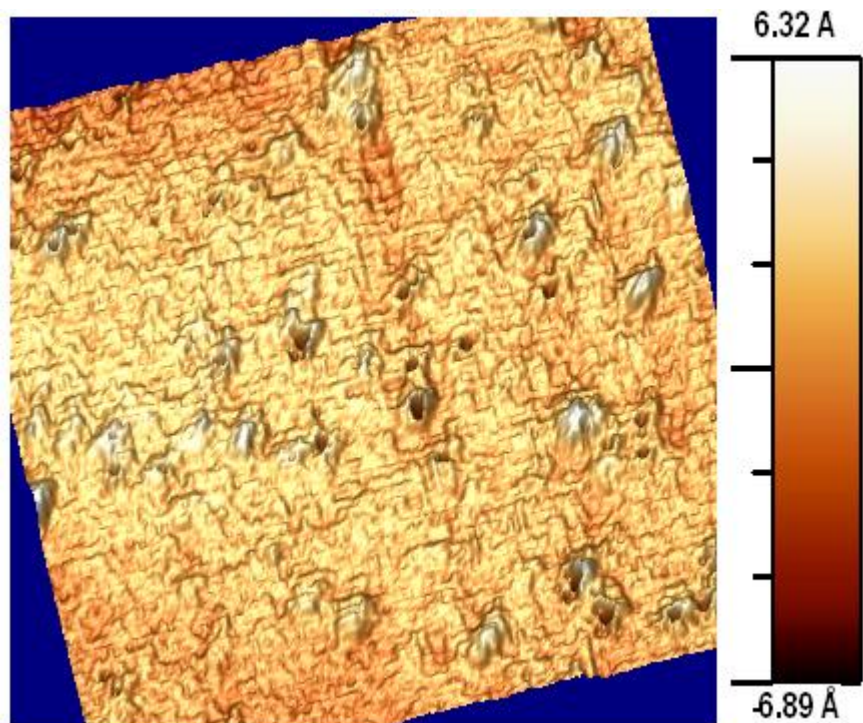


Figure 5.8 3D image of figure 5.7 (top) and line profiles showing the topography of Sb^{18+} induced nanodefects (bottom) after annealing. Note the x-y scale is identical to that in figure 5.7.

Table 5.2 Summary of results from observed nanodefects after annealing.

Property	Units	Sb ⁸⁺	Sb ¹⁸⁺	Sb ²²⁺
Defect diameter	nm	6.372±0.312	8.66±0.290	9.15±0.498
Hillock height	Å	1.821±0.121	2.01±0.143	2.473±0.182
Kinetic energy	keV	40	90	110

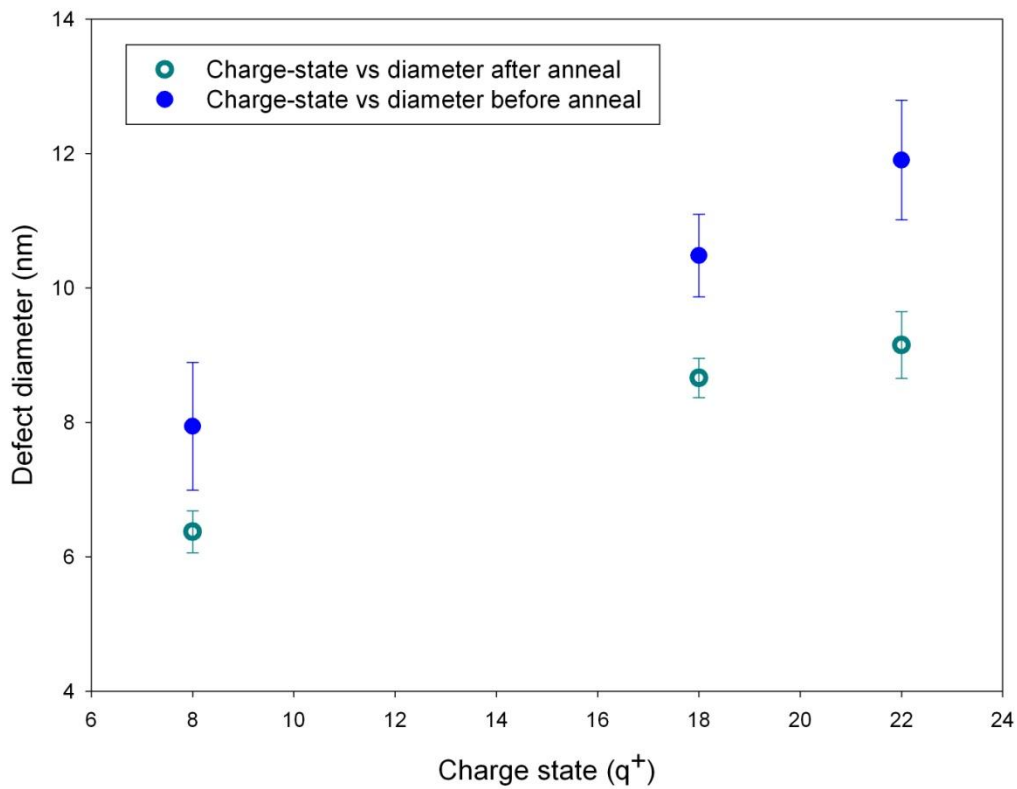


Figure 5.9 Comparison of the (average) defect diameters induced on HOPG before and after annealing as a function of the charge state of the incident Sb ions.

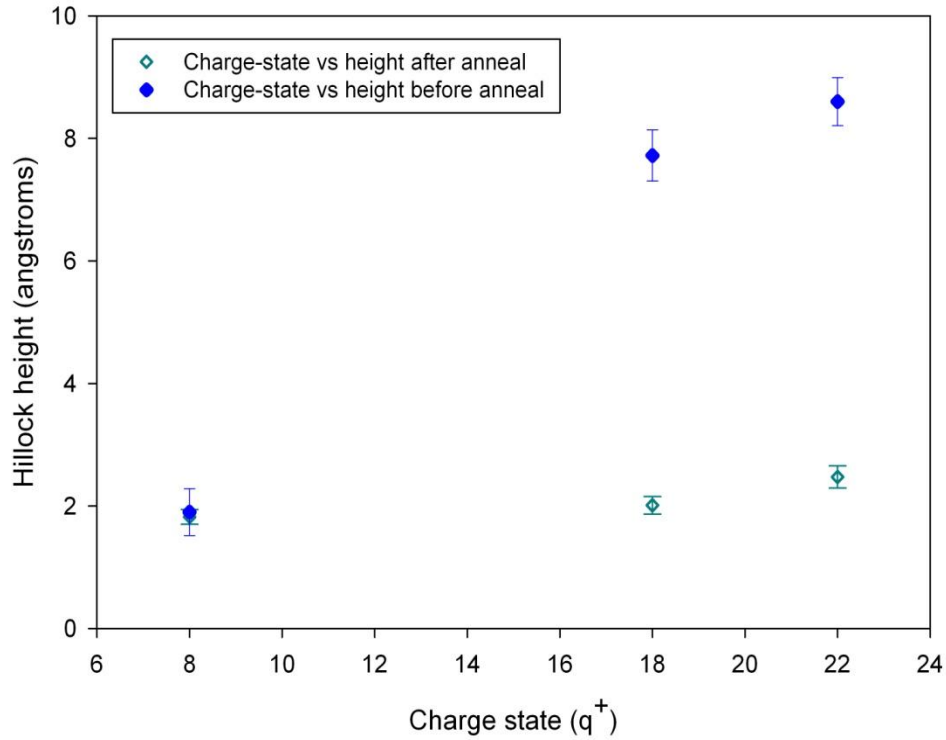


Figure 5.10 Comparison of (average) hillock heights induced on HOPG before and after annealing as a function of the charge state of the incident Sb ions.

Table 5.2, figure 5.9 and figure 5.10 show a summary of results from observed nanodefects after annealing. The results show a direct proportionality between the defect diameter and the defect height with the charge state of the incident ions. Both the defect diameter and the hillock height seem to be reduced following annealing as seen in figure 5.9 and figure 5.10. This effect is observed in all impact sites for charge states investigated in this work. The observed reduction in defect diameter and hillock height after annealing is attributed to surface reconstruction facilitated by high temperature and

a hydrogen atmosphere. Error analysis of the data after annealing followed a similar procedure as before annealing using equations 5.1 and 5.2.

5.4 Raman Spectroscopy

Raman spectroscopy, in particular micro Raman spectroscopy, has been used widely in studies of carbon based nanomaterials. Meguro *et al.* [16] studied ion impact induced diamond-like nanostructures using Raman spectroscopy and observed a signal corresponding to the Raman shift for diamond.

The present Raman study was conducted on the HOPG sample as detailed in section 4.5 to assess firstly the radiation damage on the region irradiated with highest charge state of Sb, i.e. Sb^{22+} and secondly, the possible creation of nanodiamonds/DLC following annealing in a hydrogen atmosphere.

Results from Bi^{35+} implantation on a similar HOPG sample are also presented in this work. The HOPG sample was irradiated under normal incidence with Bi^{35+} ions where the ion fluence was $\sim 100 \text{ ions}/\mu\text{m}^2$ as in the Sb case. However, only SHCI implantation has been conducted in this sample. No post irradiation surface treatment or annealing has been performed on this particular HOPG sample. As a result, only pre-annealing results are presented for the Bi^{35+} implantation study.

Raman spectroscopy results before annealing

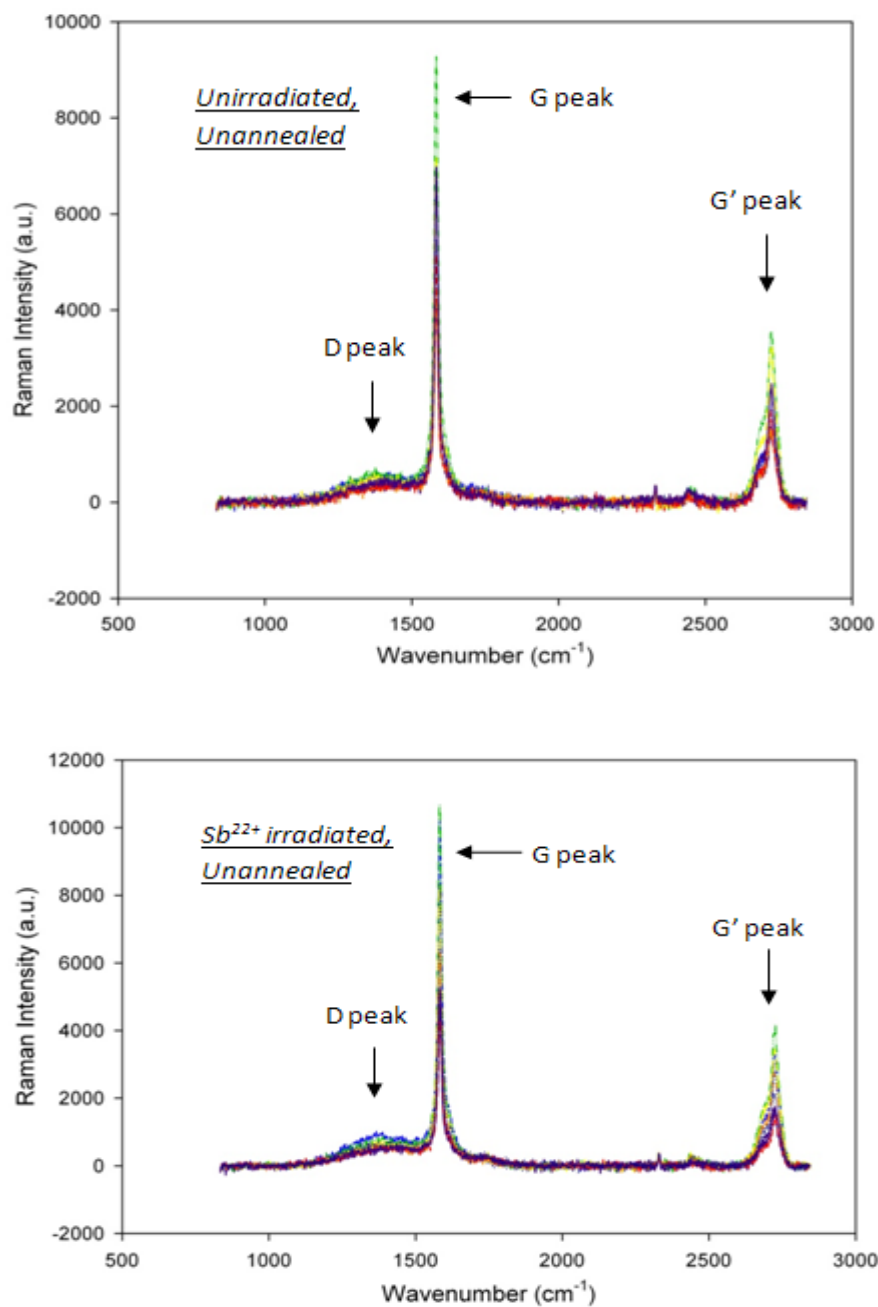


Figure 5.11 Raman intensity maps (8 X 8 points) of the unannealed, unirradiated (top) and the unannealed, Sb²²⁺ irradiated regions of the sample (bottom) acquired using 600 lines/mm grating and a 50X objective lens

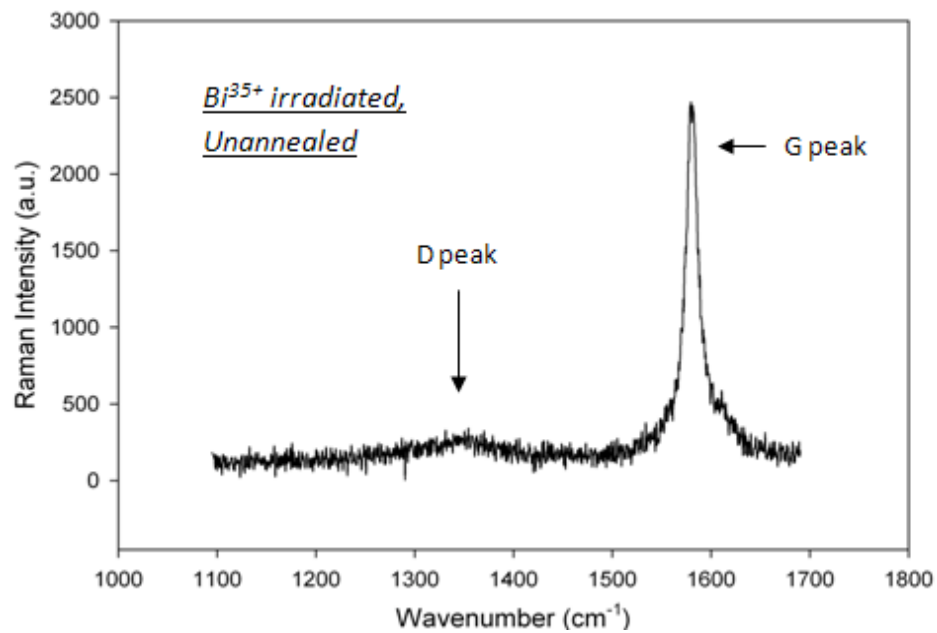
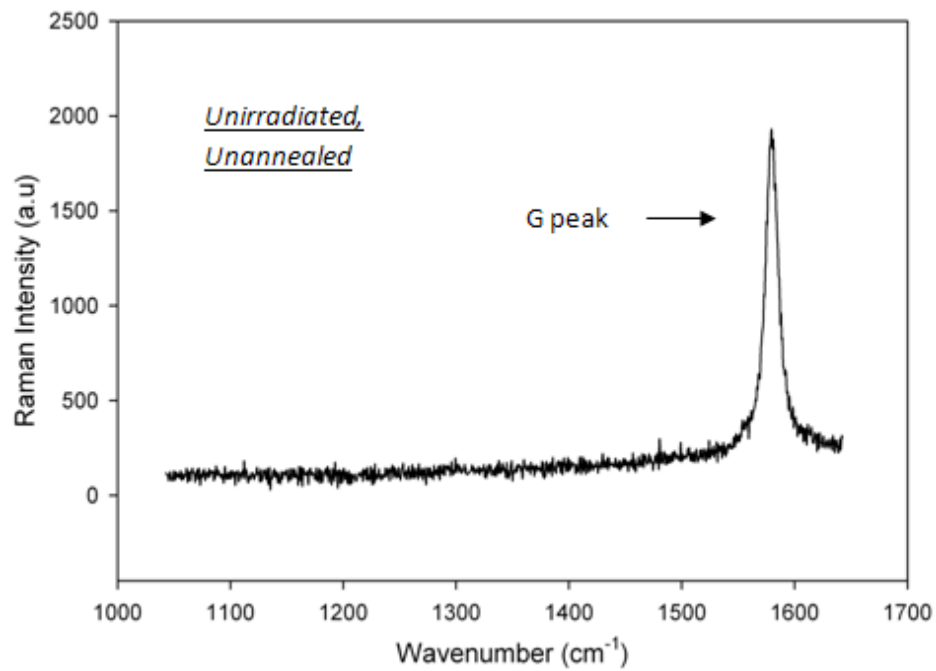


Figure 5.12 Raman spectroscopy spectra showing unirradiated HOPG (top) and Bi³⁵⁺ irradiated HOPG (bottom) acquired using the 1800 lines/mm grating and a 50X objective lens.

In general, common Raman peaks observed in graphitic materials are; the D peak, the G peak, the D' peak and the G' peak corresponding to 1358 cm^{-1} , 1581 cm^{-1} and 1620 cm^{-1} and 2700 cm^{-1} respectively.

Origin of Observed Raman Peaks

- **D and D' peaks**

The D peak and D' peak are both defect induced Raman features (e.g. following irradiation by singly or multiply charged ions). The integrated Raman intensity ratio, I_D/I_G for the D and G bands is widely used for characterizing defect quantity in graphitic materials [171].

- **G Peak**

The G peak is a doubly degenerate in-plane transverse optic (iTO) and longitudinal optic (LO) phonon mode at the Brillouin zone center that is active for sp^2 carbon networks [171].

- **G' Peak**

All graphitic materials exhibit this peak in the range (2500, 2800) cm^{-1} corresponding to an overtone of the D peak. It is a second order peak and is very sensitive to the stacking order of the graphite sheets along the c -axis (perpendicular to the sample surface) [171].

In figure 5.11, Raman spectroscopy maps of the unannealed sample are displayed. In the figure, Raman maps were acquired over the unirradiated region and in the second figure over the Sb^{22+} irradiated region for comparison. Inspection of figure 5.11 reveals three prominent peaks, namely; the D peak, the G peak and the G' peak. The D' peak (1620

cm^{-1}) that is usually associated with disorder in graphite is not clearly seen in the two maps in figure 5.11, however, asymmetry of the G peak seen in both maps is largely attributed to the presence of the D' peak.

The two Raman maps in figure 5.11 appear to be very similar, however, only a slight increase in the D peak following irradiation can be seen in some regions. The low intensity of the D peak is attributed to low radiation damage caused by the incident Sb^{22+} ions. Also, the spatial resolution of the micro Raman facility used in this work has a limit of approximately $0.314 \mu\text{m}$ set by the Abbe' criterion as discussed in section 4.5.

In figure 5.12, Raman intensity profiles of an unirradiated (top) and Bi^{35+} irradiated HOPG sample are shown. The G peak is seen in both profiles; however, in the second profile (irradiated) a broad D peak can be clearly seen around 1358 cm^{-1} . This peak is attributed to radiation damage created by Bi^{35+} impact on the surface and near surface regions.

As discussed in chapter 2 of this work, the potential energy of SHCIs is proportional to the charge state of the SHCIs. Now in this case, the ion fluence used is approximately the same as in the Sb^{22+} case the extraction potential remained constant at $\sim 5 \text{ kV}$. Therefore according to equation 4.1, the corresponding kinetic energy of Bi^{35+} ions is $\sim 175 \text{ keV}$. Two factors are therefore responsible for the observed radiation damage induced by Bi^{35+} in HOPG, namely; the kinetic energy and the potential energy associated with high ionization state of the projectiles.

Raman spectroscopy results after annealing

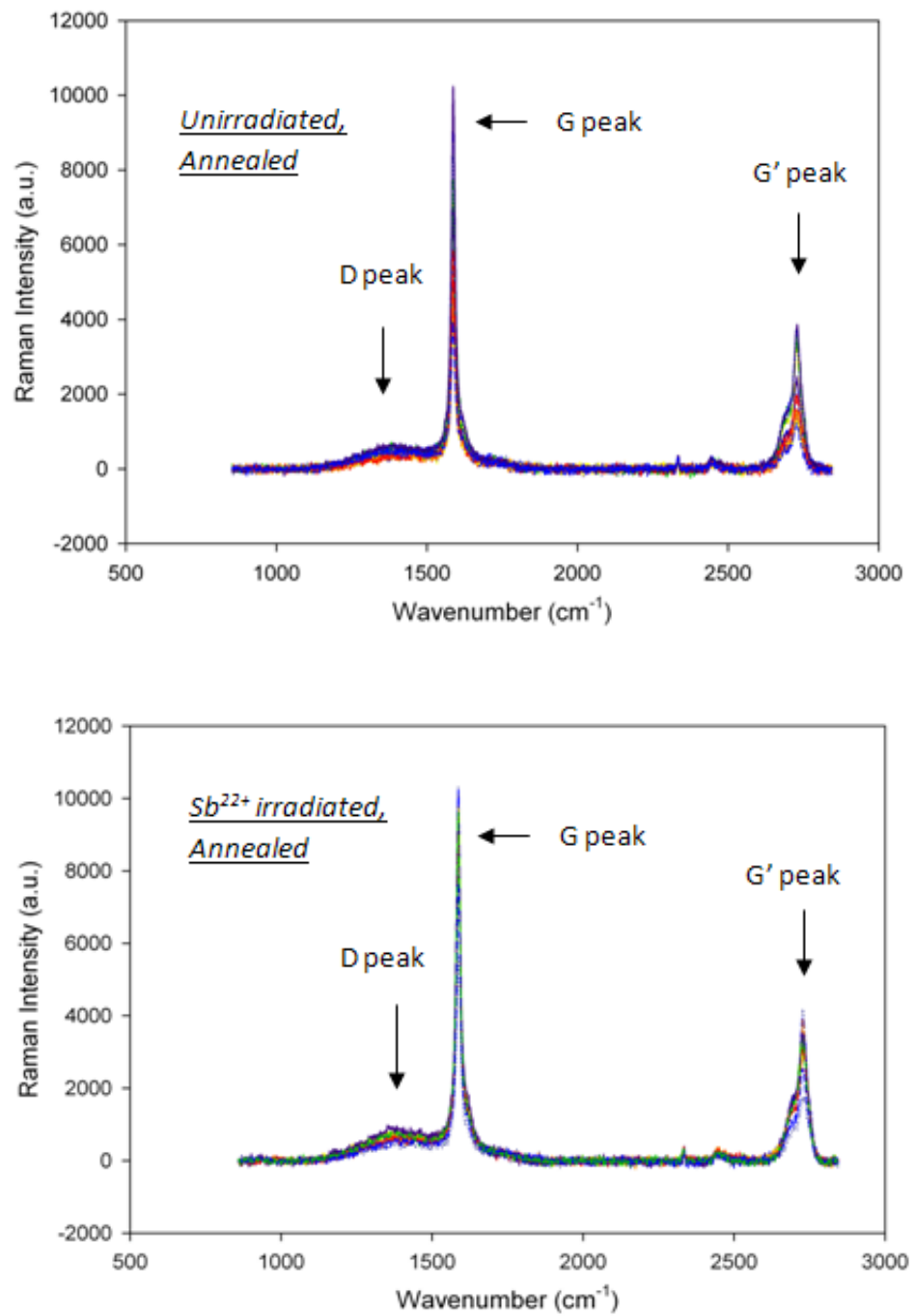


Figure 5.13 Raman intensity map (8 X 8 points) over the unirradiated spot (top) and the Sb²²⁺ irradiated spot (bottom) after annealing using a 600 lines/mm grating and a 50X objective lens.

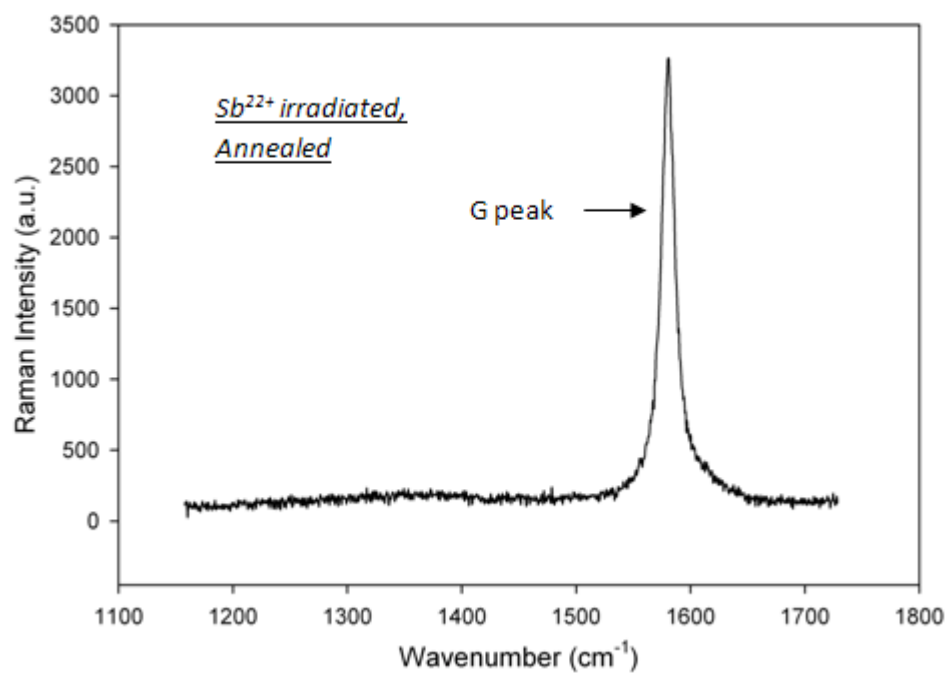
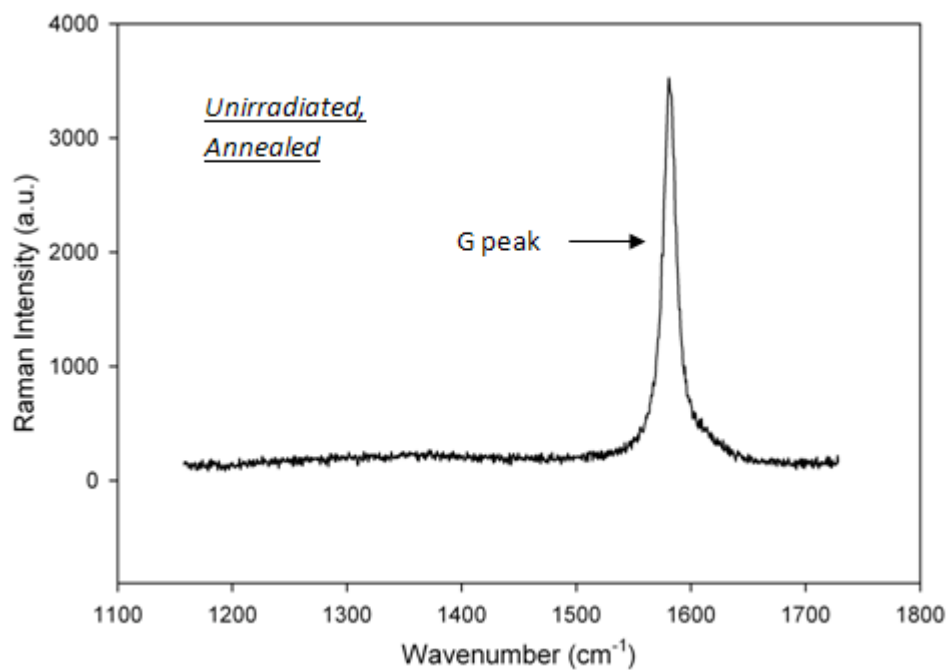


Figure 5.14 Raman spectra acquired over a random spot in the unirradiated region (top) and in the Sb²⁺ irradiated region (bottom) after annealing using the 1800 lines/mm grating and 50X objective lens.

Figure 5.13 and 5.14 shows Raman spectroscopy results acquired after annealing. In figure 5.13 Raman maps were acquired using the 600 lines/mm grating and the 50X objective lens whereas in figure 5.14, Raman profiles over a random spot in the unirradiated and the irradiated regions were acquired using the 1800 lines/mm grating and the 50X objective lens.

As in figure 5.11 and 5.12 the most prominent peaks observed are the D, G and G' peaks. In both figures 5.13 and 5.14 the radiation damage induced by the SHCIs is not pronounced as observed through the D peak. However, a slight increase in the D peak can be seen in some regions following irradiation. The low intensity of the D peak is attributed to low spatial resolution of the Raman equipment used, low charge state of the SHCIs (e.g. relative to Bi^{35+}) hence relatively lower kinetic and potential energy and also temperature and hydrogen assisted surface reconstructions.

It has been reported that the FWHM of the G band and the intensity of the D peak closely relates to the crystallinity of HOPG [172, 173]. Figure 5.15 shows the FWHM of the G peak increases as a function of the intensity ratio of the D and G peaks, (I_D/I_G), in the case of $q = 1, 3, 7$ and 8 . It is important to note that this result indicates that defect formation is directly proportional to the charge state of the incident SHCIs. Defect formation (highest charge states) in HOPG will result in a least crystalline HOPG hence the highest values of FWHM of the G band correspond to highest charge states as seen in figure 5.15.

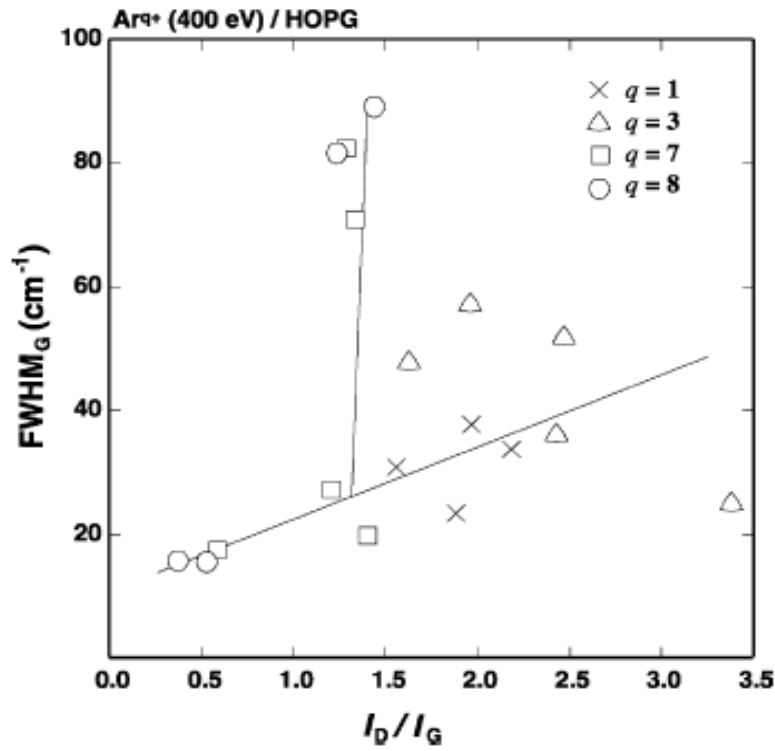


Figure 5.15 FWHM of the G peak as a function of the I_D/I_G [16].

Raman Signal Deconvolution

The Raman spectra shown in figures 5.11 to 5.14 were further analyzed carefully using Lorentzian peak fitting method in order to reduce the composite Raman spectroscopy signal into its individual components. Using this method, one can then extract relevant parameters such as peak intensities, the full width at half maximum of the G peak ($FWHM_G$) and estimation of their corresponding errors.

Figures 5.16 and 5.17 shows examples of results from Lorentzian peak fitting using a Lorentzian function of the form:

$$y = y_0 + \frac{2 \cdot A}{\pi} \frac{w}{4(x - x_0)^2 + w^2} \quad (5.4)$$

where A is the area under the curve, x_0 is the peak center and w is the full width at half maximum (FWHM).

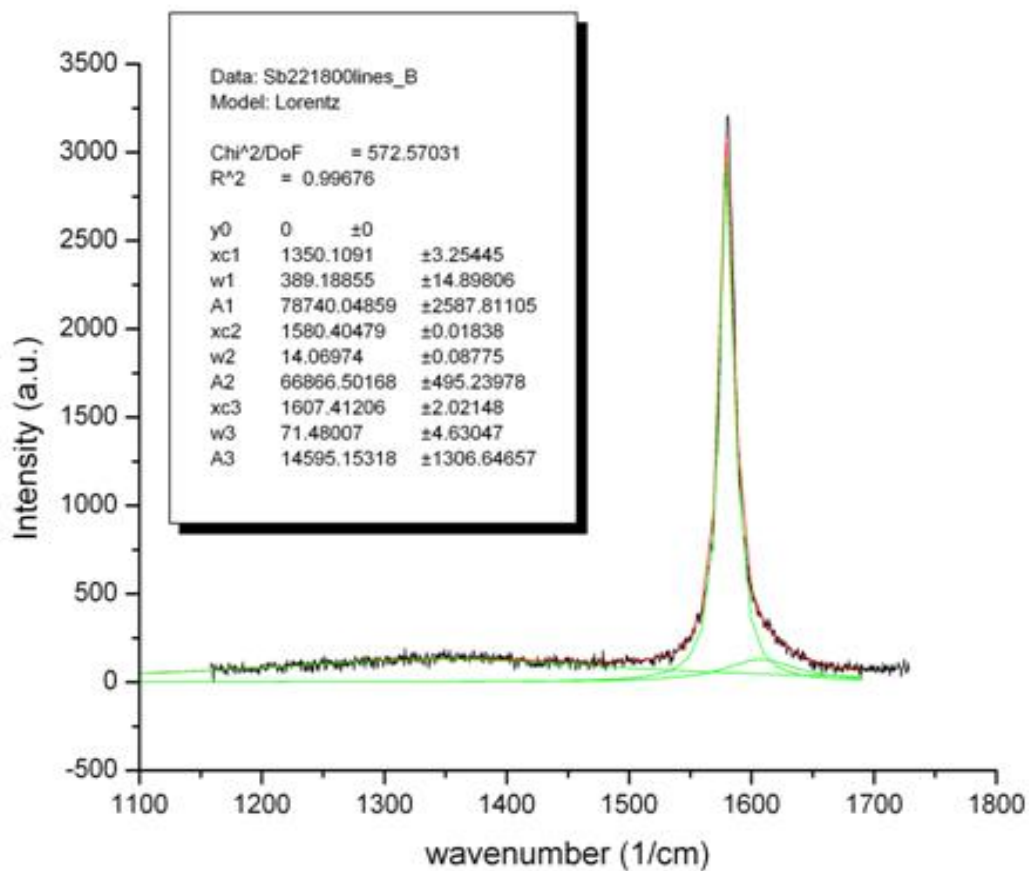


Figure 5.16 Lorentzian peak fitting of Raman data collected over the Sb^{22+} impact site after annealing using the 1800 lines/mm grating and a 50X objective lens. The red line is the fit of the data and the green lines are Lorentzian components of the fit.

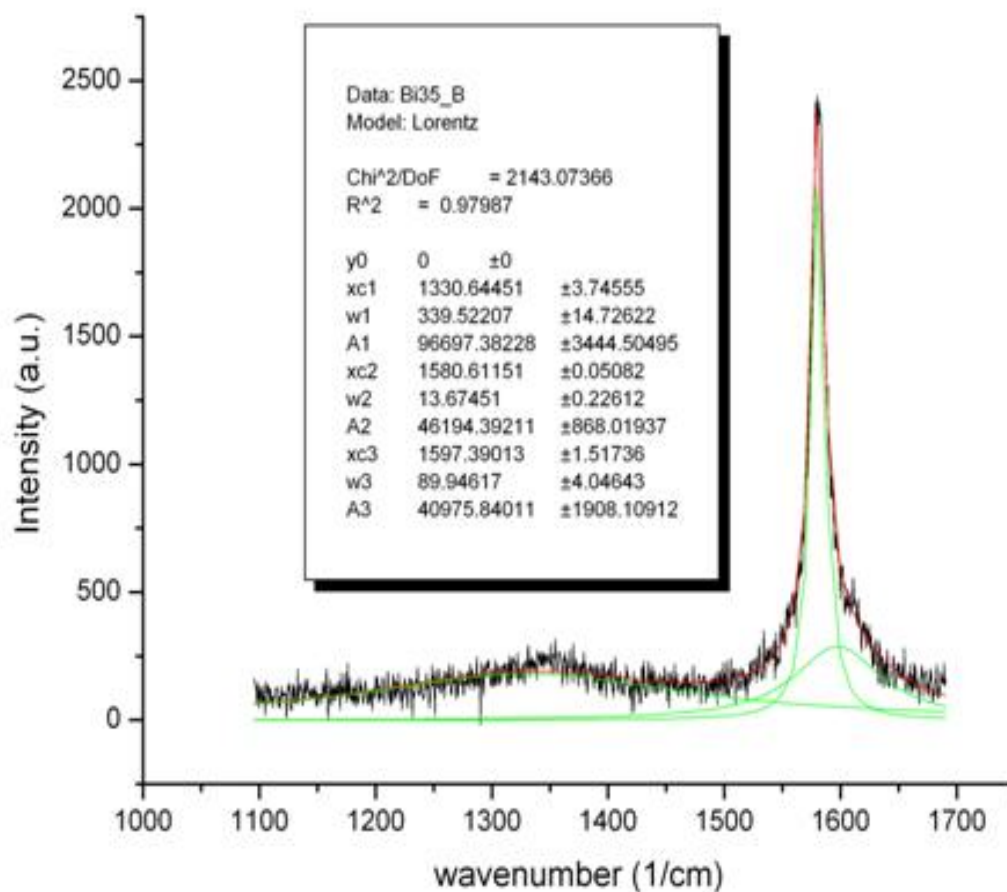


Figure 5.17 Lorentzian peak fitting results of the Bi^{35+} irradiated HOPG (unannealed). The red line is the fit of the data and the green lines are Lorentzian components of the fit. The Raman data was acquired using a 1800 lines/mm grating and a 50X objective lens.

The deconvolution results show in a quantitative manner that the D peak in irradiated, unirradiated, annealed and annealed HOPG is relatively broad in wavenumber space (see figures 5.16 and 5.17) and has a very low intensity. Therefore, the overall radiation damage created by Sb^{22+} is low (before and after annealing) compared to that created by Bi^{35+} before annealing.

The ion fluence is kept constant for Bi³⁵⁺ and Sb²²⁺ implants, therefore the charge state of the incident ions play a more important role in the radiation damage induced in HOPG. A summary of results acquired from deconvolution of the Raman spectra before and after annealing using a Lorentzian function of the form shown in equation 5.4 is shown in tables 5.3 and 5.4.

Table 5.3 Summary of Raman results obtained from Lorentzian peak fitting before annealing.

Parameter	HOPG 1		HOPG 2	
	Unirradiated	Sb ²²⁺ irradiated	Unirradiated	Bi ³⁵⁺ irradiated
FWHM _C (cm ⁻¹)	14.0±0.0912	14.2±0.103	13.4±0.0182	13.7±0.0226
I _D /I _G (x 10 ⁻²)	5.10±0.601	10.3±0.952	8.14±0.514	8.86±0.687
Charge State (q ⁺)	0	22	0	35

Table 5.4 Summary of Raman results obtained from Lorentzian peak fitting after annealing.

Parameter	HOPG 1	
	Unirradiated	Sb ²²⁺ irradiated
FWHM _C (cm ⁻¹)	13.2±0.0825	14.1±0.0876
I _D /I _G (x 10 ⁻²)	4.79±0.422	4.87±0.465
Charge State (q ⁺)	0	22

Inspection of tables 5.3 and 5.4 show a strong correlation between the charge state (hence potential and kinetic energy) of the incident SHCIs with the disorder induced in the target surface as quantified by (I_D/I_G) and FWHM_G . The ratio of the intensity of the D peak to that of the G peak, (I_D/I_G) and the full width at half maximum of the G peak, FWHM_G are both directly proportional to the charge state of the incident SHCIs.

The observed Raman results as summarized in tables 5.3 and 5.4 are in agreement with previous studies [16, 174, 175]. In both HOPG samples, the disorder increases following irradiation. However, Bi^{35+} creates more radiation damage in HOPG than Sb^{22+} . This observation is confirmed by the larger (I_D/I_G) value following Bi^{35+} irradiation as seen in table 5.3.

After annealing, the FWHM_G together with (I_D/I_G) decrease in both the unirradiated and the Sb^{22+} irradiated regions of the sample. These observations are in agreement with expectations because the high temperature and the hydrogen introduced into the annealing furnace together catalyze surface reconstructions from sp^2 bonding into sp^3 bonding. Therefore, an overall decrease in disorder is observed from Raman spectroscopy following annealing and is attributed surface reconstructions.

It has been reported that on the nanoscale, energetics of surface reconstructions favour the reconstruction of graphite into diamond [123, 124]. However, in general, catalysts are required to reduce the activation energy required for the transformation (hence high temperature and hydrogen were utilized in the surface treatment phase of this work). Nevertheless, Raman spectroscopy was not able to detect sp^3 phases of carbon corresponding to 1331 cm^{-1} (see figure 5.13 and 5.14) primarily due to the low spatial

resolution of the equipment used and the low number of defects per unit area (hence low Raman intensity) of the induced nanodefects.

5.5 Photoluminescence (PL)

The setup used to acquire PL data in the present work is similar to that used for Raman spectroscopy data acquisition. That is, in the PL setup, a 514 nm excitation wavelength was used. All PL data was acquired using a 600 lines/mm diffraction grating. However, one set of data was acquired using a 50X objective lens and another using a 100X objective lens for higher resolution (lower collection efficiency) and higher collection efficiency (lower resolution) respectively.

Only the PL results acquired using the 50X objective lens (higher resolution) are presented in this work for brevity (see figure 5.19). Following Raman spectroscopy analysis, the next step was to investigate the photoluminescence properties of the Sb^{22+} induced nanodefects after annealing.

The photoluminescence of nanodiamonds has been studied by several authors [176, 177, 178]. Figure 5.18 shows PL results from nanodiamonds of different sizes acquired using a 532 nm laser. For nanodiamonds less than 50 nm in diameter, one expects a PL signal around 630 nm. However, PL signatures for DLC have been observed in different wavelengths depending on several properties such as sp^2/sp^3 ratio and the presence of impurities such as Nitrogen and Hydrogen. In the present study the acquired PL spectra do not show any significant change following annealing (see figure 5.19).

This observation is attributed to the low spatial resolution of the PL setup (similar to the Raman setup) and also thermal noise which is likely to interfere with the expected low intensity nanodiamond/DLC signal (PL data was acquired at room temperature and ambient pressure). Note: the sharp peaks appearing at 618 nm and 707 nm are spikes in the Sb^{22+} irradiated data, these do not represent any change in the material properties.

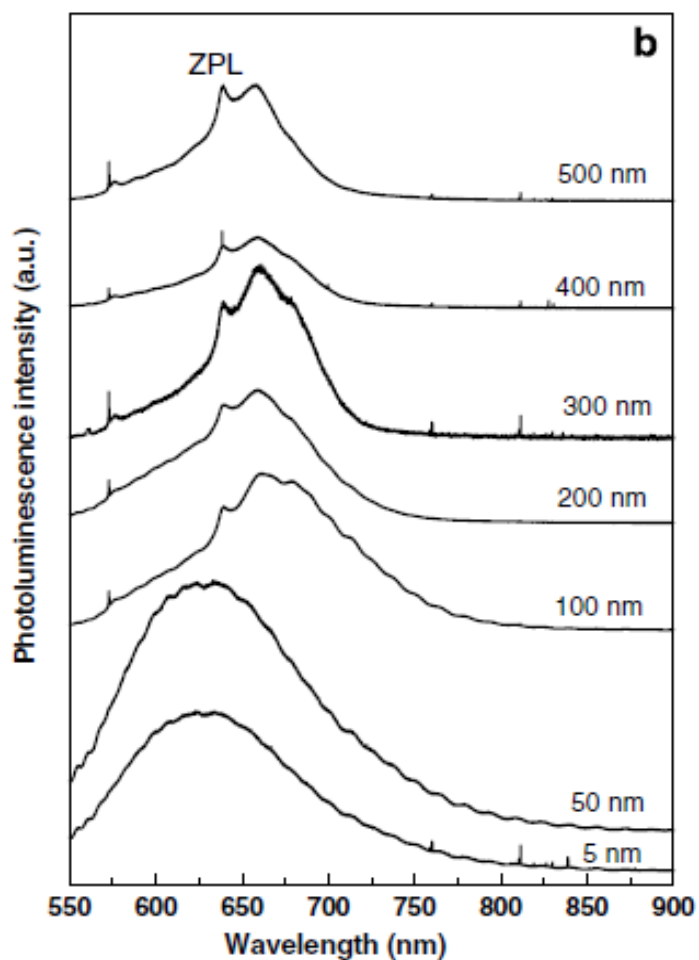


Figure 5.18 PL spectra of nanodiamonds of different sizes acquired using a 532 nm excitation laser [176]. Note: ZPL refers to the zero phonon line.

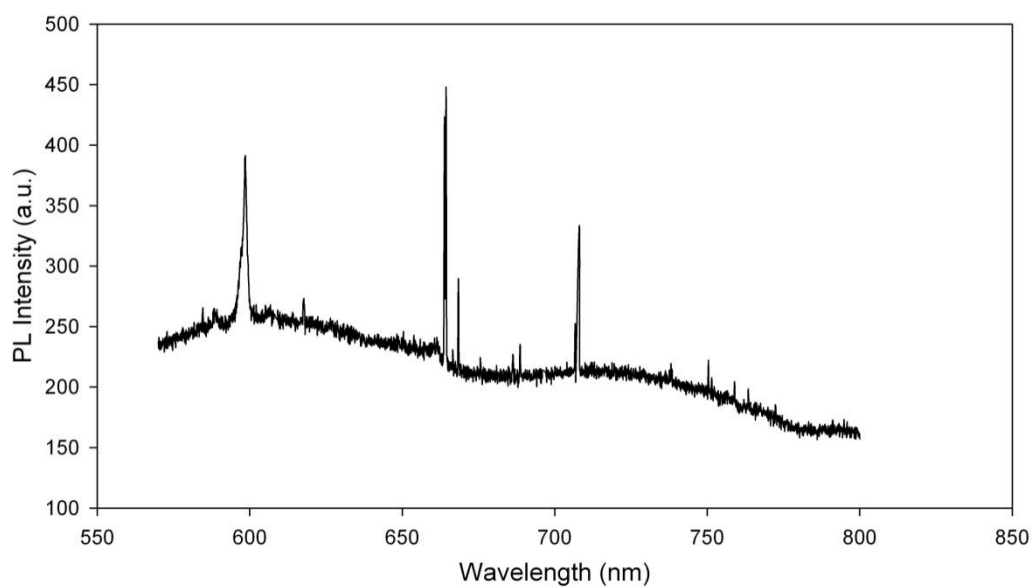
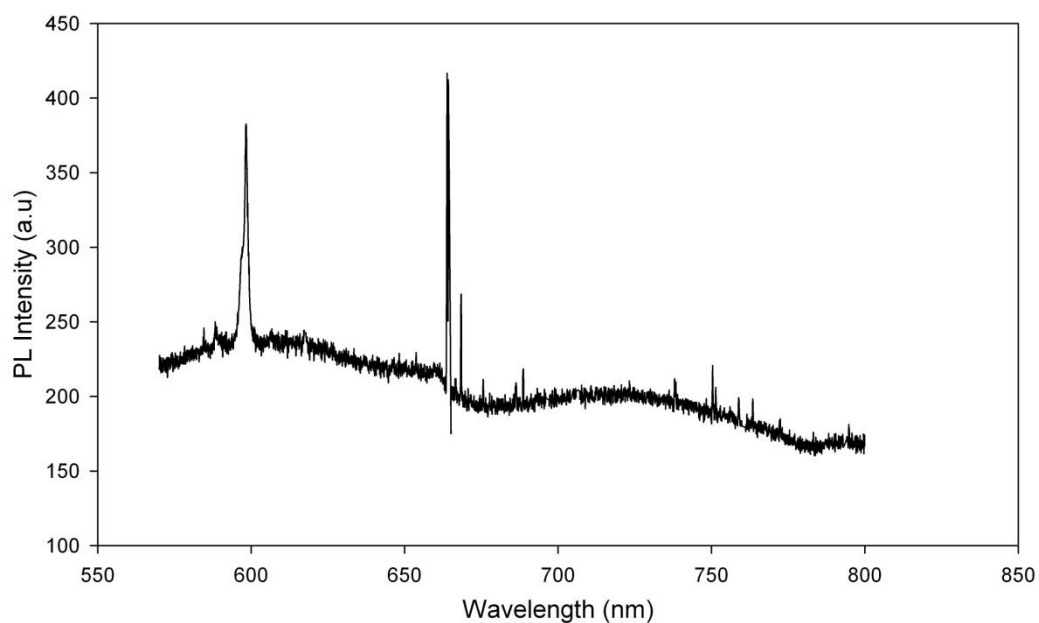


Figure 5.19 PL intensity spectra taken over the unirradiated site (top) and the Sb²²⁺ irradiated (bottom) impact site on HOPG using a 50X objective lens, a 600 lines/mm grating and a 514 nm excitation laser.

5.6 Scanning and Tunneling Spectroscopy (STS).

In order to conduct spectroscopy measurements on the HOPG sample, STM imaging of surface is necessary. This was achieved by scanning a PtIr tip across the sample with a sample-tip separation of several angstroms. An example of an STM image acquired over the Sb^{22+} impact site is shown in figure 5.20. The STM images were then zoomed into using CPIX software routines in order to obtain a larger view of the nanod defect.

It is important to note that STM imaging is prone errors in lateral measurements induced by the tip-sample electronic interaction. As a result, the true dimensions of defects may be obscured when observed using STM. However, amongst other reasons (see section 4.4.2), STM is very useful in that it allows one to conduct spectroscopy measurements that can give accurate semi-quantitative electronic structure information. Figure 5.20 shows a series of points along which individual I-V curves (figure 5.21) were collected to investigate electronic properties of the defects at Sb^{22+} and Sb^{18+} impact sites.

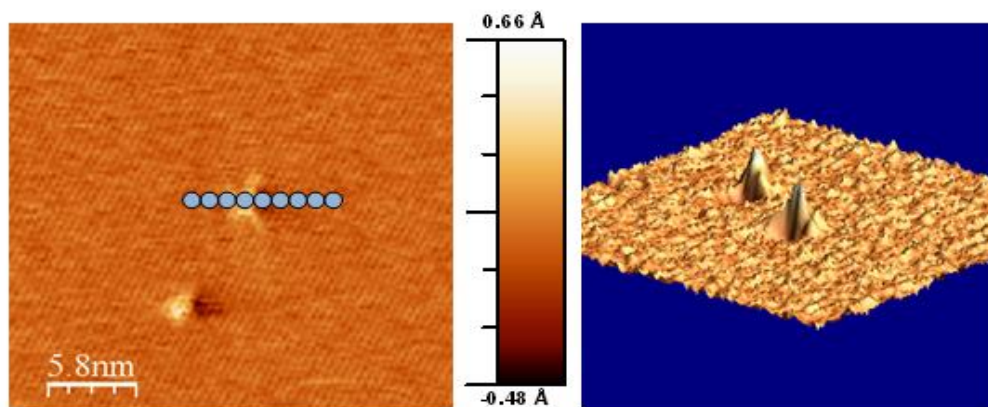


Figure 5.20 STM image showing Sb^{22+} induced nanodefects on HOPG and the points along which I-V curves were acquired. The 3D image has the same x-y scale as the 2D image.

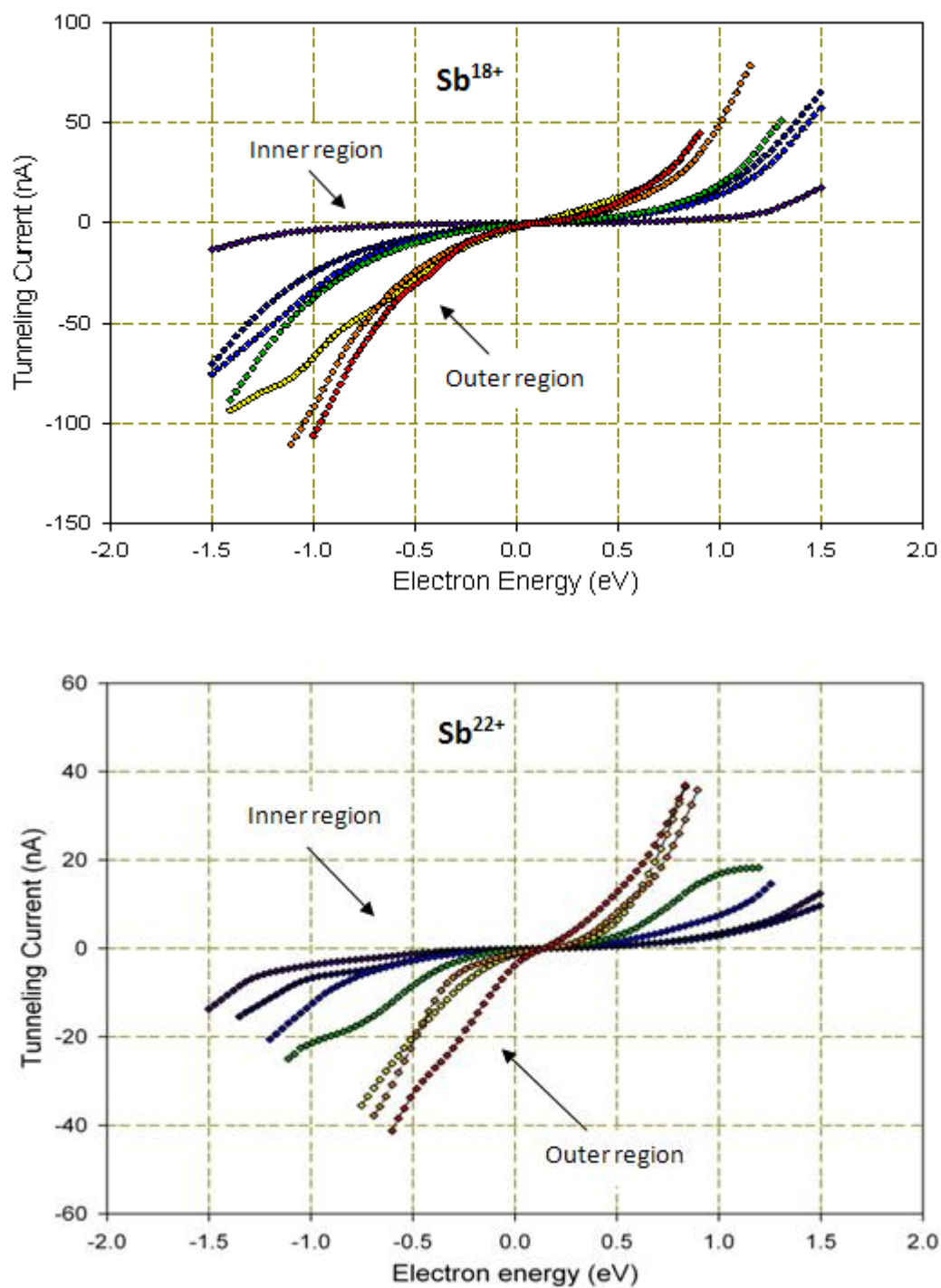


Figure 5.21 I-V curves acquired over the Sb^{18+} (top) and Sb^{22+} (bottom) nanodefects on HOPG after annealing showing the inner to the outer regions of the nanodefects.

Figure 5.21 shows I-V curves acquired over Sb^{18+} and Sb^{22+} impact sites on HOPG. In both cases, the I-V curves show that, towards the center of the nanodefekt, the resistivity increases and gradually decrease towards the outer regions of the nanodefekt. Such behaviour has been reported previously in literature [125].

The first derivative of the I-V curves and the normalized differential currents (see section 4.4.2) have been widely used to give insight into local electronic structure of the material under investigation. Figure 5.22 shows results from taking the first derivative of the I-V curves shown in figure 5.21.

Several interesting features can be seen in figure 5.22. Firstly, the Fermi energy is found to be at about 0.112 eV and 0.164 eV for the Sb^{18+} and Sb^{22+} induced defects respectively. A clear clustering of similar curves is seen in the Sb^{18+} induced defect and labeled A-C and D in the Sb^{22+} induced defects. Such clustering suggests a similarity in the electrical properties of the localized materials from which tunneling data is acquired.

It has been reported that the normalized differential current curves resemble a closer representation of the local electronic states [154]. Figure 5.23 and 5.24 shows the normalized differential current curves and the truncated normalized differential current curves. In figure 5.23, discontinuities in the data are seen around 0.09 eV and 0.14 eV for the Sb^{18+} and Sb^{22+} induced nanodefekts respectively.

These discontinuities are only consequences of the mathematical procedure of the derivative which involves division by values that are close to zero but do not represent any known physical information. Therefore, these discontinuities are referred to as artificial discontinuities.

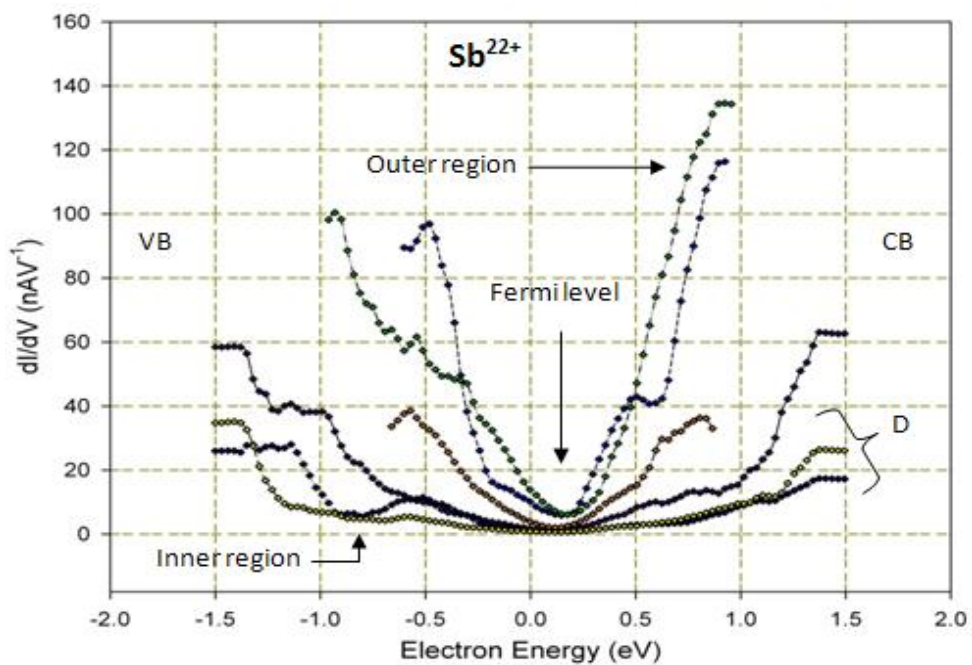
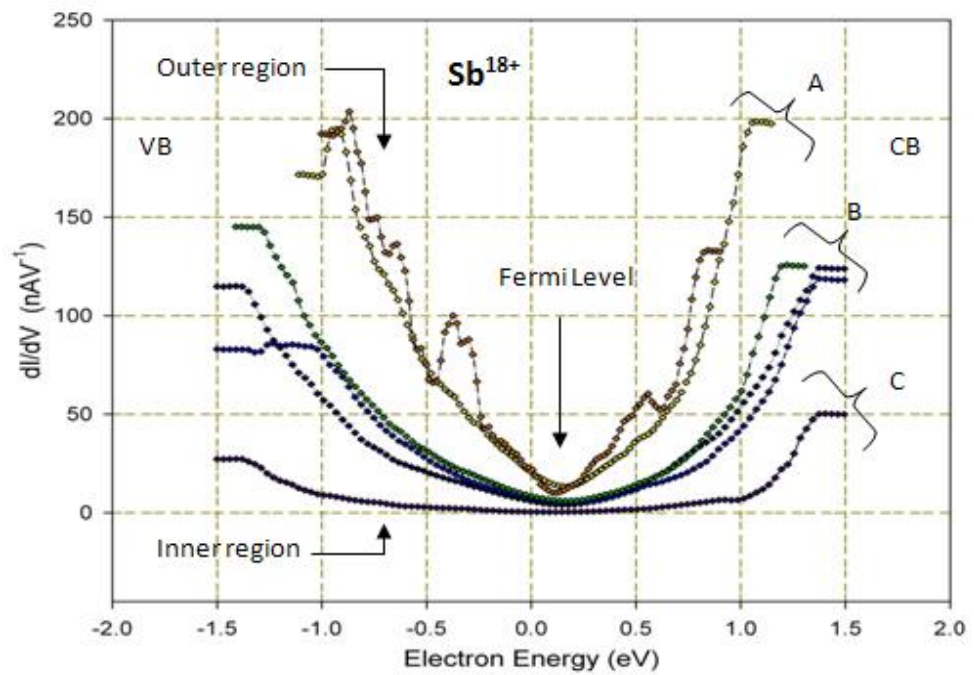


Figure 5.22 Differential current curves for Sb^{18+} (top) and Sb^{22+} (bottom) induced nanodefects showing the valence (VB) and conduction bands (CB) with respect to the Fermi level, curves from the inner and outer regions on the nanodefect and also the clustered curves labeled A-D.

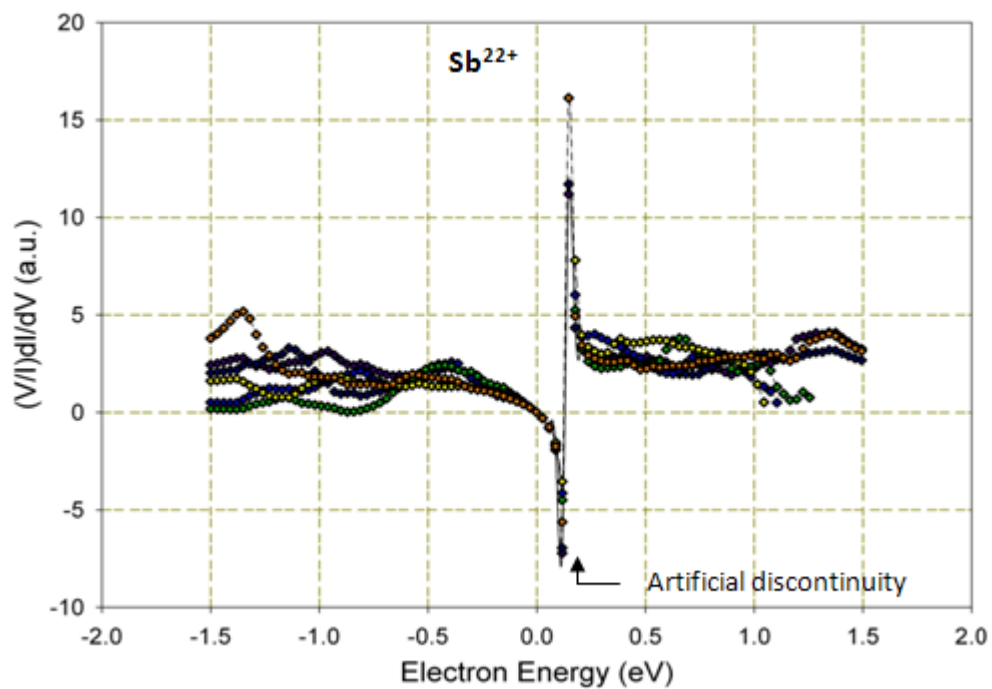
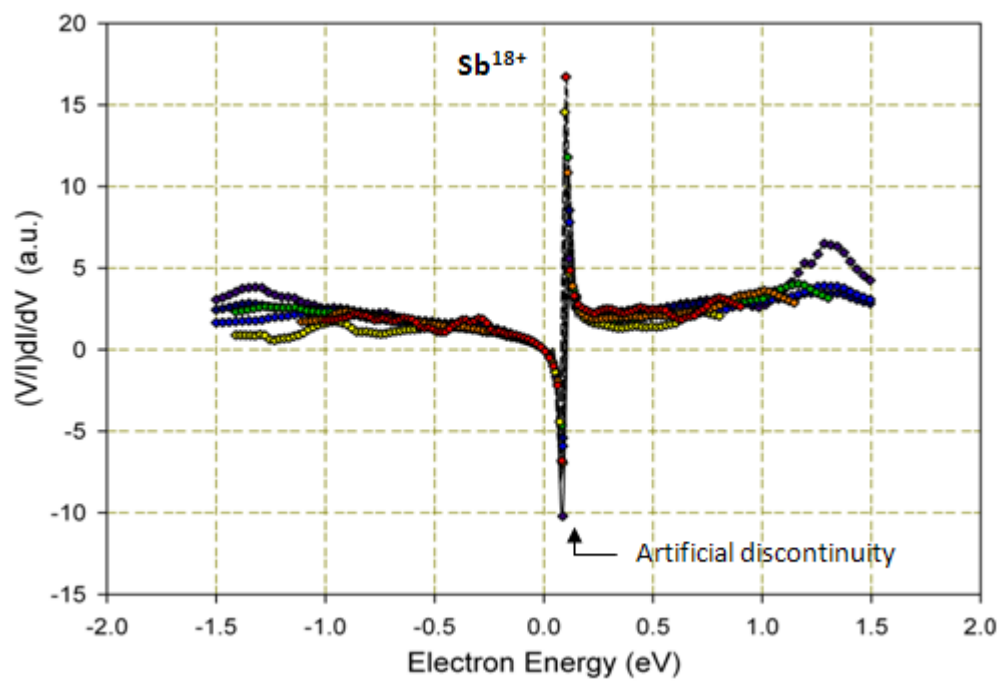


Figure 5.23 Normalized differential curves taken over Sb^{18+} (top) and Sb^{22+} (bottom) induced nanodefects on HOPG.

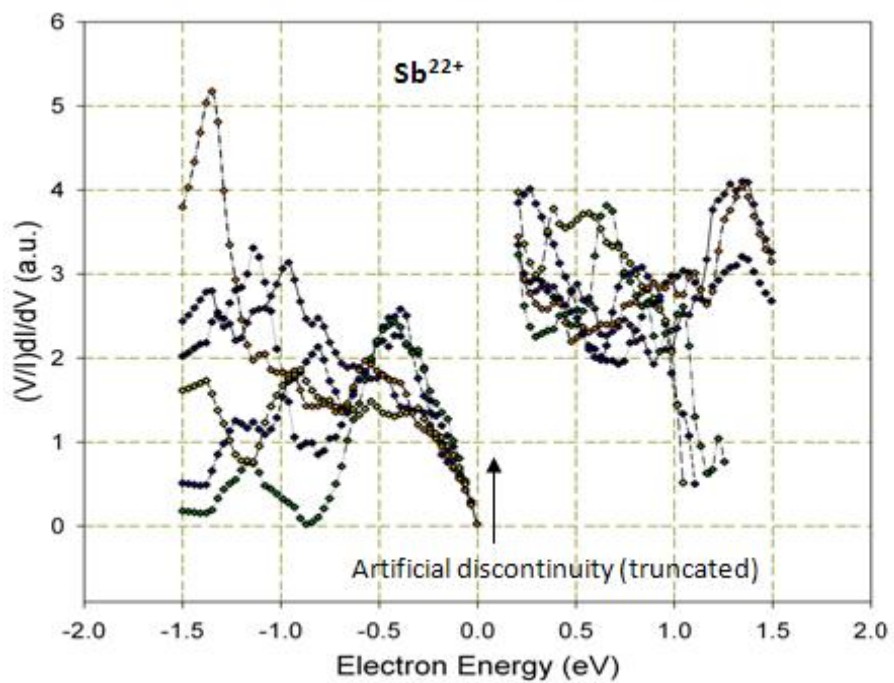
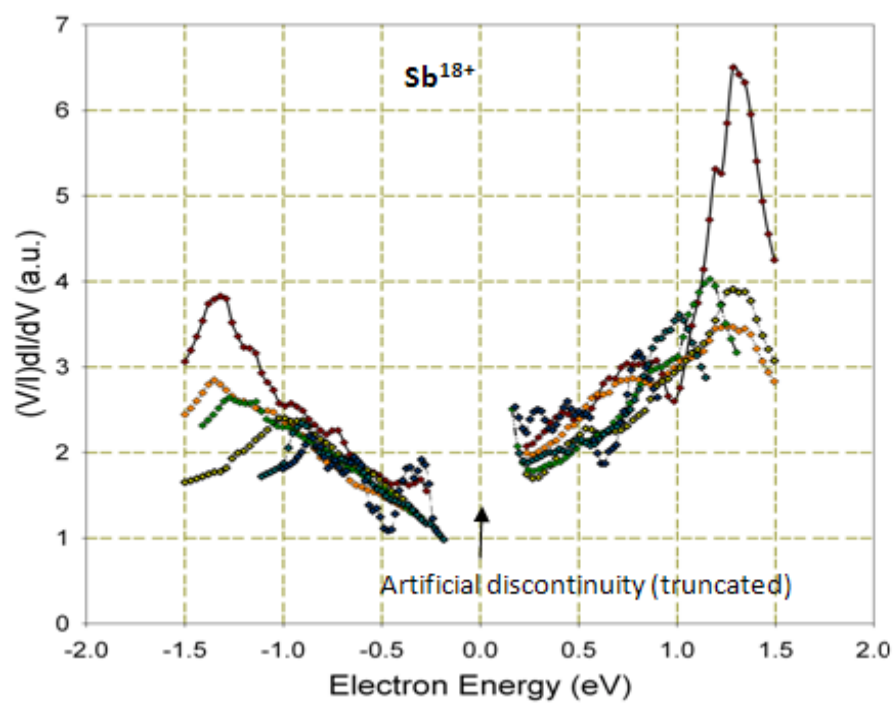


Figure 5.24 Truncated normalized differential curves taken over Sb^{18+} and Sb^{22+} nanodefects.

When presenting normalized differential current curves, the discontinuity is commonly truncated to avoid obscuring important information in the data (see figure 5.24). Analysis of figure 5.24 shows that the structure in the local electronic DOS is complex for modest acquisition conditions used for both the Sb^{18+} and Sb^{22+} cases.

In order to carry out a conclusive analysis of nanodefects based on the structure of the local electronic DOS, a statistical ensemble of I-V curves collected at different nanodefects for each charge state would be necessary and also less noise in the acquired data (considering that the data was acquired in ambient pressure and room temperature) would yield a more accurate and conclusive analysis.

However, although it is not obvious to map out the electronic structure from the given normalized differential current curves, it is possible to make semi-quantitative estimates of the electronic energy band gap of the materials being studied. Ivanov-Omskiĭ *et al.* [155] demonstrated electronic energy gap estimation using differential current curves (see figure 4.19).

Figure 5.25 shows electronic energy band gap estimation using a procedure similar to that used by Ivanov-Omskiĭ *et al.* Only materials with highest electronic energy band gap, (E_g) are plotted against HOPG which has a known electronic energy band gap. The estimated electronic energy band gap for the Sb^{18+} and Sb^{22+} induced nanodefects are ≈ 2.05 eV and ≈ 2.33 eV respectively. DLC has been reported to have a band gap of ≈ 1.5 - 2.6 eV [155, 178]. These values show an electronic transformation from graphite (blue curve in figure 5.25) to DLC (red curve) in the irradiated regions following surface treatment as described in chapter 4.7.

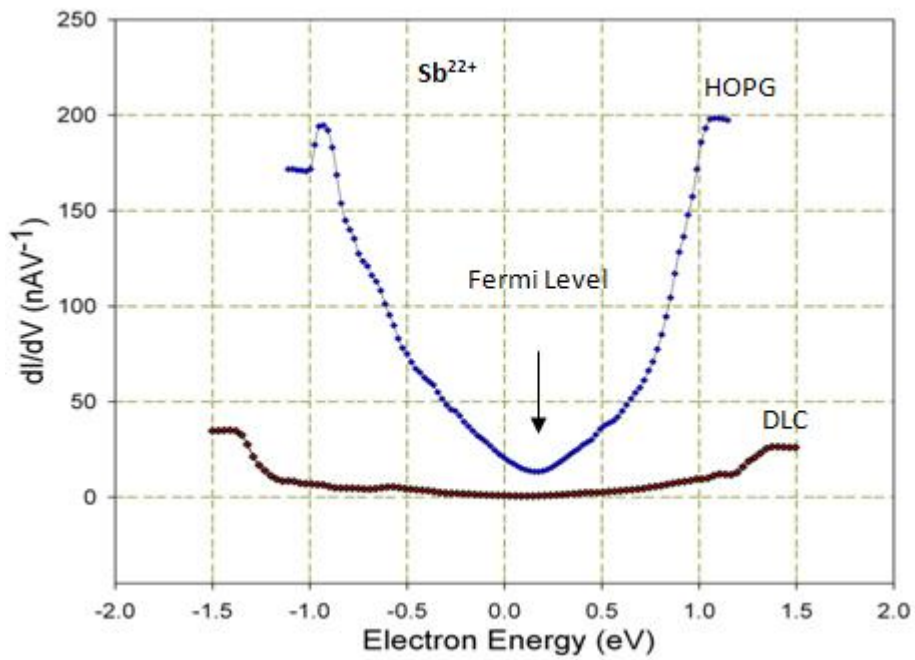
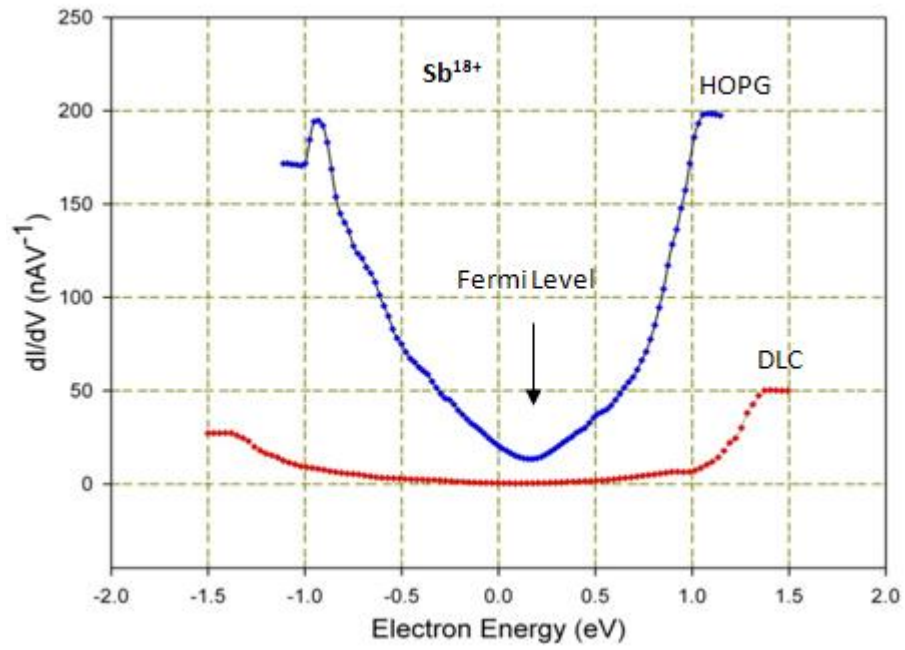


Figure 5.25 Plot showing the maximum electronic energy band gap (E_g) Sb^{18+} (top) and Sb^{22+} (bottom) induced nanodefects (red curve) on HOPG in comparison to graphite (blue curve).

Chapter 6

6. Conclusions

After thorough analysis and interpretation of results presented in chapter 5 of the present work, several conclusions can be drawn. Using NC-AFM imaging and analysis, this work provides further evidence for the direct proportionality between the charge state of the incident SHCIs with nanod defect formation in terms of the nanod defect diameter and the hillock height as reported previously by several authors [79, 125, 173, 174].

In the present study, the SHCIs that were investigated namely; Sb^{8+} , Sb^{18+} , Sb^{22+} and Bi^{35+} induced surface nanod defects on HOPG with average diameters of 7.94 ± 0.950 nm, 10.5 ± 0.613 nm, 11.9 ± 0.890 nm and 14.7 ± 0.590 nm with corresponding average hillock heights of 1.90 ± 0.382 Å, 7.72 ± 0.418 Å, 8.60 ± 0.392 Å and 9.72 ± 0.916 Å respectively. El Said *et al.* showed that most materials have a potential energy threshold for the formation of nanod defects [79]. The present study provides evidence that such a potential energy threshold for HOPG occurs at lower charge states than the ones utilized in this work.

Following annealing at 650°C in a hydrogen atmosphere, the diameters of the nanod defects were reduced to 6.372 ± 0.312 nm, 8.66 ± 0.290 nm and 9.15 ± 0.498 nm and

in hillock height to $1.821 \pm 0.121 \text{ \AA}$, $2.01 \pm 0.143 \text{ \AA}$ and $2.473 \pm 0.182 \text{ \AA}$ for the Sb^{8+} , Sb^{18+} and Sb^{22+} impact regions respectively. Therefore, diameter changes of up to 23% (corresponding to Sb^{22+} impact sites) and hillock height changes over 70% (corresponding to Sb^{18+} and Sb^{22+} impact sites) were observed following surface treatment. The observed reduction in both the diameter and the hillock height of the SHCI induced surface nanodefects is attributed to surface reconstruction facilitated by high temperature (at approximately 650°C) and a hydrogen atmosphere.

Results obtained from Raman spectroscopy show that for an ion dose of ~ 100 ions/ μm^2 , electronic transformation of sp^2 into sp^3 phases of carbon is not easily detected by conventional methods. This observation is attributed to the following:

- The spatial resolution of the micro Raman facility used in the present work is limited by the Abbe' Criterion to about 314 nm which is much larger than the average diameter of the SHCI induced nanodefects.
- The density of nanodefects within the area of the laser utilized in the Raman spectroscopy measurements and PL ($\sim 1 \mu\text{m}$) is very low given the small diameter and height of the nanodefects. As a result the corresponding Raman (and PL) signal intensity is very low.
- The diamond Raman line corresponding to sp^3 phases of carbon (diamond) is found at about 1331 cm^{-1} . This line is very close to the D peak which is found at about 1358 cm^{-1} . Therefore, the diamond line is easily obscured by any radiation damage with a characteristic broad D peak.

Nevertheless, although sp^3 carbon phases are not easily detected for the above mentioned reasons, using micro Raman techniques, the present study provides a preliminary method for the assessment of radiation damage induced by SHCIs. The radiation damage by SHCIs is studied in terms of the $FWHM_G$ which represents the crystallinity of HOPG and also the ratio of the intensity of the D peak to the G peak, I_D/I_G which represents the disordered fraction of the material. Results from the assessment of radiation damage using micro Raman techniques show the following:

- $FWHM_G$ is directly proportional to the charge state of the incident SHCIs as previously reported [16, 173].
- The disorder in HOPG as quantified by I_D/I_G is directly proportional to the charge state of the incident SHCIs.
- Annealing HOPG at 650°C for 40 minutes in a hydrogen atmosphere results in a decrease in the $FWHM_G$ and I_D/I_G in both the irradiated and unirradiated regions. This observation is attributed to high temperature and hydrogen assisted surface reconstruction. Therefore, the surface treatment results in a restoration of the HOPG crystallinity and a reduction in surface disorder.

Scanning and tunneling spectroscopy (STS) has shown that following annealing at 650°C for 40 minutes in a hydrogen atmosphere, electronic transformation of SHCI induced nanodefects in HOPG takes place. In the present study, differential current curves calculated from I-V curves acquired by means of the STS technique have shown in a semi-quantitative manner that the electronic energy band gap, E_g of the SHCI induced nanodefects changes from approximately 0 eV (predominantly sp^2 rich form) to

about 2.05 eV and 2.33 eV for Sb^{18+} and Sb^{22+} induced nanodefects respectively which symbolizes significant presence of sp^3 phases of carbon.

The localized materials fabricated in the present study with electronic energy band gaps of approximately 2.05 eV and 2.33 eV correspond to diamond-like carbon (DLC) which has a known electronic energy band gap of ranging between 1.5 eV – 2.6 eV depending on the purity of the DLC and the sp^2/sp^3 ratio [155, 179]. Other radiation based methods of diamond synthesis using beams that are characterized primarily by kinetic effects ($\sim\text{MeV}$) are currently being explored.

Results from the present study therefore provide preliminary measurements for future fabrication of patterned qubits based on N-V centers localized in nanoscale DLC. Preliminary studies geared towards optimizing the cross-section of N-V formation are currently being carried out at Berkeley EBIT in U.S.A.

Single ion implantation of nitrogen into nanoscale DLC synthesized in the present study will provide the unique opportunity of creating nanopatterned arrays of N-V center based qubits which could ultimately be scaled up to develop a functional quantum computer and other useful quantum information devices using advanced nanopatterning apparatus such as the EBIT described in section 4.1.

References

- [1] Wilson, M. *et al.*, *Nanotechnology, basic science and emerging technologies*, Sydney: University of New South Wales Press Ltd., 2002, pp. 3-5.
- [2] Poole Jr., C. P. and Owens, F. J. *Introduction to Nanotechnology*, New Jersey: John Wiley & Sons Inc., 2003, pp. 1-7.
- [3] Gogotsi, Y. *Nanomaterials Handbook*, New York: Taylor and Francis Group, 2006, pp 1-3.
- [4] Aumayr, F. and Winter, H. *Philosophical Transactions of the Royal Society of London*, A362, 2004 pp. 77-102.
- [5] Sigmund, P. ed, *Proceedings on Fundamental Processes in Sputtering of Atoms and Molecules (SPUT 92)*, Copenhagen, 1993.
- [6] Winter, H. P. and Aumayr, F. *Europhysics News*, Vol. 33, No. 215, 2002.
- [7] Arnau, A. *et al.* *Surface Science Reports*, Vol. 229, No. 1, 1997.
- [8] Aumayr, F. and Winter, H. *Electronic Journal of Surface Science and Nanotechnology*, Vol. 1, 2003, pp. 171-174.
- [9] Schenkel, T. *et al.* *Journal of Vacuum Science and Technology*, Vol. B16, No. 3298, 1998.
- [10] Rühlicke, C. *et al.* *Nuclear Instruments and Methods in Physics Research*, Vol. B99, 1995, pp. 528-532.

- [11] Minniti, R. *et al. Physica Scripta*, Vol. T92, 2001, pp. 22-26.
- [12] Gebeshuber, I. C. *International Journal of Mass Spectrometry*, Vol. 229, 2003, pp. 27-34.
- [13] Hamza, A. V. *Applied Physics Letters*, Vol. 79, No. 18, 2001.
- [14] Banhart, F. and Ajayan, P. M. *Nature*, Vol. 82, No. 433, 1996.
- [15] Meguro, T. *et al. Applied Physics Letters*, Vol. 79, No. 3866, 2001.
- [16] Meguro, T. *et al. Nuclear Instruments and Methods in Physics Research*, Vol. B209, 2003, pp. 170-174.
- [17] Nakamura, Y. *et al. Nature*, London: Vol. 398, No. 786, 1999.
- [18] Petta, R. J. *et al. Science*, Vol. 309, No. 2180, 2005.
- [19] Davies, G. and Hamer, M. F. *Proceedings of the Royal Society of London*, Ser. A348, No. 285, 1976.
- [20] Kennedy, T. A. *et al. Applied Physics Letters*, Vol. 83, No. 4190, 2003.
- [21] van Oort, E. *Journal of Physics*, Vol. C21, No. 4385, 1988.
- [22] Charnock, F. T. and Kennedy, T. A. *Physics Review*, Vol. B64, 041201(R), 2001.
- [23] Jelezko, F. *et al. Physical Review Letters*, Vol. 92, 076401, 2004.
- [24] Jelezko, F. *et al. Physical Review Letters*, Vol. 93, 130501, 2004.
- [25] Popa, I. *et al. Physics Review*, Vol. B70, 201203 (R), 2004.
- [26] Gruber, A. *et al. Science*, Vol. 276, No. 2012, 1997.
- [27] Epstein, R. J. *et al. Nature Physics*, Vol. 1, No. 94, 2005.
- [28] Gaebel, T. *et al. Nature Physics*, Vol. 2, No. 408, 2006.
- [29] Hanson, R. *et al. Physical Review Letters*, Vol. 97, 087601, 2006.
- [30] Gillaspay, J. D. *Journal of Physics B: Atomic, Molecular and Optical Physics*, Vol. 34, 2001, pp. 93-130.
- [31] Schenkel, T. *et al. Progress in Surface Science*, Vol. 61, 1999, pp. 23-84.

- [32] Winter, H. and Aumayr, F. *Journal of Physics B: Atomic, Molecular and Optical Physics*, Vol. 32, 1999, pp. 39-65.
- [33] Briand, *et al. Physics Review*, Vol. A55, 1997, pp. R2523-2526.
- [34] Briand, *et al. Review of Scientific Instruments*, Vol. 71, 2000, pp. 627-630.
- [35] Aumayr, F. and Winter, H. *Electronic Journal of Surface Science Nanotechnology*, Vol. 1, 2003, pp. 171-174.
- [36] Bohr, N. *Philosophical Magazine*, Vol. 25, No. 10, 1913.
- [37] Bohr, N. *Mat. Fys. Medd. Dan. Vid. Selsk.*, Vol. 18, No. 8, 1948.
- [38] Bethe, H. A. *Annalen der Physik*, Vol. 5, No. 325, 1930.
- [39] Bethe, H. A. and Heitler, W. *Proceedings of the Royal Society*, Vol. A146, No. 83, 1934.
- [40] Bloch, F. *Annalen der Physik*, Vol. 16, No. 287, 1933.
- [41] Bloch, F. *Z. F. Physik*, Vol. 81, No. 363, 1933.
- [42] Firsov, O. B. *Zh. Eksp. Teor. Fiz.*, Vol. 32, No. 1464, 1957.
- [43] Firsov, O. B. *Journal of Experimental and Theoretical Physics*, Vol. 7, No. 308, 1958.
- [44] Lindhard, J and Scharff, M. *Mat. Fys. Medd. Dan. Vid. Selsk.*, Vol. 27, No. 15, 1953.
- [45] Lindhard, J. *et al. Mat. Fys. Medd. Dan. Vid. Selsk.*, Vol. 36, No. 10, 1968.
- [46] Sigmund, P. ed, *Radiation Damage Processes in Materials*, Norrdhoff, Leyden: Du Puy C. H. S., 1975, Chapter 1.
- [47] Ziegler, J. F. *et al. The Stopping and Range of Ions in Matter*, New York: Pergamon Press, 1985, pp. 51-108.
- [48] Schwitietz, G. *et al. Nuclear Instruments and Methods in Physics Research*, Vol. B175, No. 125, 2001.
- [49] Arnoldbik, W. M. *et al. Nuclear Instruments and Methods in Physics Research*, Vol. B203, 2003, pp. 151-157.
- [50] Burgdörfer, J. *et al. Physical Review*, Vol. A44, No. 9, 1991.

- [51] Briand, J. P. *et al. Physical Review Letters*, Vol. 65, No. 2, 1990.
- [52] Rebuli, D. B. *Electron Emission in Charged Particle Interactions with Diamond Surfaces*, PhD Thesis, University of the Witwatersrand, Johannesburg, 2003.
- [53] Bethe, H. A. and Salpeter, E. E. eds, *Quantum Mechanics of One and Two Electron Systems*, New York: Academic Press, 1957.
- [54] Varga, et al. *Physica Scripta*, Vol. T73, No. 307, 1997.
- [55] Hayderer, *et al. Nuclear Instruments and Methods in Physics Research*, Vol. B182, No. 143, 2001.
- [56] Schneider, D. H. *et al. Radiation Effects and Defects in Solids*, Vol. 127, No. 113, 1993.
- [57] Bitenskii, I. S. *et al. Zh. Tekh. Fiz.*, Vol. 49, No. 1044, 1979.
- [58] Briere, M. A, Schenkel, T. and Schneider, D. (unpublished).
- [59] Schneider, D. H. *et al. Physica Scripta*, Vol. 53, No. 228, 1996.
- [60] Cheng, H. P. and Gillaspay, J. D. *Physical Review*, Vol. 55, No. 4, 1997.
- [61] Bitenskii, I. S. and Parilis, E. S. *Atomnaya Energiya*, Vol. 46, No. 269, 1978.
- [62] Parilis, E. S. *Zeitschrift fuer Physik*, Vol. D21, No. S127, 1991.
- [63] Cheng, H. P. and Gillaspay, J. D. *Computational Material Science*, Vol. 9, No. 285, 1998.
- [64] Schneider, D. H. and Briere, M. A. *Physica Scripta*, Vol. 53, No. 228, 1996.
- [65] Schenkel, *et al. Nuclear Instruments and Methods in Physics Research*, Vol. B125, No. 153, 1997.
- [66] Bitensky, I. S. *et al. Nuclear Instruments and Methods in Physics Research*, Vol. B72, No. 380, 1992.
- [67] Schenkel, T. *et al. Material Science Forum*, Vols. 248-249, No. 413, 1997.
- [68] Aumayr, F. *et al. Communications of Atomic and Molecular Physics*, Vol. 34, No. 201, 1999.
- [69] Meftah, A. *et al. Nuclear Instruments and Methods in Physics Research*, Vol. B127, 2005, pp. 563-574.

- [70] Fleischer, R. L. *et al. Nuclear Track in Solids*, University of California Press, 1975.
- [71] Chadderton, L. T. and Mc Torrens, I. eds, *Fission Damage in Crystals*, Methuen & Co. Ltd., 1969, pp. 113, 190.
- [72] Seitz, D. and Turnbull, D. eds, *Solid State Physics 2*, 1956, pp. 305.
- [73] Boccanfuso, M. *et al. Nuclear Instruments and Methods in Physics Research*, Vol. B191, No. 301, 2002.
- [74] Trautmann, C. *et al. Physical Review*, Vol. B62, No. 13, 2000.
- [75] Trautmann, C. *et al. Journal of Applied Physics*, Vol. A66, No. 3560, 1998.
- [76] Manika, I. *et al. Nuclear Instruments and Methods in Physics Research*, Vol. B209, No. 93, 2003.
- [77] Khalfaoui, N. *et al. Nuclear Instruments and Methods in Physics Research*, Vol. B240, No. 819, 2005.
- [78] El-Said, A. S. *et al. Nuclear Instruments and Methods in Physics Research*, Vol. B218, No. 492, 2004.
- [79] El-Said, A. S. *et al. Nuclear Instruments and Methods in Physics Research*, Vol. B258, 2007, pp. 167-71.
- [80] Dufour, C. *et al. Journal of Physics: Condensed Matter*, Vol. 5, No. 4573, 1993.
- [81] Toulemonde, M. *et al. Nuclear Instruments and Methods in Physics Research*, Vol. B166/167, No. 903, 2000.
- [83] Lifshitz, I. M. *et al. Journal of Nuclear Energy*, Vol. A12, No. 69, 1960.
- [84] Waligorski, M. P. *et al. Nuclear Tracks and Radiation Measurements*, Vol. 11, No. 3, 1986.
- [85] Pierson, H. O. ed, *Handbook of Carbon, graphite, diamond and fullerenes: Properties, Processing and Applications*, New Jersey: Noyes Publications, 1993, pp. 11-39.
- [86] Papali, P. ed, *Physics of Diamond*, Italy: Società Italiana di Fisica, 1997, pp. 10-13.
- [87] <http://www.shef.ac.uk/physics/teaching/phy204/index.html>
- [88] Kittel, C. ed, *Introduction to Solid State Physics*, 7th ed. Singapore: John Wiley & Sons (Asia) Pte. Ltd., 1996, pp. 17-20.

- [89] Nazarè, M. H. and Neves, A. J. eds, *Properties, Growth and Applications of Diamond*, London: INSPEC IEE, 2001, pp. 247-61.
- [90] Davis, R. F. ed, *Diamond films and coatings: development, properties and applications*, New Jersey: Noyes Publications, 1993, pp. 3-15.
- [91] <http://phycomp.technion.ac.il/~david/thesis/node3.html>.
- [92] <http://www.webelements.com/carbon/allotropes.html>.
- [93] Werner, M. and Locher, R. *Reports on Progress in Physics*, Vol. 61, 1998, pp. 1665-1710.
- [94] http://dao.mit.edu/8.231/carbon_phase_diagram.jpg.
- [95] Kennedy, T. Y. and Kennedy, G. C. *Journal of Geophysical Research*, Vol. 81, 1976, pp. 2467-9.
- [96] Davies, G. ed, *Properties and Growth of Diamond*, London: INSPEC IEE, 1994, pp. 404-8.
- [97] Reguero, M. N. *et al. Nature*, Vol. 355, 1992, pp. 237-39.
- [98] Yagi, T. *et al. Physical Review*, Vol. B46, 1992, pp. 6031-39.
- [99] Burns, R. C. *et al. Journal of Crystal Growth*, Vol. 104, 1990, pp. 257-79.
- [100] Strong, H. M. and Chrenko, R. M. *Journal of Physical Chemistry*, Vol. 75, 1971, pp. 1838-43.
- [101] Chrenko, R. M. *et al. Philosophical Magazine*, Vol. 23, 1971, pp. 313-8.
- [102] Collins, A. T. and Lawson, S. C. *Philosophical Magazine letters*, Vol. 60, 1989, pp. 117-22.
- [103] Kanda, H. and Yamaoka, S. *Diamond and Related Materials*, Vol. 2, 1993, pp. 1420-3.
- [104] Isoya, J. *et al. Physical Review*, Vol. B42, 1990, pp. 9843-52.
- [105] Isoya, J. *et al. Physical Review*, Vol. B42, 1990, pp. 9843-52.
- [106] Nadolinny, V. A. and Yelisseyev, A. P. *Diamond and Related Materials*, Vol. 3, 1994, pp. 1196-1200.
- [107] Kamo, M. *et al. Journal of Crystal Growth*, Vol. 62, No. 642, 1983.

- [108] Hyman, E. *et al. Journal of Vacuum Science and Technology*, Vol. A12, No. 1474, 1994.
- [109] Capitelli, M. *et al. Plasma Chemical and Process Engineering*, Vol. 16, No. 153, 1996.
- [110] Dolmatov, V. Y. *Physics of the Solid State*, Vol. 46, No. 4, 2004, pp. 611-15.
- [111] Robertson, J. *Material Science and Engineering*, Vol. 37, No. 129, 2002.
- [112] Wang, C. X. and Yang, G. W. *Material Science and Engineering*, Vol. 49, No. 157, 2005.
- [113] Liu, P. *et al. Journal of Physical Chemistry*, Vol. C113, 2009, pp. 12154-61.
- [114] Yang, G. W. *Progress in Material Science*, Vol. 52, No. 648, 2007.
- [115] Fuge, G. M. *et al. Diamond and Related Materials*, Vol. 12, No. 1049, 2003.
- [116] Fuge, G. M. *et al. Journal of Applied Physics*, Vol. 99, 014309, 2006.
- [117] Yang, L. *et al. Diamond and Related Materials*, Vol. 16, No. 725, 2007.
- [118] Wang, C. X. *et al. Applied Physics Letters*, Vol. 87, 201913, 2005.
- [119] Daulton, T. L. *et al. Nuclear Instruments and Methods in Physics Research*, Vol. B175, No. 12, 2001.
- [120] Wesolowski, P. *et al. Applied Physics Letters*, Vol. 71, No. 1948, 1997.
- [121] Banhart, F. and Ajayan, P. M. *Nature*, Vol. 382, No. 433, 1996.
- [122] Daulton, T. L. *et al. Materials Research Society Symposium Proceedings*, Vol. 540, No. 189, 1999.
- [123] Bar-Yam, Y. and Moustakas, T. D. *Nature*, Vol. 342, No. 786, 1989.
- [124] Badiag, P. *et al. Nature*, Vol. 343, No. 244, 1990.
- [125] Meguro, T. *et al. Nuclear Instruments and Methods in Physics Research*, Vol. B235, 2005, pp. 431-37.
- [126] Jiang, Q. *et al. Journal of Physics: Condensed Matter*, Vol. 12, No. 5623, 2000.
- [127] Koga, H. and Watanabe, S. *57th Meeting Abstracts of the Physical Society of Japan*, Vol. 57, Issue 1, Part 4, 2002, pp. 846.
- [128] Epstein, R. J. *et al. Nature*, Vol. 1, 2005, pp. 94-98.

- [129] Loubster, J. H. and van Wyk, J. A. Reports on Progress in Physics, Vol. 41, 1978, pp. 1201-1248.
- [130] Awschalom, D. *et al.* Scientific American, October 2007, pp. 84-91.
- [131] Benioff, P. *Physical Review Letters*, Vol. 48, No. 23, 1982, pp. 1581-1585.
- [132] Feymann, R. *International Journal of Theoretical Physics*, Vol. 21, No.6/7, 1982, pp. 467-488.
- [133] Shor, P. W. *Society for Applied and Industrial Mathematics Journal of Computing*, Vol. 26, 1997, pp. 1484-1509.
- [134] Kane, B. E. Nature, Vol. 393, No. 133, 1998.
- [135] Berman, G. P. *et al.* eds, *Introduction to Quantum Computers*, Singapore: World Scientific Publishing Co. Pte. Ltd., 1998, pp. 1-7.
- [136] Monroe, C. *et al.* *Physical Review Letters*, Vol. 75, No. 25, 1995.
- [137] DiVincenzo, D. P. *Fortschritte der Physik*, Vol. 48, 2000, pp. 771-783.
- [138] <http://www-ebit.lbl.gov/>.
- [139] <http://physics.nist.gov/MajResFac/EBIT/intro.html#120>.
- [140] Tseng, A. A. *et al.* *Journal Vacuum Science and Technology*, Vol. 23, No. 877, 2005.
- [141] Egger, S. *et al.* Nano Letters, Vol. 5, No. 15, 2005.
- [142] Persaud, A. *et al.* *Journal of Vacuum Science and Technology*, Vol. B23, No. 6, 2005.
- [143] Schenkel, T. *et al.* *Journal of Vacuum Science and Technology*, Vol. B21, 2720, 2003.
- [144] Rangelow, W. *et al.* *Proceedings of the Society of Photo-Optical Instrumentation Engineers (SPIE)*, Vol. 2879, No. 56, 1996.
- [145] Persaud, A. *et al.* *Journal of Vacuum Science and Technology*, Vol. B22, No. 2992, 2004.
- [146] Persaud, A. *et al.* *Journal of Vacuum Science and Technology*, Vol. B24, No. 6, 2006.
- [147] Persaud, A. *et al.* *Quantum Information Processing*, Vol. 3, No. 233, 2003.
- [148] Schenkel, T. *et al.* *Journal of Applied Physics*, Vol. 94, No. 7017, 2003.
- [149] <http://www.srim.org/>.

- [150] Veeco Metrology Group, *di CP-II User's Guide Part I: Basic Imaging Techniques*, California, 85-10335 Revision. B, 2004.
- [151] Veeco Metrology Group, *diProScan Data Acquisition Software CP-II User's Guide Part III*, California, 48-101-1101 Revision E, November 2004.
- [152] Veeco Metrology Group, *di CP-II User's Guide Part II: Advanced Techniques*, California, 85-10354 Revision B, 2004.
- [153] Veeco Metrology Group, *NanoScope Scanning Tunneling Microscope Operation Manual*, Software Version 5.12, 004-230-00, 2001.
- [154] Bonnel, D. A. ed, *Scanning Probe Microscopy and Spectroscopy; Theory, Techniques and Applications*, 2nd ed. Canada: Wiley-VCH, Inc., 2001, pp. 43-154.
- [155] Ivanov-Omskiĭ, V. I. *et al. Semiconductors*, Vol. 34, No. 12, 2000, pp. 1355-1362.
- [156] Feensta, R. *et al. Surface Science*, Vol. 181, No. 295, (1987).
- [157] Vasil'ev, S. Y. *et al. Technical Physics*, Vol. 45, No. 99, 2000.
- [158] Veeco Metrology Group, *diSPMLab Version 5.01 Reference Manual*, California, 85-10317 Review D, December 2004.
- [159] Knight, D. S. and White, W. B. *Journal of Material Research*, Vol. 4, No. 385, 1989.
- [160] Dresselhaus, M. S. and Dresselhaus, G. eds, *Light Scattering in Solids III*, Berlin: Springer-Verlag, 1982.
- [161] Dresselhaus, M. S. *et al.* eds, *Science of Fullerenes and Carbon Nanotubes*, New York: Academic Press, 1996.
- [162] Saito, R. ed, *Physical Properties of Carbon Nanotubes*, London: Imperial College Press, 1998.
- [163] Irmer, G. and Dorner-Reisel, A. *Advanced engineering Materials*, Vol. 7, No. 8, 2005, pp. 694-705.
- [164] Kittel, C. ed, *Introduction to Solid State Physics*, 7th ed. Singapore: John Wiley & Sons (Asia) Pte. Ltd., 1996, pp. 322-324.
- [165] Gouadec, G. and Colomban, P. *Progress in Crystal Growth and Characterization of Materials*, Vol. 53, 2007, pp. 1-56.
- [166] Goldsmith, N. T. *Image Analysis and Stereology*, Vol. 19, No. 163, 2000.

- [167] Meyers, R. A. ed, *Encyclopedia of Analytical Chemistry*, Chichester: John Wiley & Sons Ltd., 2000, pp. 9209-9231.
- [168] Stokes, G. G. *Philosophical Transactions of the Royal Society of London*, Vol. A142, No. 463, 1852.
- [169] Mielenz, K. D. ed, *Optical Radiation Measurements*, Volume 3, New York: Academic Press, 1982, pp. 2-19.
- [170] Birks, J. B. *Photophysics of Aromatic Molecules*, New York: Wiley (Interscience), 1970.
- [171] Pimenta, M. A. *et al. Physical Chemistry Chemical Physics*, Vol. 9, 2007, pp. 1276-91.
- [172] Niwase, K. *Physical Review*, Vol B52, 15785, 1995.
- [173] Nakamura, K. and Kitajima, M. *Physical Review*, Vol. B45, Vol. 78, 1992.
- [174] Tona, M. *et al. Nuclear Instruments and Methods in Physics Research*, Vol. B235, 2005, pp. 443-447.
- [175] Sideras-Haddad, E. *et al. Nuclear Instruments and Methods in Physics Research*, Vol. B267, 2009, pp. 2774-7.
- [176] Chung, P. H. *et al. Surface Science*, Vol. 601, 2007, pp. 3866-3870.
- [177] Sun, K. W. and Wang, C. Y. *Journal of Physics: Conference Series*, Vol. 92, 2007, No. 0120231.
- [178] Tisler, J. *et al. American Chemical Society*, Vol. 3, No. 7, 2009, pp. 1959-1965.
- [179] Adhikary, S. *et al. Diamond and Related Materials*, Vol. 14, 2005, pp. 1832-1834.

